Spectral Wave Modelling with Nonlinear Dissipation

Dissertation
zur Erlangung des Doktorgrades der Naturwissenschaften
im Fachbereich Geowissenschaften
der Universität Hamburg

vorgelegt von

Christoph Schneggenburger

aus Bensberg

Hamburg

1998

Als Dissertation angenommen vom Fachbereich Geowissenschaften
der Universität Hamburg

auf Grund der Gutachten von Professor Dr. Hans von Storch
und Dr. Wolfgang Rosenthal

Hamburg, den 21. Oktober 1998

Professor Dr. G. Miehlich
(Dekan des Fachbereichs Geowissenschaften)

Abstract

A spectral wave model with nonlinear dissipation is introduced, analysed, and applied to wind-wave investigations in the Sylt-Rømø tidal basin. The model has been developed within this study for applications in small-scale shallow-water environments. It uses for the first time a source function which describes dissipation by wave turbulence interaction. The nonlinear parametrization of this mechanism is shown to be formally and physically motivated. With regard to small-scale inhomogeneous applications the neglect of nonlinear interactions is justified. The use of action density in wave number direction coordinates as prognostic field in the model enables a convenient treatment of instationary systems, e.g. systems with tidal influence. Principal features of the model are elucidated by analytical investigation in simple cases. Results of various academic test cases show that in small-scale systems the model is consistent with observational knowledge. Numerical experiments on wind waves in the Sylt-Rømø tidal basin demonstrate the applicability of the model in small-scale systems with time-varying water levels and currents. A considerable influence of tidal currents on wind waves is indicated by case studies for prescribed wind situations. A one-month hindcast of wind waves in the Sylt-Rømø tidal basin is used for a successful validation of the model against field data. For the first time, influence of tidal currents on wave parameters is reproduced quantitatively. It is shown in particular that inclusion of tidal currents distinctly improves the hindcast skill of wave periods.

Zusammenfassung

Ein spektrales Seegangsmodell mit nichtlinearer Dissipation wird vorgestellt, analysiert und für Seegangsuntersuchungen in der Sylt-Rømø-Bucht angewendet. Das Modell wurde innerhalb dieser Arbeit für Anwendungen in kleinskaligen Flachwassersystemen entwickelt. Zum ersten Mal wird eine Quellfunktion verwendet, die Dissipation durch Seegang-Turbulenz-Wechselwirkung beschreibt. Es wird gezeigt, daß die nichtlineare Parametrisierung dieses Prozesses formal und physikalisch motiviert ist. Für Anwendungen in kleinskaligen inhomogenen Systemen ist die Vernachlässigung von nichtlinearen Wechselwirkungen gerechtfertigt. Die Verwendung der Wirkungsdichte in (k, θ)-Koordinaten als prognostisches Feld ermöglicht eine bequeme Behandlung instationärer Systeme, z.B. solche mit Tideneinfluß. Grundsätzliche Eigenschaften des Modells werden durch analytische Untersuchungen in einfachen Fällen verdeutlicht. Diverse akademische Testfälle zeigen, daß das Modell in kleinskaligen Systemen experimentelle Resultate reproduziert. Numerische Simulationen von Seegang in der Sylt-Rømø-Bucht demonstrieren die Verwendbarkeit des Modells in Systemen mit zeitveränderlichen Wassertiefen und Strömungen. Ein erheblicher Einfluß von Tidenströmungen auf den Seegang wird durch Fallstudien für vorgeschriebene Windsituationen gezeigt. Eine Nachrechnung von Seegang über einen Zeitraum von einem Monat wird für eine erfolgreiche Validierung des Modells anhand gemessener Daten verwendet. Zum ersten Mal wird der Einfluß von Tidenströmungen auf Seegangsparameter quantitativ reproduziert. Insbesondere wird durch Berücksichtigung von Tidenströmungen der Hindcast Skill der Wellenperioden deutlich verbessert.

Contents

List of Figures

List of Tables

1 Introduction

The subject of this doctoral thesis is spectral wave modelling with nonlinear dissipation. The general features and capabilities of this modelling approach, as well as its applicability to modelling of the sea state in coastal systems is investigated. The aim of the introduction is to give an overview of the research presented in this thesis. The general framework is introduced in the first section. This includes the presentation of motivations and an outline of the scientific context. In the latter the work presented in the thesis will be related to comparable work of other authors. The specific framework of the thesis will be set in the second section: general aims and purposes will be laid down and, more specifically, the objectives of the study will be made apparent and the approach to and procedure for the investigation will be described. In a final paragraph, an outline of the text will be presented and the notation used will be clarified.

1.1 Motivation and Scientific Context

Motivations for research on spectral wave modelling are manifold. Classic objectives for the prediction of the sea state have been to ensure security in shipping traffic, in offshore operations, and for activities on offshore platforms. Prediction of coastal sea states is of major interest for designing coastal protection constructions, ports, harbours, and navigational channels. But in addition to these "traditional" application fields for spectral wave modelling, it is commonly accepted today that the sea state is an important paramater both in the global coupled atmospheric and oceanic system and in coastal dynamical systems. Third-generation ocean wave models are used e.g. for assessment of the climatological impact of sea-state/atmosphere coupling (ASPEN project: Air Sea Processes, EC Environment and Climate Programme). In a recent paper by Lionello et al. (1998), the sea-state influence on atmospheric circulation in oceanic systems is indicated in several case studies. Whereas for oceanic and shelf-sea applications of wave modelling a sophisticated state of the art has been established through decades of research (see e.g. Komen et al. 1994, Cardone et al. 1998), research on wave models for coastal applications is still in progress. The relevance of the sea state in these systems is elucidated briefly in what follows. Coastal dynamical systems consist of coupled atmospheric, hydrodynamic, morphological, and biological subsystems. In coastal environments, the sea state acts as link between the listed subsystems: it influences mass, momentum, and energy fluxes between atmosphere and water body (Donelan 1995, Makin 1998). It has a leading impact on mobilization of sediments. Besides a direct influence on the suspended matter regime, this mechanism causes a wave impact on water quality, because some classes of nutrients and pesticides may be linked to sediments and suspended matter in the water column. In addition, an impact on the biology is present through modulation of the light regime in the water column. Recent interest in coupled atmospheric, hydrodynamic, and sedimentologic phenomena in the Sylt-Rømø tidal basin (activities within European Union MAST III Programme PROMISE, MAS3 CT 9500025, at GKSS Forschungszentrum) thus causes a strong need for a coastal wave model suitable for application to complex tidal systems and coupling phenomena between the atmospheric, hydrodynamic, and suspended-matter subsystems.

There are two different classes of wave models for coastal systems: time or frequency-domain

phase-resolving models, and frequency-domain phase-averaging models, also referred to as spectral wave models. Recent overviews of the capabilities of the two approaches can be found in Ris (1997) and Cardone et al. (1998). Phase-resolving models are advantageous in problems where nonlinear shoaling in varying media on scales of wave lengths and periods occur, or where diffraction is important. Spectral wave models have the great advantage that arbitrary random-phase source functions can be included. In this way, wave generation by wind, wave nonlinear interactions, and wave dissipation can be taken into account. Coupling of waves to atmosphere and hydrodynamics can be considered. However, diffraction cannot be included in phase-averaged models, and nonlinear propagation effects are usually neglected.

The preceding paragraph has made clear that for the planned application of a wave model in a coupled coastal model system a spectral wave model must be used. Various models of this kind for application to larger-scale systems exist, cf. section 2.1. The question arises whether existing models can be readily applied to coastal systems. In principal this is possible, but major adjustments must be made for numerical adaption to the small scales, and emphasis on further and maybe different physical processes must be set. The research presented in this thesis is one possible adaption of an existing spectral wave model to coastal systems. While the study was in progress, further attempts of this kind have been made, see e.g. Ris (1997) and Luo et al. (1998), but these authors have used different approaches. Luo et al. mainly focus on numerical adaptions to speed up an ocean wave model for use in small scale applications, i.e. the time-step splitting is generalized and frequency-dependent propagation time steps are incorporated. As in this approach, Ris and coworkers take over ocean-wave-model processes to coastal wave modelling. But various additional processes are added which can be important in coastal systems, e.g. depth-induced wave breaking and triad nonlinear coupling of waves. The rising complexity of such a model is compensated by these authors by basing their model on a stationary version (Holthuijsen et al. 1993). It has recently been extended to an instationary mode which is characterized by a fully implicit propagation scheme with no stability limitations to the time steps (Booij et al. 1998). This is seen as a major advantage in comparison to a classic explicit upwind scheme as used e.g. in the third-generation ocean wave model WAM cy. 4 (Günther et al. 1992). But it is stressed here that the use of comparatively large time stepping in an unconditionally stable implicit scheme may be comfortable, but can on the other hand lead to intolerable inaccuracies. A restriction of computational efficiency is imposed by accuracy requirements in a similar quality as by stability requirements. For this reason, the benefits of unconditional stability decrease in relevance.

In the approach taken in this thesis, emphasis is set on a limitation of model complexity. This is achieved by an attempt to identify essentially relevant processes and to neglect less relevant ones. It will be shown that in small-scale systems observational evidence can be reproduced by an approach to the source functions which is much simpler than in third-generation ocean wave models. A nonlinear dissipation function is used as key dissipation mechanism. It accounts for dissipation by wave turbulence interactions. Internal nonlinear interactions of waves according to the theory of Hasselmann (1962) are neglected. In the present study, nonlinear dissipation and its combination with further source functions is used for the first time in a spectral wave model. The quality of the modelling strategy will be demonstrated, but its limitations will also be pointed out. The scientific approach is described in detail in the next section.

1.2 This Thesis

General Aim and Purpose. Spectral wave models have been used to predict sea states in large- and intermediate-scale oceanic and shelf sea systems. Various approaches are in progress today to adapt these models for use in small-scale coastal systems. One approach is investigated in this thesis. The general aim is to establish a spectral wave model suitable for installing into a coupled model system for coastal environments. The focus is set on limiting the complexity of the modelling approach by retaining only essentially relevant physical processes in the wave model.

The purpose of this work is to enable investigation of coupled coastal dynamical systems. In particular, the consideration of sea-state impacts on sediment and suspended matter dynamics, on morphology, water quality, and biology will be made possible. In this way, an important contribution to near-future research activity proposed e.g. at GKSS Forschungszentrum will be given. As far-range goal, coupled modelling of coastal dynamical systems will enable an assessment of human impacts and lead to a strategy for coastal management and sustainable development. The preceding paragraphs make apparent that waves can play a significant role in these questions.

Objectives of this Study. The described general aim is realized in this thesis by investigation of spectral wave modelling with nonlinear dissipation and analysis of a corresponding wave model in coastal applications. Accordingly, the specific objectives of this study are:

1. To give formal justifications for nonlinear dissipation in spectral wave modelling and the neglect of quadruplet nonlinear interactions in coastal wave modelling

2. To investigate general features and capabilities of a wave model with nonlinear dissipation and disregard of quadruplet interactions

3. To test and validate this wave model in applications to a coastal system

4. To demonstrate the applicability of the model in investigations of coastal systems.

Approach and Procedure. The investigational approach of this study is to analyse a wave model and perform numerical experiments with it. The procedure of investigation, related to the given objectives, is described in the following:

1. A general nonlinear shape of dissipation source functions will be reviewed from literature. It is based on a functional power-series expansion. Different classes of specific parametrizations are shown to be consistent with this form, including the formulation investigated in this thesis. The neglect of nonlinear interactions in the case of small-scale applications to inhomogeneous systems will be discussed in general terms. A rigorous analysis of this aspect is beyond the scope of this thesis, however.

2. As tool for investigation, a wave model with nonlinear dissipation was developed. General features of this model will be investigated in two steps. A wave model is a solver of a partial differential equation. The model equation will be analysed in simple cases and simplifying

approximations in a first step. As a second step, computation of so-called academic test cases will enable analysis of features in a more realistic framework. Comparison with other models and with observational evidence will be possible. The latter is very important for a final assessment of model features and performance.

3. Numerical experiments of two kinds have been performed to test and validate the model in a small-scale coastal application, and to demonstrate the applicability of the model for investigations of these systems.

   (a) In case studies for two different prescribed wind situations the impact of tidal currents on wind waves in the Sylt-Rømø tidal basin is investigated. Wave model runs have been performed with and without current input. This enables direct indication of current effects by comparison of time series, parameter fields, and two-dimensional wave spectra from the output of the two model runs.

   (b) A one-month wave hindcast in the Sylt-Rømø tidal basin allows statistical validation of the model against field measurements of wave parameters from within the tidal basin. Furthermore, current effects as indicated in the case studies can be quantified in a realistic hindcast, again by comparison of model output with and without currents. The relevance of current impact on the waves in this system can be assessed in an objective manner by comparison of the corresponding validation statistics.

Outline of the Thesis, Notation. The text is divided into three main chapters and a final chapter containing overall conclusions of this thesis. In chapter 2, established concepts of spectral wave modelling will be reviewed. A formal analysis of nonlinear dissipation functions will be carried out. Furthermore, a wave model with nonlinear dissipation will be described, and the neglect of nonlinear interactions will be discussed. The analysis of spectral wave modelling with nonlinear dissipation will be presented in chapter 3. Three sections contain analytical investigations, academic test cases, and a North-Sea storm period hindcast to extend comparison with existing models and field data. In chapter 4, numerical experiments in the Sylt-Rømø tidal basin are covered. Various technical details and supplementing informations are collected in appendix A.

Remarks on applied notation conclude this introduction. In the presented mathematical formulae, vectors appear as bold letters. Their inner product is denoted by a central dot. Partial derivatives with respect to a scalar quantity, say time t, appear as "$\partial_t(.)$". Gradients with respect to, say location $\boldsymbol{x}$, are denoted by "$\partial_{\boldsymbol{x}}(.)$". References to numbered equations appear in the text as parenthesized numbers, e.g. (2.3) means "equation (2.3)". A list of symbols and acronyms used in the text is provided in appendix B.

2 Concepts of Wave Modelling with Nonlinear Dissipation

This chapter covers the basic concepts of spectral wave modelling with nonlinear dissipation. In the first section, a review of the fundamentals of spectral wave modelling will be given. The second section covers the concept of nonlinear dissipation. Basic formal and physical motivations are reviewed from literature and extended. A wave model with nonlinear dissipation is described in the third section. A final section gives a summary of the chapter.

2.1 Review of Spectral Wave Modelling

A review of the concepts of spectral wave modelling is given here for the purpose of clarifying terminology and listing formulae needed subsequently in the text. A rigorous derivation of the fundamental theory will not be presented. Instead, reference is made to basic textbooks, e.g. Phillips (1977) and Komen et al. (1994).

Spectral wave models predict the evolution of the sea state in a specified area of investigation, depending on the initial state, on boundary values, and on external fields like wind, water depths, and currents. The aim is to characterize the sea state on space and time scales which are large compared to typical wave lengths and wave periods, i.e. no attempt is made to resolve the detailed space-time structure of the sea surface. The mathematical description of the sea state is the wave spectrum. The dynamics of wave spectra on large space and time scales are given by the action balance equation. Spectral wave models solve this equation numerically. Some remarks on the historical perspective of wave modelling will be made at the end of the section.

2.1.1 Linear Waves and Wave Spectra

Wave spectra can be defined by two alternative approaches: by an energy expression valid in linear wave theory and by a statistical description of the sea surface. Both approaches will be equivalent if the sea state is quasi-stationary and quasi-homogeneous in a statistical sense and can be well approximated by a superposition of slowly varying linear wave trains. The two approaches will be introduced here.

Dynamics of Linear Waves. Gravity waves on the surface of a water body with infinite depth or space-constant finite depth h, and space-constant current $\boldsymbol{u}_{\mathrm{c}}$ can be described by a velocity potential $\phi(\boldsymbol{x}, z, t)$ for the wave flow field and a surface elevation field $\eta(\boldsymbol{x}, t)$ describing the deviation of the water/air boundary from its mean (equilibrium) value. The vector $\boldsymbol{x}$ is two-dimensional and contains the horizontal location coordinates, z denotes the vertical space coordinate. The constraint to homogeneous (space-constant) systems can be relaxed to slowly varying inhomogeneous systems, see below. The wave dynamics are given by a linear partial differential equation – the Laplace equation – for the velocity potential. Two nonlinear boundary conditions for the free water surface are connected to it, viz. the kinematical and the dynamical condition. In case of finite water depth, a linear bottom boundary condition is additionally

considered. Linearization of the surface boundary conditions yields a general solution for the surface elevation function (and velocity potential) of the waves.

The linearization is exact for waves with infinitesimal amplitudes. It is a good approximation in the case of small wave steepness, i.e. a small ratio of wave amplitude to wave length. The solutions of the linearized system are identical to the first terms in an expansion of the waves into a series with terms containing rising powers of a steepness parameter. This expansion is called Stokes expansion, cf. Witham (1974). In spectral wave modelling only the linear solutions are taken into account. Effects of weak nonlinearity are usually treated via perturbation theory on the level of the wave-spectrum dynamics, see subsection 2.1.2.

Solutions of the linearized system can be given as normal-mode solutions for the surface elevation field η and the velocity potential ϕ, both characterized by wave vectors $\boldsymbol{k}$. For each $\boldsymbol{k}$ there exist the solutions $(\pm)$

$$\begin{aligned} \eta(\boldsymbol{x},t) &= a \exp i(\boldsymbol{k}\cdot\boldsymbol{x} - \omega_\pm t) + \text{c.c.} \\ \phi(\boldsymbol{x},z,t) &= -i\omega_\pm a \frac{\cosh k(z+h)}{k \sinh kh} \exp i(\boldsymbol{k}\cdot\boldsymbol{x} - \omega_\pm t) + \text{c.c.} \end{aligned} \tag{2.1}$$

with the circular frequencies

$$\omega_\pm = \pm\sigma(\boldsymbol{k}) + \boldsymbol{k}\cdot\boldsymbol{u}_\text{c} \tag{2.2}$$

and the dispersion relation

$$\sigma(\boldsymbol{k})^2 = gk \tanh kh, \tag{2.3}$$

which relates the intrinsic frequency σ to wave number k and water depth h. The solution for the velocity potential is given here to show its dependence on the vertical coordinate z. The following discussion will be restricted to the η fields, however. In (2.3), the effects of surface tension are neglected, only gravity waves are taken into account. In (2.1), "c.c." denotes the complex conjugate of the right-hand-side term. The normal-mode solutions are "wavelike", with a complex amplitude a and a phase $(\boldsymbol{k}\cdot\boldsymbol{x} - \omega_\pm t)$ depending on location and time. The wave length λ and wave period T are defined as

$$\lambda \equiv 2\pi/k, \quad T \equiv 2\pi/\omega_+. \tag{2.4}$$

The general solution of the linearized system is given as superposition (linear combination) of the normal mode solutions. It is equivalent to a Fourier representation of the sea surface, if no other modes than surface gravity waves are present. A reality condition for the surface elevation η allows to replace the ω_- mode by the complex conjugate of the ω_+ mode. The general solution then reads

$$\eta(\boldsymbol{x},t) = \int_{-\infty}^{\infty} \mathrm{d}\boldsymbol{k}\, a(\boldsymbol{k}) \exp i(\boldsymbol{k}\cdot\boldsymbol{x} - \omega t) + \text{c.c.}, \tag{2.5}$$

with the identification $\omega \equiv \omega_+$. As above, the amplitudes $a(\boldsymbol{k})$ of the normal modes with wave vector $\boldsymbol{k}$ are complex numbers. An expression for the spatially mean energy density $\overline{E}$ of the wave field described by (2.5) is

$$\overline{E} = 2\rho g \int \mathrm{d}\boldsymbol{k}\, |a(\boldsymbol{k})|^2. \tag{2.6}$$

Here, ρ denotes the density of water, g the gravitational acceleration.

A specification of $\overline{E}$ can be regarded as representation belonging to an ensemble of possible sea states in a given situation. The ensemble mean of $\overline{E}$ defines the wave spectrum $F(\boldsymbol{k})$ as used in spectral wave models:

$$\langle \overline{E} \rangle = \rho g \int \mathrm{d}\boldsymbol{k}\, F(\boldsymbol{k}),\ F(\boldsymbol{k}) \equiv 2\, \langle |a(\boldsymbol{k})|^2 \rangle. \tag{2.7}$$

Equation (2.7) defines the wave spectrum as describing the ensemble mean energy density per normal mode of the wave field. The phase information of the complex amplitude belonging to a normal mode is not retained. For this reason, spectral wave models are also called phase-averaging models.

Statistical Description. In contrast to the previous paragraph, an introduction of the wave spectrum can be alternatively started with a statistical description of the sea surface, into which the dynamics are introduced as last step. For a detailed analysis see e.g. Komen et al. (1994). The basic ideas will be given here in order to elucidate subsequent statistical interpretations of the integrated parameters of the wave spectrum.

The sea surface is considered as superposition of random waves. A deterministic specification of the surface is regarded as impossible. The field $\eta(\boldsymbol{x}, t)$ describing the deviation of the sea surface from its mean level at different locations and times is therefore treated as random variable. A joint probability function P describes the ensemble statistics of the surface. The ensemble is defined as set of possible representations of the surface elevation field for given boundary conditions. For example, a two-point joint probability $P(\eta_1, \eta_2) d\eta_1 d\eta_2$ gives the probability of finding at space-time locations $(\boldsymbol{x}_1, t_1)$ and $(\boldsymbol{x}_2, t_2)$ the values $\eta_1 = \eta(\boldsymbol{x}_1, t_1)$ and $\eta_2 = \eta(\boldsymbol{x}_2, t_2)$ for the surface elevation field η. The distribution P is nearly Gaussian. It follows that the statistical information of P is basically contained in the first two moments. Since the first moment $\langle \eta(\boldsymbol{x}, t) \rangle$ is zero by definition of the η field, the two-point covariance function $\langle \eta(\boldsymbol{x}_1, t_1) \eta(\boldsymbol{x}_2, t_2) \rangle$ characterizes the statistics completely. Here, angular brackets denote ensemble expectation values, which are defined as expectation with respect to the P distribution. In the case of statistical homogeneity and stationarity, the two-point covariance function depends only on the difference of locations $\boldsymbol{\xi}$ and difference of times τ:

$$\widehat{F}(\boldsymbol{\xi}, \tau) \equiv \langle \eta(\boldsymbol{x} + \boldsymbol{\xi}, t + \tau) \eta(\boldsymbol{x}, t) \rangle, \tag{2.8}$$

independent of $\boldsymbol{x}$ and t. The wave spectrum $F(\boldsymbol{k})$ can then be defined via the three-dimensional Fourier transform $F(\boldsymbol{k}, \omega)$ of the covariance function $\widehat{F}(\boldsymbol{\xi}, \tau)$ with respect to $\boldsymbol{\xi}$ and τ. It is obtained by integration of the Fourier transform over the positive frequencies ω:

$$F(\boldsymbol{k}) \equiv \int_0^\infty \mathrm{d}\omega F(\boldsymbol{k}, \omega). \tag{2.9}$$

The dynamics of linear waves can be introduced into this description by taking into account the dispersion relation in the integration (2.9) and by assuming a general expression (2.5) as valid for the η field in (2.8). In this case the definitions (2.7) and (2.9) for the wave spectrum are equivalent.

2.1.1.1 Generalization to Inhomogeneous Systems

To be able to describe the evolution of the sea state on large space and time scales, e.g. depending on the large-scale variability of a wind field, the definition of the wave spectrum $F(\boldsymbol{k})$ as description of the sea state must be generalized to a function $F(\boldsymbol{k}, \boldsymbol{x}, t)$ of space and time on the large scales. The generalization with a two-scale approach is applicable to both the dynamics of linear waves and the statistical description of the sea surface.

Wave Dynamics in Slowly Varying Media. The normal mode solutions (2.1) can be generalized to slowly varying wave trains, which are characterized by an amplitude $a(\boldsymbol{x}, t)$ and a phase function $\theta(\boldsymbol{x}, t)$, both varying with $\boldsymbol{x}$ and t on the large scales. The wave trains are given by

$$\eta(\boldsymbol{x}, t) = a(\boldsymbol{x}, t) \exp i\theta(\boldsymbol{x}, t). \tag{2.10}$$

Space and time derivatives of the phase function define local wave vector and local circular frequency of the wave train:

$$\boldsymbol{k}(\boldsymbol{x}, t) \equiv \partial_{\boldsymbol{x}} \theta(\boldsymbol{x}, t), \quad \omega(\boldsymbol{x}, t) \equiv -\partial_t \theta(\boldsymbol{x}, t). \tag{2.11}$$

As for the normal mode solutions of the homogeneous system, wave vector and circular frequency of the wave train are connected by a dispersion relation

$$\omega(\boldsymbol{x}, t) = \Omega(\boldsymbol{k}(\boldsymbol{x}, t), \zeta(\boldsymbol{x}, t)). \tag{2.12}$$

The dispersion function Ω depends on a quantity $\zeta(\boldsymbol{x}, t)$ which formally summarizes the local properties of the medium. In the case of a linear gravity wave train in a basin with water depth field $h(\boldsymbol{x}, t)$ and current field $\boldsymbol{u}_{\mathrm{c}}(\boldsymbol{x}, t)$ the dispersion function reads

$$\Omega(\boldsymbol{k}(\boldsymbol{x}, t), \boldsymbol{x}, t) = \sigma(\boldsymbol{k}(\boldsymbol{x}, t), \boldsymbol{x}, t) + \boldsymbol{k}(\boldsymbol{x}, t) \cdot \boldsymbol{u}_{\mathrm{c}}(\boldsymbol{x}, t). \tag{2.13}$$

Here, the local intrinsic frequency σ is a generalization of equation (2.3)

$$\sigma(\boldsymbol{k}(\boldsymbol{x}, t), \boldsymbol{x}, t)^2 = gk(\boldsymbol{x}, t) \tanh k(\boldsymbol{x}, t) h(\boldsymbol{x}, t), \tag{2.14}$$

where $k(\boldsymbol{x}, t)$ is the local wave number, i.e. modulus of local wave vector. The arguments $\boldsymbol{x}$ and t will be dropped in the following and in subsequent chapters if confusion is unlikely. The group velocity of the wave train is defined as

$$\boldsymbol{v}_{\mathrm{g}} \equiv \partial_{\boldsymbol{k}} \Omega = \partial_{\boldsymbol{k}} \sigma + \boldsymbol{u}_{\mathrm{c}}. \tag{2.15}$$

It is the energy propagation velocity of the wave train. Note that wave energy may be advected by a current field $\boldsymbol{u}_{\mathrm{c}}$, whose depth dependence is considered as approximated by a near surface mean in this study. An observer moving with the group velocity describes a space curve $\boldsymbol{x}(t)$ characterized by $\dot{\boldsymbol{x}} = \boldsymbol{v}_{\mathrm{g}}$. These curves are termed rays. For motion on rays, the Hamilton equations

$$\begin{aligned} \dot{\boldsymbol{x}} &= \partial_{\boldsymbol{k}} \Omega \\ \dot{\boldsymbol{k}} &= -\partial_{\boldsymbol{x}} \Omega \\ \dot{\Omega} &= \partial_t \Omega \end{aligned} \tag{2.16}$$

follow from the definitions of group velocity (2.15), and the definitions of local wave vector and local circular frequency (2.11). The dynamics of wave trains in slowly varying inhomogeneous media, i.e. the evolution of the amplitudes $a(\boldsymbol{x}, t)$, are governed by the conservation of action density

$$N(\boldsymbol{x}, t) \equiv 2|a(\boldsymbol{x}, t)|^2/\sigma \tag{2.17}$$

of the wave train (Bretherton et al. 1969).

To obtain a general description of the sea surface for slowly varying inhomogeneous media, the linear combination of normal mode solutions of the homogeneous system (2.5) is replaced by a superposition of wave trains of the form (2.10). The expression for the spatially mean energy density $\overline{E}$ then becomes a function of $\boldsymbol{x}$ and t on the large scales

$$\overline{E}(\boldsymbol{x}, t) = 2\rho g \int \mathrm{d}\boldsymbol{k}\, |a(\boldsymbol{k}(\boldsymbol{x}, t), \boldsymbol{x}, t)|^2. \tag{2.18}$$

The corresponding generalized definition for the wave spectrum then reads

$$F(\boldsymbol{k}(\boldsymbol{x}, t), \boldsymbol{x}, t) \equiv 2\, \langle |a(\boldsymbol{k}(\boldsymbol{x}, t), \boldsymbol{x}, t)|^2 \rangle. \tag{2.19}$$

Willebrand (1975) showed that in the case of a wave field consisting of a superposition of wave trains, the conservation of action holds for each individual wave train. This led to a balance equation for the spectral action density

$$N(\boldsymbol{k}(\boldsymbol{x}, t), \boldsymbol{x}, t) \equiv F(\boldsymbol{k}(\boldsymbol{x}, t), \boldsymbol{x}, t)/\sigma = 2\langle |a(\boldsymbol{k}(\boldsymbol{x}, t), \boldsymbol{x}, t)|^2 \rangle/\sigma \tag{2.20}$$

of the form

$$\partial_t N + \partial_{\boldsymbol{x}} \cdot (\dot{\boldsymbol{x}} N) + \partial_{\boldsymbol{k}} \cdot (\dot{\boldsymbol{k}} N) = 0, \tag{2.21}$$

in which the "dot terms" $\dot{\boldsymbol{x}}$ and $\dot{\boldsymbol{k}}$ are given by the Hamilton equations (2.16).

Statistical Description for Slowly Varying Media. The statistical theory of the sea surface can be generalized in an analogous manner by replacing the requirement of statistical homogeneity and stationarity by quasi-homogeneity and quasi-stationarity. To this end two scales are distinguished, similar to the definition of slowly varying wave trains. The statistics may vary slowly on large scales, but not strong enough to have a considerable influence on the homogeneity and stationarity of the wave statistics on scales relevant for individual waves. In this way, the two-point covariance function describing the statistical information of the nearly Gaussian wave field can be generalized to a function of $\boldsymbol{x}$ and t on the large scales. Since the wave spectrum is defined as Fourier transform of the covariance function, cf. equation (2.9), it directly inherits this feature.

Both defining approaches for the wave spectrum have been generalized consistently to quantities dependent on space and time. The concept of the wave spectrum as mathematical representation of the sea state is therefore suitable for the use in wave models.

2.1.1.2 Wave Spectra and Integrated Parameters

For practical purposes, wave spectra can be given in different representations as functions of generalized wave vector coordinates, say $\boldsymbol{\kappa}$. To obtain a representation $\tilde{F}(\boldsymbol{\kappa})$ according to these, the transformation $\boldsymbol{k} \mapsto \boldsymbol{\kappa}$ must be performed with the condition

$$\tilde{F}(\boldsymbol{\kappa})\mathrm{d}\boldsymbol{\kappa} = F(\boldsymbol{k})\mathrm{d}\boldsymbol{k}. \tag{2.22}$$

It ensures that the spatially mean energy densities connected to each representation are equal. The transformation is defined only in the case of coordinates $\boldsymbol{\kappa}$ with existing nonzero Jacobian $|\mathrm{d}\boldsymbol{\kappa}/\mathrm{d}\boldsymbol{k}|$. A common representation is the frequency direction spectrum $E(f,\theta)$. Further examples are given in appendix (A.1). In A.1, definition and features of one-dimensional frequency spectra $E(f)$ are discussed in addition, including a definition of peak frequency which will be needed in chapter 3.

Integrated parameters of the wave spectrum can be statistically interpreted as observables of the sea state which is described by the spectrum. In this way, wave model results can be related to measurements. Integrals of $E(f,\theta)$ containing powers of f are called moments of the spectrum. The most important moments are

$$m_n \equiv \int \mathrm{d}f\mathrm{d}\theta E(f,\theta) f^n, \quad n = -1, 0, 1, 2. \tag{2.23}$$

Moment m_0 is called total energy or total variance of the spectrum. It can be obtained equivalently as integral of any representation of the wave spectrum, e.g. as

$$m_0 = \int \mathrm{d}\boldsymbol{k} F(\boldsymbol{k}). \tag{2.24}$$

The total energy defines the integrated parameter significant wave height

$$H_\mathrm{S} \equiv 4\sqrt{m_0}\,. \tag{2.25}$$

Different integrated periods are defined as

$$\text{mean period } \langle T \rangle \equiv \frac{m_{-1}}{m_0}, \quad T_{\mathrm{m1}} \equiv \frac{m_0}{m_1}, \quad T_{\mathrm{m2}} \equiv \sqrt{\frac{m_0}{m_2}}. \tag{2.26}$$

The mean wave-vector direction is given by

$$\langle \theta \rangle \equiv \arctan\left(\frac{\int \mathrm{d}f\mathrm{d}\theta E(f,\theta)\sin\theta}{\int \mathrm{d}f\mathrm{d}\theta E(f,\theta)\cos\theta}\right). \tag{2.27}$$

The integrated parameters of the wave spectrum are related to observables of the sea state as follows. The significant wave height H_S corresponds to the wave height $H_{1/3}$ defined as mean of the highest third of observed waves (Longuet-Higgins 1963). The integrated period T_{m2} corresponds to the zero-upcrossing period T_z, for a definition cf. Goda (1985). Finally, the parameter $\langle\theta\rangle$ can be interpreted as mean wave direction.

2.1.2 Dynamical Equation for Wave Spectra

To predict the sea state as function of initial and boundary sea states and the influence of external fields, spectral wave models numerically solve a dynamical equation for the wave spectra. This dynamical equation is the action balance equation

$$\partial_t N + \partial_{\boldsymbol{x}} \cdot (\dot{\boldsymbol{x}} N) + \partial_{\boldsymbol{k}} \cdot (\dot{\boldsymbol{k}} N) = S(N). \tag{2.28}$$

for the wave action spectrum $N \equiv F/\sigma$. The equation is a generalization of the conservation equation (2.21). It is valid for a wave field consisting of a superposition of slowly varying inhomogeneous wave trains. In the case of zero currents $\boldsymbol{u}_\mathrm{c}$ the spectral action density N can be replaced by the wave energy spectrum F in (2.28). The left-hand side of the equation describes the local change (∂_t-term), propagation ($\partial_{\boldsymbol{x}}$-term), and refraction ($\partial_{\boldsymbol{k}}$-term) of spectral action density as balance in flux form. It is therefore shape-invariant in a transformation to generalized coordinates as described in subsection 2.1.1. The right-hand side of (2.28) describes the total influence of external processes leading to sources and sinks of energy (action). These sources and sinks can be described as weak, homogeneous perturbations in the dynamics of the Gaussian wave field. From this follows that the individual source functions representing different processes are functionals of the wave spectrum (or wave-action spectrum) and can be added independently to the dynamical equation for the wave spectrum (Komen et al. 1994). Both features are expressed in the equation

$$S(N) = S_\mathrm{in} + S_\mathrm{nl} + S_\mathrm{dis} + S_\mathrm{bot}, \tag{2.29}$$

describing input by wind, quadruplet nonlinear interactions, dissipation by bottom interactions, and dissipation by white capping. The individual terms will be discussed in the following paragraph. Note that in many cases expressions for the source functions were originally given in terms of energy density F, defined with respect to a balance equation for F shape-similar to (2.28) (WAMDI 1988). It will be valid if currents are absent. In what follows, generally valid expressions in terms of N will be used. They are shape-similar to the original expressions.

2.1.2.1 Source Functions

Energy Input by Wind. In spectral wave modelling, energy input to the wave field by wind is usually given in terms of friction velocity $u_* \equiv \tau^{1/2}$ defined with the (kinematic) surface wind stress $\tau = c_\mathrm{d} u_{10}^2$. The surface wind stress depends on wind speed at a certain height, here 10 m, and on the drag coefficient c_d, which has to be determined e.g. by a wind-dependent parametrization as given in Wu (1982). The influence of the sea state on the drag coefficient also plays a crucial role, cf. theories on the drag of the sea surface by Janssen et al. (1989) and Makin et al. (1995). See also Komen et al. (1994) for an overview on this subject.

The input term has the general form

$$S_\mathrm{in} = \alpha + \beta N. \tag{2.30}$$

The constants α and β describe energy input leading to wave growth linear and exponential in time, respectively.

The linear-growth input results from interaction of the wave field with atmospheric turbulence (Phillips 1957). It is independent of the wave spectrum, thus resulting in time linear growth. Parametrizations of α contain the wind speed, or friction velocity, to the power of 4, as in Phillips (1977), Cavaleri et al. (1981), and Tolman (1992).

The exponential-growth input results from interaction of the waves with shear flows above them (Miles 1957). The energy input to the spectrum at a selected wave vector is proportional to the spectral level at that wave vector. This leads to an instability and exponential growth in time. The growth parameter β was measured by Snyder et al. (1981). Earlier observational studies are collected in Plant (1982). A parametrization of β linear in the wind speed at 5 m height was given by Snyder et al. (1981). It was reformulated in terms of friction velocity u_* by Komen et al. (1984). This parametrization was used e.g. in the third-generation model WAM (WAMDI 1988). It reads

$$\beta = \beta_0 \omega \max\left(28\frac{u_*}{c}\cos\theta - 1,\, 0\right), \quad \beta_0 = 0.25\frac{\rho_\mathrm{a}}{\rho_\mathrm{w}} \approx 0.0003\,, \tag{2.31}$$

with symbols c phase velocity, ρ_a and ρ_w densities of air and water, and θ the relative angle of wind and wave vector.

Plant (1982) and Donelan et al. (1987) used expressions for β quadratic in the wind speed for young, strongly forced wind sea. A combination of the linear and quadratic wind-speed dependence of β was used e.g. by Banner et al. (1994). An expression for the growth rate β and the wave influence on the drag of the sea surface given by Janssen (1989, 1991) is applied in WAM cy. 4 (Günther et al. 1992).

Computations of β via boundary-layer models have been performed e.g. by Burgers et al. (1993) and Chalikov et al. (1993). The latter results have been used in parametrized form in a wave model by Tolman et al. (1996).

Quadruplet Nonlinear Interactions. The weak nonlinearity of ocean waves can be treated as homogeneous perturbation in the linear dynamics of slowly varying wave spectra (Komen et al. 1994). It therefore enters the wave-spectrum dynamics via a source term in the action balance equation. The theory of energy transfer in a gravity-wave spectrum due to quadruplet nonlinear interactions was given by Hasselmann (1962, 1963a, 1963b). According to this theory, variations of the wave spectrum at a regarded wave vector are caused by resonant four-wave interactions which can be computed by evaluation of a six-dimensional Boltzmann integral. Phillips (1981) gave a reviewing article of the theory of nonlinear interactions. Numerical algorithms for the computation of the Boltzmann integral have been developed, e.g. the symmetrical method by Hasselmann et al. (1981, 1985a), and the method of Resio et al. (1991). Further research on quadruplet interactions in the case of finite water depth can be found in Herterich et al. (1980), Polnikov (1997), and Lin et al. (1997). A shallow-water extension of the numerical method of Resio was used in Cardone et al. (1998). The numerical algorithms have been used in one-dimensional wave models for the study of the quantitative influence of nonlinear interactions in idealized cases, e.g. on the existence of an equilibrium sea state (Komen et al. 1984), on the energy balance in finite depth waters (Weber 1988), on the response of wave spectra to turning winds (Young et al. 1987, van Vledder et al. 1993), and in recent studies (Young et al. 1993,

Banner et al. 1994). However, the numerical solution methods of the exact Boltzmann integral are still too expensive in regard to computing resources of operational spectral wave models. Therefore approximations are usually carried out, e.g. the discrete interaction approximation (DIA) by Hasselmann et al. (1985b) used in WAM cy. 4.

Dissipation of Wave Energy. Energy dissipation in spectral wave modelling is usually attributed to wave breaking (white capping) at the water surface and, in the case of shallow water, to interaction processes at the bottom boundary, including bottom friction, percolation, and bottom elasticity. An overview of the bottom interactions is given in Weber (1994) and Komen et al. (1994). Bottom interaction models used as source functions S_{bot} in spectral wave models have the general form

$$S_{\mathrm{bot}} = -\Gamma\sigma^{-2}k^2(1-\tanh^2 kh)N, \tag{2.32}$$

in which the interaction coefficient Γ depends on the used bottom interaction model. Examples are the drag-law model of Hasselmann et al. (1968) used in Hasselmann et al. (1973) for swell-decay analysis and the spectral eddy-viscosity model by Weber (1991). The influence of different models on the shallow-water wave-energy balance was analysed by Luo et al. (1994). Most wave models use a constant interaction coefficient Γ, e.g. WAM cy. 4 and SWAN (Booij et al. 1998).

Energy dissipation by white capping is the least known process in the energy balance of the wave spectrum. It is generally accepted that parametrizations of white capping in spectral wave models must obey a quasilinear form

$$S_{\mathrm{dis}} = -\gamma N, \tag{2.33}$$

with the interaction parameter γ a functional of the wave spectrum (Hasselmann 1974). Usually, γ is given as function of spectral mean period, energy, and steepness parameters (Donelan 1994). The white-capping source function is commonly parametrized and tuned in spectral wave models to give the correct spectral energy content for fully developed spectra (Komen et al. 1984). The parametrization thus depends on the chosen parametrization of the wind input. For this reason, different white-capping functions were used in 3G WAM (WAMDI 1988) and WAM cy. 4 (Günther et al. 1992).

Further Processes. For the purpose of applying spectral wave models to the coastal zone, a number of processes have been investigated and included as additional source functions e.g. in the near-shore wave model SWAN (Booij et al. 1998). These include depth-induced wave breaking with expressions according to Battjes et al. (1978) and Eldeberky et al. (1995), and triad nonlinear interactions of waves according to Eldeberky et al. (1996). An assessment of the relevance of diffraction effects in coastal wave-modelling applications was given by Cardone et al. (1998).

2.1.3 Model Generations

A brief historical perspective of spectral wave modelling is given in this subsection in order to enable comparisons of the modelling approach investigated in this thesis with existing wave

models. After the introduction of the concept of a wave spectrum by Pierson et al. (1955), the first wave model based on a dynamical equation for the spectrum was given by Gelci et al. (1956). Since then, many spectral wave models have been developed, reflecting the growing understanding of the wave-energy balance. Today, spectral wave models are commonly classified into three generations (Komen et al. 1994). Nine models of first and second generation were analysed and intercompared in SWAMP (1985). A short characterization of the generations follows here.

In first-generation models, the wave spectrum is discretized to energy levels at a finite number of frequency-direction bins corresponding to discrete frequency and direction axes. Wave energies in the individual spectral bins develop independently from each other. Nonlinear interactions are neglected. In the first generation models in SWAMP (1985), the wind input is represented by a combination of linear and exponential growth. Dissipation is not treated explicitly. It is introduced by an artificial energy cutoff at a level prescribed by a parametrized spectral form dependent on the wind speed. An example is the VENICE model of Cavaleri et al. (1981).

Second-generation models take into account nonlinear interactions implicitly or in rather poor parametrization, corresponding to coupled hybrid and coupled discrete models as described in SWAMP (1985). For example, in coupled hybrid models, the wind-driven part of the spectrum is parametrized as self-similar spectral shape depending on a few parameters, e.g. the JONSWAP spectrum (Hasselmann et al. 1973). The development of the spectrum can then be represented by a mapping of the spectral dynamical equation onto equations of motion for the parameters. The swell part of the spectrum is treated independently, similar to first-generation models. An example is the wave model HYPA (Günther et al. 1979). A disadvantage of coupled hybrid models is the prescribed spectral form which cannot be valid in full generality, e.g. in complex instationary and inhomogeneous situations. Another shortcoming is the artificial classification of wind sea and swell and the neglect of interactions between both.

As a result of the SWAMP (1985) intercomparison, it was decided to develop a third-generation wave model in which the wave spectrum was to be represented in a full two-dimensional discretization to avoid the limitations of a parametric model, and in which the physical processes were to be treated in state-of-the-art parametrizations. Especially the quadruplet nonlinear interactions were to be given in a form leaving enough degrees of freedom for the developing spectrum. The first third-generation model was 3G WAM (WAMDI 1988). Up to the present, quite a few others have followed, with improvements in the source-term parametrizations, especially the wind input, in the propagation numerics, and with extensions to shallow-water shelf seas and coastal areas. Examples are WAM cy. 4 (Günther et al. 1992), and in Tolman (1991), Bender (1996), Lin et al. (1996a, 1996b), and Tolman (1996).

Recently, third-generation spectral wave models have been adapted to applications in small-scale systems such as coastal waters and inland lakes. A stationary model for the coastal zone is the SWAN model (Booij et al. 1998). An extension to an instationary version is in progress. Numerical adaptions for the application of WAM cy. 4 to small-scale systems have been presented by Luo et al. (1998).

Third-generation models require significantly more computing power than first- and second-generation models. This stems from the fully discrete representation of the wave spectrum and

the expensive parametrization of the nonlinear interactions. This can be a major obstacle in the context of coupled modelling of atmosphere, water body, and sediments. For this reason, second-generation models, e.g. HYPAS (Günther et al. 1984), a shallow-water version of HYPA, are still popular and in frequent application, see e.g. Wolf et al. (1998).

2.2 Nonlinear Dissipation in Spectral Wave Modelling

The concept of nonlinear dissipation will be introduced in this section. The general shape for dissipation source functions will be reviewed from literature and supplemented. Its consistency with parametrizations of spectral wave dissipation as in use today will be worked out. A continuing discussion in the wave modelling community about the physical reasonability of nonlinear dissipation source functions will be outlined and interpreted. A nonlinear dissipation source function follows from parametrization of wave-energy dissipation by wave turbulence interaction. General consequences of a thus parametrized dissipation function on the wave-energy balance will be indicated.

2.2.1 General Shape of Dissipation Source Functions

The action balance equation (2.28) describing the large-scale evolution of the wave spectrum cannot be closed from first principles to yield a numerically solvable problem for the wave spectrum. The external perturbations summarized in the total source function S operate on length and time scales which are not necessarily resolved in the chosen wave-spectrum formulation. These processes must therefore be parametrized in some manner as functions of external parameters and of the spectrum itself to close the dynamical equation. In this subsection, common knowledge on the general form of the total source function is reviewed and applied as general approach to the nonlinear formulation of the dissipation source function. The purpose of this is to show that the specific nonlinear dissipation function treated in this thesis is formally consistent with this general shape.

Functional Power Series Expansion. It was reviewed in subsection 2.1.2 that the total source function S in the action balance equation (2.28) is a sum of terms representing individual physical processes. The terms are functionals of the wave spectrum and functions of parameters characterizing the process. This justifies a formal expansion of the total source term into a functional power series containing rising integral powers of the spectrum. This was done by Snyder et al. (1992), who identified the terms in the expansion with different processes. The expansion is purely formal. It cannot be argued that only the first few expansion orders will contribute significantly to the series, while higher order terms are neglectable. But the expansion will serve the purpose of clarifying the general shape of the source functions.

Snyder et al. (1992) attributed the dissipation to terms in the functional expansion starting at second order, arguing with an essentially nonlinear character of dissipation. The nonlinearity of dissipation is adopted in the present work. Snyder et al. (1992) pointed out further that purely dissipative terms in the expansion must be quasi-linear, i.e. containing the spectrum itself as factor, to avoid creation of negative energies in the course of spectral development.

A similar but not equivalent feature is the quasi-linearity of source functions pointed out by Hasselmann (1974).

Since dissipation appears as additive term in the total source function, the functional power-series expansion can be done for the dissipation alone. A general quasi-linear expression for the dissipation source function is accordingly

$$\begin{aligned} S_{\mathrm{dis}}(N) &= N(\boldsymbol{k})\{\int \mathrm{d}\boldsymbol{k}_1 \zeta(\boldsymbol{k},\boldsymbol{k}_1)N(\boldsymbol{k}_1) + \\ &\quad + \int\int \mathrm{d}\boldsymbol{k}_1\mathrm{d}\boldsymbol{k}_2 \eta(\boldsymbol{k},\boldsymbol{k}_1,\boldsymbol{k}_2)N(\boldsymbol{k}_1)N(\boldsymbol{k}_2) + \ldots\}. \end{aligned} \tag{2.34}$$

Dots indicate integrals with kernels containing the wave spectrum to powers greater than two. The expansion coefficients $\zeta(\boldsymbol{k},\boldsymbol{k}_1)$, $\eta(\boldsymbol{k},\boldsymbol{k}_1,\boldsymbol{k}_2)$, and higher order coefficients describe the physics of the dissipation process. They must be parametrized as functions of $\boldsymbol{k}$ and external parameters. Snyder et al. (1992) applied dimensional and symmetry analysis to obtain conditions for the general shape of the coefficients. They also suggested approximation of the dependence on $\boldsymbol{k}$ by Taylor-polynomial expressions. Two alternatives for the general nature of the $\boldsymbol{k}$ dependence of the coefficients are pointed out here. The integral expansion in (2.34) is a distribution mapping the wave spectra to real numbers. This distribution can be regular or singular. In the first case, the expansion coefficients can be given by functions of $\boldsymbol{k}$. In the second case, the coefficients contain delta functions of $\boldsymbol{k}$ in addition. Delta functions have been used e.g. by Snyder et al. (1992) for a formal derivation of a quasi-linear expression similar to (2.34) from a general functional expansion of the total source term. The question of the coefficients containing regular functions or delta functions must be addressed by an analysis of the physics of the specific process or by more general considerations. For instance, the introduction of delta functions to achieve quasi-linearity is needed to satisfy the condition of non-negativity of wave energy.

Second-order Nonlinear Dissipation. Consider a function $f(\boldsymbol{k})$ of wave vector and a Taylor-expandible function $g(m_0, m_1, \ldots)$ of the spectral moments. A dissipation source term of the form

$$S_{\mathrm{dis}} = f(\boldsymbol{k})g(m_0, m_1, \ldots)N^2(\boldsymbol{k}) \tag{2.35}$$

is treated in this thesis. It is consistent with (2.34) in the sense that specific expressions for the expansion coefficients exist for which (2.35) follows from (2.34). The proof of this statement is outlined in appendix A.2. It gives a formal justification for the use of a source term based on (2.35).

Other expressions. The white-capping source term of WAM (WAMDI 1988) can be written in general terms as

$$S_{\mathrm{dis}} = f(\boldsymbol{k})g(m_0, m_1, \ldots)N(\boldsymbol{k}), \tag{2.36}$$

with functions $f(\boldsymbol{k})$ and $g(m_0, m_1, \ldots)$ as above. The consistency of this expression with (2.34) can be shown with similar arguments as for (2.35), cf. appendix A.2. Further possible parametrizations of dissipation contain higher local powers of the wave spectrum. They can be justified analogously, again cf. appendix A.2. Examples are in Phillips (1985) and Donelan et al. (1987), where the spectrum appears to the power of three, or some higher power n.

2.2.2 On the Physical Reasonability of Nonlinear Dissipation

For the process of white-capping dissipation, the general validity of a source-function parametrization involving local powers of the wave spectrum similar to expression (2.35) has been questioned by K. Hasselmann as reported by Snyder et al. (1992) and Donelan et al. (1994). This has led to a continuing discussion on the subject within the wave modelling community. The essentials of the discussion will be summarized here to clarify subsequently the physical reasonability of the nonlinear dissipation source function (2.35).

Hasselmann has given a counterexample to show a violation of the general validity of expression (2.35) in the case of white-capping dissipation. In the example, two narrow-banded swell spectra are considered with equal total energy, mean frequency, rms slope, and directional distribution. The spectra differ only in spectral band width. Following from this, the total dissipation according to equation (2.35) must be different, although the local Rayleigh statistics of the wave fields are the same. Since the degree of white capping exclusively depends on local properties, differing total white-capping dissipations for the two wave fields cannot be justified by any physical argument (cf. Donelan et al. 1994). It is stressed here that Hasselmann's counterexample applies only to dissipation processes which are essentially local in physical space, i.e. confined to a spatial region smaller than a wave length. Dissipation by random breaking events is such a process.

A number of authors have pointed out that special cases exist in which a $\boldsymbol{k}$-space-local parametrization of white-capping dissipation is reasonable, e.g. in the context of the analysis of equilibrium ranges and radar scattering (Phillips 1985, Plant 1986, Donelan et al. 1987). Snyder et al. (1992) have indicated special situations in which an expression (2.35) is useful for the complete wind-wave spectrum. Donelan (1995) and Donelan et al. (1998) have pointed out a $\boldsymbol{k}$-local balance of input and dissipation at the spectral peak in case of strongly forced, depth-limited wind seas.

There is also some controversy about the essential physical-space-local character of white capping. Laboratory studies are described in Donelan et al. (1994), which show that energy loss due to white capping is usually confined to spectral bins close to the breaking wave. In contrast to Hasselmann, this suggests a $\boldsymbol{k}$-local parametrization of the source function.

Important for the present work is the conclusion that to physical processes which can be understood to operate nonlocally in physical space, Hasselmann's counterexample does not apply. For such processes, a parametrization of the form (2.35) is not a priori physically incorrect.

2.2.3 Dissipation by Turbulent Diffusion

In deep water, the dissipation of wave energy has been principally regarded as caused by random wave breaking, also called white capping (Donelan 1994). In a different approach, the dissipation of surface waves is regarded as mainly due to interaction of the waves with upper-oceanic turbulence, as described e.g. in Kitaigorodskii et al. (1983b). In deep-water systems, turbulence in the layer from the surface to a depth where surface wave motion ceases can be understood to be in part caused by wind stress resulting in white capping, but other sources of turbulence can also exist. Individual breaking events give small contributions to a general turbulence level which is described on the scales of the wave field. The individual normal modes of the wave

field can be thought to interact independently with this large-scale mean turbulence. Thus, this interaction can be understood as mainly local in $\boldsymbol{k}$ space. The degree of white capping has influence on this dissipation, but only in a mean, integral manner by contribution to the level of turbulence. The local physics of individual breaking events is thus insignificant in considerations on the general shape of the corresponding source function.

Wave turbulence interaction has been described by several authors, see e.g. Kitaigorodskii et al. (1968), Phillips (1977), Kitaigorodskii et al. (1983b), and Rosenthal (1989). An approach for the treatment of turbulence in connection with wave dynamics is usually the decomposition of the wave flow field into mean flow plus turbulent fluctuations with zero mean. In the momentum balance of the mean flow, a term then appears which contains covariances of the fluctuating part. These are the Reynolds stresses, which are interpreted to sustain a downward flux of wave momentum. The Reynolds stresses can be parametrized proportional to the vertical gradient of the mean flow, including a proportionality constant called turbulent eddy viscosity (Pedlosky 1987, Rosenthal 1989). Two different eddy-viscosity models of this kind have been used to give parametrizations for dissipation terms which can be used in spectral wave models. One was recently given by Tolman et al. (1996). In this thesis, a parametrization according to Rosenthal (1989) is used.

The parametrization of Rosenthal (1989) was obtained by insertion of the first-order Stokes solution for the wave field, including Stokes drift, into the momentum balance of the wave flow field. The Stokes drift has non-vanishing vorticity, it is thus retained in the eddy-viscosity expression for the Reynolds stresses. An energy balance equation can be obtained from the momentum balance. Since the wave amplitudes appear squared in the Stokes drift expression, this yields a total-energy dissipation proportional to amplitude to the power of four, i.e. squared in energy of the normal-mode wave (Rosenthal 1989). Since dissipation by wave turbulence interaction operates locally in $\boldsymbol{k}$ space, a parametrization follows in which the wave spectrum appears locally squared:

$$S_{\mathrm{dis}} = \gamma(\boldsymbol{k}, \ldots) N^2(\boldsymbol{k}) \,. \tag{2.37}$$

This formulation is equivalent to expression (2.35). It is thus formally consistent with the general shape of a dissipation source function as given in (2.34). The locally nonlinear shape is physically reasonable, since the described process operates locally in $\boldsymbol{k}$ space.

The $\boldsymbol{k}$ dependence of the coefficient γ can be given by dimensional arguments. The coefficient depends on the turbulent eddy viscosity. It can depend on various parameters affecting the level of turbulence. This is indicated by the dots in equation (2.37). Parameters can include integral parameters of the wave spectrum to account for enhanced dissipation of short waves in the presence of long waves, water depth to account for turbulence generated at the bottom boundary layer, wind stress to account for enhanced white capping, and currents. A specification of $\gamma(\boldsymbol{k}, \ldots)$ as used in the model computations in this thesis will be given in the context of the model formulation, see section 2.3.

2.2.4 Consequences for the Wave-Action Balance

The use of a nonlinear dissipation source function of the form (2.37) in a spectral wave model, together with a linear wind input source function, has substantial consequences on the wave-action

balance. For the present discussion, advective effects and quadruplet nonlinear interactions of waves will be neglected. Systems with neglectable nonlinear interactions exist, as was pointed out by Snyder et al. (1992). Advective effects will cancel in the case of homogeneous systems.

Resulting from the local powers of the wave spectra in the two source terms, the spectrum will develop towards a local equilibrium between input and dissipation at each wave number. A fully developed spectrum thus exists, which is determined only by the parametrizations of wind input and nonlinear dissipation.

The equilibrium range of the spectrum will result as power-law function of wave number. Its specific form will be analysed explicitly in the next chapter. Since the wind-input parametrization also contributes to its shape, the energy level of the equilibrium range will be wind-dependent. This is consistent with general knowledge (Phillips 1985). The form of the equilibrium range is usually interpreted as energy cascade maintained by nonlinear interactions. These result in a flux of energy from generation at low wave numbers to dissipation at very high wave numbers (Kitaigorodskii 1983a). According to this view, the equilibrium range is shaped by a dynamical balance. Kitaigorodskii et al. (1983b) have pointed out, however, that the balance can alternatively be due to a local balance of wind input and dissipation by wave turbulence interactions, as is the case in the present study.

Besides the equilibrium range, the spectral peak can be determined by a local balance of wind input and dissipation in special cases, as was suggested by Donelan et al. (1995, 1998). With the use of nonlinear dissipation, a $\boldsymbol{k}$-local balance is possible throughout the spectrum. It is thus formally possible to run a wave model with these processes without prescribing a spectral form to introduce an artificial limit of wave growth. This will be an advantage if complex advective effects destroy the self similarity of the wind wave spectrum, i.e. if a parametrical spectral form can no longer be applied.

2.3 Formulation of a Wave Model with Nonlinear Dissipation

Nonlinear dissipation in spectral wave modelling will be analysed in this thesis by performance of numerical experiments with a wave model. The formulation of the model is the subject of this section. Since the model solves the action balance equation in wave-number and direction coordinates, it has been internally called K-model. The name will be adopted as alternative to "the wave model" in subsequent parts of the text.

2.3.1 Conceptual Idea of the Model

The general aim of the analysis of nonlinear dissipation in spectral wave modelling in this thesis is the development of a wave model for applications in coastal systems. Such systems are characterized by small length scales and time scales, by tides leading to space- and time-varying water depths and currents, and by wind fields variable on small scales. The conceptual idea of the wave model is closely related to this general aim. It can be characterized as follows:

1. The sea state to be predicted in coastal systems will depend on a complex interplay of developing wind sea, depth limitation, and advective effects. A standard self-similar

spectral shape cannot be expected. Therefore the wave model must resolve the full two-dimensional wave-action spectrum at each grid point.

2. In small-scale coastal applications it can be feasible in special cases to treat wave modelling in stationary approximation (Holthuijsen et al. 1993). This is the case in applications where nearly fully-developed wind seas and swell approach an open coastline. In this thesis, partially enclosed systems mainly dominated by local wind waves will be analysed. For these, it is inevitable to use an instationary wave model. This will be shown in chapter 4.

3. The source functions of the wave model should be simple. Considerable computing resources are needed for the resolution of inhomogeneous advective effects and for the computation and supply of instationary water depths, currents, and winds. Furthermore, coupled modelling of atmosphere, water body, and sediment is a far-range aim.

4. Existing third-generation ocean wave models consider weakly nonlinear waves in a nonlocal, dynamical balance with basically linear source functions. In contrast to this, the wave model presented in this thesis describes linear waves in a local balance of linear wind input and nonlinear dissipation. This conceptual idea satisfies the requirement of simple source functions. In particular, an explicit treatment of quadruplet nonlinear interactions is abandoned. This will be justified in subsection 2.3.2.

5. The choice of spectral action densities as prognostic fields and wave vector modulus and direction (k, θ) as independent coordinates reflects the need for an instationary treatment in full generality. This will be shown in subsection 2.3.6.

Consistent with these general ideas, the action balance equation used in the wave model is

$$\partial_t N + \partial_{x_1}(\dot{x}_1 N) + \partial_{x_2}(\dot{x}_2 N) + \partial_k(\dot{k} N) + \partial_\theta(\dot{\theta} N) = S(N). \tag{2.38}$$

It is given in flux form and is thus shape-similar to the formulation (2.28). The sum of source functions is

$$S(N) = S_{\mathrm{in}} + S_{\mathrm{phil}} + S_{\mathrm{dis}} + S_{\mathrm{bot}}, \tag{2.39}$$

consisting of a modified Snyder input S_{in}, modified Phillips input S_{phil}, dissipation by wave turbulence interaction S_{dis}, and dissipation by bottom interactions S_{bot}.

With respect to the neglect of nonlinear interactions, the wave model is comparable to first-generation spectral wave models as described in subsection 2.1.3. But it is stressed that the dynamical concept of the wave model is different. First- and second-generation models are based on presribed spectral shapes and therefore cannot be applied in systems where deviations from these shapes are expected. In particular, the influence of currents cannot be studied in these models, as Doppler shifting cannot be resolved in a prescribed spectral shape.

The technical development of the wave model was carried out on the basis of the WAM cy. 4 code. Major changes were:

1. Replacement of the source functions

2. Transformation to action density in (k, θ) as prognostic fields

3. Various technical details to enable small-scale and instationary applications.

The numerical schemes and e.g. the file handling were adopted from the WAM code.

One striking feature of the wave-model conceptual idea described in this subsection is the neglect of quadruplet nonlinear interactions. This will be motivated and justified in detail in the following subsection.

2.3.2 On the Neglect of Quadruplet Nonlinear Interactions

The significance of nonlinear energy transfer in the development of ocean wave spectra was pointed out by various authors in studies dating back to 1962, see e.g. Hasselmann (1962), Hasselmann et al. (1973), Hasselmann et al. (1976), Phillips (1981), and more recent papers by Young et al. (1993), Lin et al. (1997), Cardone et al. (1998), and Young et al. (1998), just to mention a few. This thoroughly established consensus has given rise to consideration of the process also in coastal wave modelling, see e.g. SWAN (Holthuijsen et al. 1993, Ris 1997, Booij et al. 1998) and WAM (Luo et al. 1998). The related source term is based on shallow-water extensions of numerical algorithms as in use in ocean wave models, cf. section 2.1. The extended algorithms are parametrizations of energy transfer due to quadruplet nonlinear interactions of shallow-water waves in homogeneous systems.

With respect to the foregoing, the neglect of nonlinear energy transfer in a spectral wave model may seem like an uneducated disregard of major scientific results obtained by various independent investigators during the past four decades. But this is not the case. We agree to the significance of nonlinear energy transfer in oceanic systems, but object to the use of identical numerical algorithms in coastal inhomogeneous applications. In these applications, nonlinear transfer clearly plays a considerable role, but more basic research is needed to give an explicit source term for use in a spectral wave model for coastal areas. This point will be further elucidated in the following paragraphs.

Regarding scales of spatial and temporal variability of the wave-supporting medium, coastal environments have a different quality than oceans. Inhomogeneity in oceanic systems is mainly caused by spatial atmospheric pressure variability introducing variations in the driving wind fields on scales of 10 km to 100 km. In a first approximation neglecting orographic effects, winds in coastal environments can be treated as spatially constant. But inhomogeneity is imposed in these systems by water-depth and current fields varying on scales of 1000 m to 100 m and less. Propagation effects thus strongly gain in significance, cf. Cardone et al. (1998). These authors gave an assessment of the significance of different source functions and propagation effects for varying water depths and bottom slopes. However, due to decreasing water depths, quadruplet nonlinear interactions always remained comparable to propagation effects in oder of magnitude. But nonlinear interactions were computed with shallow-water theory of nonlinear interactions in homogeneous systems, because a readily applicable theory for inhomogeneous systems does not exist.

This point is the major source of objection to the use of state-of-the-art nonlinear source functions from ocean wave models in spectral wave models for coastal areas. In the Hasselmann (1961) theory, strict homogeneity and stationarity of the wave field must be assumed, for instance to enable formal transitions of time to infinity for obtaining asymptotic integral expressions. Via

the dispersion relation for water waves, such a transition is connected also to a transition to spatial infinity. But in coastal systems media can already change in distances comparable to a few ten wave lengths. Therefore, the assumption of homogeneity is definitely violated. It must be concluded that a theory of random nonlinear waves in homogeneous media can give rise to serious errrors in applications to inhomogeneous coastal systems. A quantitative assessment of such errors requires a considerable amount of basic theoretical work to establish the theory of weakly nonlinear random waves in inhomogeneous media. It is therefore beyond the scope of this study.

It can be justified to bypass the missing knowledge on an extension of effects of weak nonlinearity to inhomogeneous systems by using a first-guess approach and apply the original method for homogeneous systems. This is done in most approaches to spectral wave modelling in coastal areas. A second possibility is to neglect the process of weak nonlinearity altogether. This approach is chosen in this study. It is justified by the assumption that except for some basic qualitative features, the nonlinear source function as in use in ocean wave models can produce a number of unrealistic quantitative effects leading to errors in the evolution of wave spectra in inhomogeneous small-scale systems. This assumption is additionally supported by the poor quality of the state-of-the-art parametrization of the nonlinear term, i.e. DIA, present already in homogeneous applications. DIA can deviate from exact numerical solutions of the nonlinear transfer term by an amount in the order of 100 per cent, see e.g. Komen et al. (1994). This leads for instance to unrealistic results for directional spread of spectra (Cardone et al. 1998). The poor quality of DIA was recognized early, but it was nevertheless adopted simply because basic features were reproduced qualitatively and a wave model using the parametrization was able to reproduce empirical growth laws (Komen et al. 1994).

To summarize it is concluded that the use of standard parametrizations of nonlinear transfer, e.g. DIA, in inhomogeneous systems is a source of uncertainty and can lead to substantial errors for two reasons. First, the theoretical basis for quadruplet interactions in inhomogeneous systems is not clear. Second, the parametrization is poor. This conclusion suggests the decision to neglect nonlinear processes in coastal wave modelling as a first step. Justification of this approach will be given in this thesis in similar manner as the use of DIA was justified for ocean wave models: it will be shown in chapter 3 that a wave model with nonlinear dissipation and neglect of nonlinear energy transfer can reproduce qualitative features and empirical laws of wave growth. A most welcome additional aspect of neglecting a DIA source term is a considerable reduction of needed computing resources, which adds to the feasibility of coupled simulations of coastal environments.

2.3.3 Propagation and Refraction

In this subsection, the left-hand side of the action balance equation (2.38) is discussed. The terms on the left-hand side containing divergences involving gradients $(\partial_{x_1}, \partial_{x_2})$ and $(\partial_k, \partial_\theta)$ with respect to location $\boldsymbol{x}$ and wave vector (k, θ) describe conservative fluxes of wave action in physical space and spectral space respectively. These are identified as wave energy propagation and refraction. The term refraction is used here in a more general sense including fluxes in wave number k besides the fluxes in θ. Since equation (2.38) can be given in its form in any

set of generalized coordinates, the explicit formulations for propagation and refraction depend only on the expressions for the "dot terms" $\dot{x_1}$, $\dot{x_2}$, $\dot{k}$, and $\dot{\theta}$, which depend on the chosen set of coordinates.

The dot terms are obtained from the dispersion function for linear wave trains Ω, equations (2.13) and (2.14), via the Hamilton equations (2.16). The expressions for $\dot{x_1}$ and $\dot{x_2}$ are readily identified as components of the wave group velocity field (2.15), these are

$$\dot{x_1} = v_\mathrm{g} \sin\theta, \quad \dot{x_2} = v_\mathrm{g} \cos\theta. \tag{2.40}$$

The dot terms of wave number and direction can be obtained after a short calculation:

$$\begin{aligned} \dot{k} &= -(\sin\theta \partial_{x_1}\Omega + \cos\theta \partial_{x_2}\Omega) \\ \dot{\theta} &= -(\cos\theta \partial_{x_1}\Omega + \sin\theta \partial_{x_2}\Omega) k^{-1}. \end{aligned} \tag{2.41}$$

The space derivatives of the dispersion function Ω can be grouped into two additive terms involving exclusively derivatives of the water-depth field or current field, respectively. Thus, the dot terms can be written as sums

$$\dot{k} = \dot{k}_\mathrm{D} + \dot{k}_\mathrm{C}, \quad \dot{\theta} = \dot{\theta}_\mathrm{D} + \dot{\theta}_\mathrm{C}, \tag{2.42}$$

where the subscripts D and C denote depth and current refraction. This enables a separate numerical treatment of propagation, depth refraction, and current refraction with individual time steps for each. The refraction dot terms are listed explicitly in appendix A.3. The fact that time derivatives of the dispersion function do not appear in the dot terms will be advantageous if instationary fields are treated, see subsection 2.3.6.

It is understood from the expressions for the dot terms that wave-action fluxes in physical and spectral space are influenced by water depths and currents. Effects of time-independent fields are shoaling and refractions caused by depth and current gradients. These are also included in state-of-the-art third-generation ocean wave models.

Wave blocking by opposing currents occurs in the presence of strong current velocities reaching the magnitude of the intrinsic wave-group velocity. For wave models with circular frequency ω as independent variable this leads to formal restrictions, since in this case a zero Jacobian would be involved in the transformation from (k_1, k_2) to (ω, θ) variables, cf. appendix A.1. Obviously, this formal problem does not appear in the present formulation of the model. Another way of avoiding the problem is the choice of intrinsic frequency σ as independent variable. This was done e.g. in WAM cy. 4 (Günther et al. 1992) and SWAN (Holthuijsen et al. 1993, Ris 1997). Note, however, that the wave-blocking problem in spectral wave modelling is only formally avoided by the choice of suitable coordinates. The physics of blocking cannot be described in the wave-train approximation given in equation (2.10) (Shyu et al. 1990).

2.3.4 Source Functions

The sum of source functions used in the wave model has been given in equation (2.39). In this subsection, the individual terms are discussed in detail. For the objectives of this thesis the discussion of the source functions is very important, because the general behaviour of a wave model with nonlinear dissipation to be analysed in this study strongly depends both on the individual formulations and the joint behaviour of all terms.

Wind Input. Wave-energy input by wind is parametrized in the wave model by a modified Snyder input term $S_{\rm in}$ and a modified Phillips input term $S_{\rm phil}$. In the present state of development of the K-model the friction velocity in the input source functions has been replaced by the wind speed in 10 m height using a fixed relation $28u_* \mapsto 1.2u_{10}$. It corresponds to the fixed value of the drag coefficient chosen in SWAMP (1985). The formulas will be given in terms of friction velocity, however.

The Snyder wind input was adopted from WAMDI (1988), and modified to include the effect of wind gustiness. To this end, the modulus of friction velocity is assumed as Gaussian process describing fluctuations not resolved in the model time scale. The effect of this was analysed in Komen et al. (1994). These authors obtained an effective input function by taking a sub-scale mean. The source function reads

$$S_{\rm in} = \beta_0 \, \sigma \, G \, N(\boldsymbol{k}), \tag{2.43}$$

where β_0 is a constant. The gustiness parameter G is given by

$$G = \frac{\sigma_{u_*}}{\sqrt{2\pi} c_*} \exp\left[-\frac{(c_* - u_*)^2}{2\sigma_{u_*}^2}\right] + \frac{1}{2}\left[\frac{u_*}{c_*} - 1\right]\left[1 - \Phi\left(\frac{c_* - u_*}{\sigma_{u_*}}\right)\right] \tag{2.44}$$

with

$$c_* \equiv \frac{\sigma}{28\, k \cos(\theta - \theta_{\rm w})}$$

for the case of $\cos(\theta - \theta_{\rm w}) > 0$ and $G = 0$ else. In expression (2.44) the probability function

$$\Phi(x) \equiv \frac{2}{\sqrt{2\pi}} \int_0^x {\rm e}^{-\frac{t^2}{2}} {\rm d}t \tag{2.45}$$

appears. The quantity σ_{u_*} is the standard deviation of the Gaussian distribution for the friction velocity, $\theta_{\rm w}$ is the wind direction. The parameters of the Snyder input are considered to be tuning parameters. In the wave-modelling applications discussed in this thesis,

$$\frac{\sigma_{u_*}}{u_*} = 0.4 \tag{2.46}$$

was chosen.

The Phillips input source function according to Cavaleri et al. (1981) was generalized to account for two effects. First, the filter of Tolman (1992) to avoid energy growth for frequencies less than the Pierson-Moskowitz frequency $f_{\rm PM}$ (Pierson et al. 1964) was included. Second, a new filter was added to gradually reduce input at increasing frequencies. This parametrizes the effect pointed out by Phillips (1977) that energy input by turbulent atmospheric pressure fluctuations to a wave spectrum occurs only for long waves with phase speeds c roughly obeying $u_{10}/c < 1.5$. With these two modifications, the Phillips input source function becomes

$$S_{\rm phil} = 2\,\frac{80\rho_{\rm a}^2}{g^2\rho_{\rm w}^2}\,\frac{c_{\rm g}}{\sigma}\,[u_* \cos(\theta - \theta_{\rm w})]^4 \underbrace{\exp[-\left(\frac{f}{f_{\rm PM}}\right)^{-4}]}_{\text{Tolman filter}} \underbrace{\exp[-\left(\frac{f}{f_{\rm PM}}\right)]}_{\text{new filter}}. \tag{2.47}$$

Here, $\rho_{\rm a}$ and $\rho_{\rm w}$ are the densities of air and water, respectively. The magnitude of Phillips input must be rescaled for small-scale applications. This has also been pointed out e.g. by Ris (1997). The exact magnitude of the process is thus considered as free tuning parameter in the wave model.

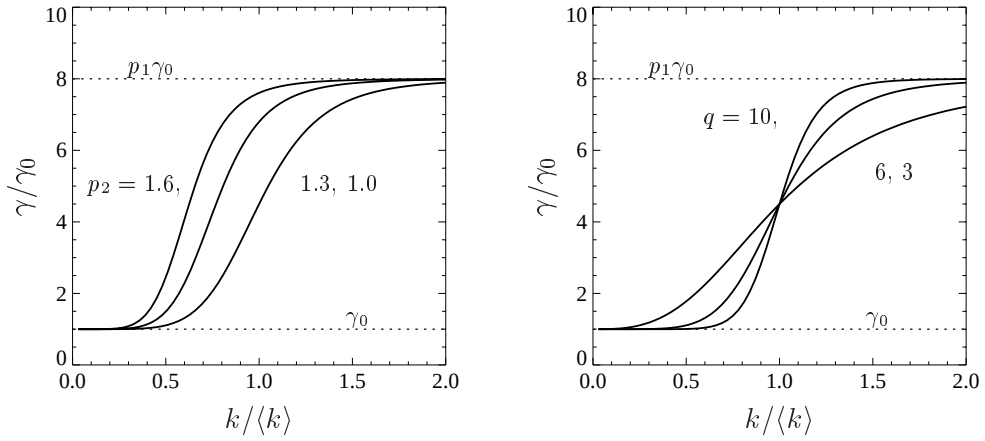

Figure 2.1: The influence of parameters p_1, p_2, and q on the dissipation coefficient $\gamma(N)$, equation (2.49). The plots show normalized quantities γ/γ_0 over $k/\langle k\rangle$. The parameters are $p_1 = 8$, in the left panel p_2 as indicated and $q = 6$, in the right panel $p_2 = 1$ and q as indicated. Dotted lines indicate extreme values of γ and their dependence on γ_0 and p_1.

Nonlinear Dissipation. Nonlinear Dissipation S_{dis} by wave turbulence interaction is considered in the wave model with a parametrization consistent to expression (2.37). It reads

$$S_{\mathrm{dis}} = -\gamma\, g\, k^5 \left(\coth 2kh + \frac{kh}{\sinh^2 kh}\right) N^2(\boldsymbol{k}). \tag{2.48}$$

The specific form of the factor $\gamma(\boldsymbol{k},\ldots)$ in (2.37) was obtained here from dimensional analysis and depth influence on particle motions in the wave flow field, cf. Rosenthal (1989). This led to the given wave-number and water-depth dependence of $\gamma(\boldsymbol{k},\ldots)$. The remaining free dissipation parameter γ in (2.48) is parametrized as functional of N to account for coupling effects, e.g. enhanced short-wave dissipation in the presence of long waves. This is modelled with a function of spectral mean wave number $\langle k\rangle$:

$$\gamma(N) = \gamma_0\, \frac{p_1 (p_2 \frac{k}{\langle k\rangle})^q + 1}{(p_2 \frac{k}{\langle k\rangle})^q + 1}. \tag{2.49}$$

Here, γ_0 gives the general magnitude of dissipation. The parameters p_1, p_2, and q control the relative magnitude of dissipation for different wave numbers within a wave spectrum. The shape of the function (2.49) is illustrated in figure 2.1. It is an increasing function of wave number from a low level of γ_0 to a maximum level of $p_1\gamma_0$. The horizontal offset of the increase relative to mean wave number $\langle k\rangle$ is given by p_2. The parameters p_2 and q influence the steepness. All parameters are considered as free tuning parameters. To study basic features of the wave model under neglect of coupling effects, γ can alternatively be treated as constant.

Dissipation by Bottom Interactions. Wave-energy dissipation by bottom interactions is treated in the wave model in standard form (2.32) as given in subsection 2.1.2. As first guess for the interaction parameter, $\Gamma = 0.038\mathrm{m}^2/\mathrm{s}^3$ is used. It is the value obtained by Hasselmann et al. (1973) from swell-decay analysis. Note, however, that Bouws et al. (1983) used a different value for application to depth-limited wind sea. They pointed out that Γ can be treated as free tuning parameter. This view is adopted in the present study.

Influence of Water Depths and Currents on the Source Terms. The source functions describe large-scale local perturbations of the wave spectrum which may depend on local water depth and current. The influence of water depth h as parametrized in the expressions of this subsection can be split into two classes:

1. Explicit dependence on h as given in S_{dis} and S_{bot}
2. Implicit dependence on h via frequencies, phase velocities, and group velocities following from the dispersion relation (2.12), as present in S_{in}, S_{phil}, S_{bot}.

Physical intuition suggests also a dependence of the processes on local currents. Currents change the relative velocities of waves and winds, thus influencing energy input from the atmosphere. They influence the bottom boundary layer and thus have impact on bottom interactions. Finally, they are expected to influence the general turbulence level in the wave field and thus take effect in dissipation by wave turbulence interaction. None of these effects are understood quantitatively, however. For this reason, the influence of local currents on the source functions is neglected in this thesis.

2.3.5 Numerical Treatment

Propagation and Refraction. The numerical scheme in the wave model for both propagation and refraction is an explicit first-order upwind scheme, similar to WAM cy. 4. A major drawback of this scheme in the context of global ocean wave modelling is its high level of numerical diffusion, see e.g. WAMDI (1988). This leads to considerable numerical dispersion in the case of swell propagation over large distances. For this reason, other schemes have been analysed in the context of ocean wave models, e.g. the ICN scheme of Tolman (1991), a second-order semi-implicit scheme (Lin et al. 1996a), and a third-order upwind scheme (Bender 1996). Obviously, the dispersion effect is less important in small-scale applications. Propagation plays another important role in fetch-limited situations, which are very likely to occur in small-scale, partially enclosed systems. Tolman (1992) showed that the impact of chosen propagation scheme on fetch-limited growth results of a wave model is much less important than the grid resolution. It is concluded here that with respect to accuracy, the first order upwind scheme is suitable for a small-scale coastal wave model.

The scheme is only conditionally stable, however. The stability criterion is the CFL criterion, which, in the case of combined propagation and refraction, takes the form

$$1 \;\geq\; \underbrace{|\dot{x_1}\frac{\Delta t}{\Delta x_1}| \,+\, |\dot{x_2}\frac{\Delta t}{\Delta x_2}|}_{\geq\; v_g \dfrac{\Delta t}{\Delta x}} + |\dot{k}\frac{\Delta t}{\Delta k}| \,+\, |\dot{\theta}\frac{\Delta t}{\Delta \theta}|. \tag{2.50}$$

Here, Δt is a time step equal for propagation and refraction discretized with grid increments Δx_1, Δx_2, Δk, $\Delta \theta$. The underbraced part can be approximated by the given expression if equal grid spacing is applied in both directions. This expression is used e.g. in WAM cy. 4 for stability checking, under neglect of the refraction contribution. In the presented wave model, the criterion is checked in its exact formulation (2.50).

The stability criterion can impose major obstacles in computation if highly variable topographies require small grid spacing or if depth or current-field gradients are large. It was pointed out above that a separate treatment of propagation, depth refraction, and current refraction is possible in the wave model. This enables an adaption of the three involved time steps to their individual stability requirements. In most applications, time-step splitting in this sense leads to a major saving of computing resources.

The stability problem is avoided in an instationary version of SWAN (Booij et al. 1998) by the use of an implicit first-order upwind scheme which is unconditionally stable. This scheme is computationally much more demanding, however, because a set of linear equations has to be solved iteratively at every time step. As discussed in the introduction of this thesis, the merits of unconditional stability are reduced also by the fact that accuracy requirements can impose a quantitatively similar restriction for the time steps as the stability criteria.

Source Term Integration. The numerical method for source-term integration is adopted from WAM cy. 4. It is a second-order semi-implicit scheme with approximations to facilitate computations (WAMDI 1988). In WAM, different time steps can be used for propagation and source-term integration, but the source time step must be smaller. This is not feasible when small grid resolutions needed for coastal application force down the propagation and refraction time steps for reasons of stability. For this reason, the source-term-integration time step of the wave model can be larger than the propagation and refraction time steps by choice of the user. The same has been suggested for an adaption of WAM cy. 4 to smaller scale applications (Luo et al. 1998).

2.3.6 Influence and Treatment of Instationary External Fields

It has been indicated in the subsections 2.3.3 and 2.3.4 how stationary water-depth and current fields can influence the wave-action balance. The consideration of such effects is state-of-the-art in third-generation ocean wave models. For wave modelling in coastal systems, a further class of interactions come into play. These are caused by tides and are related to time-varying water level and current fields. Different types of effects resulting from instationary external fields are discussed here. It is described how these are treated technically in the wave model.

Influence on the Action Balance. The choice of (k, θ) as independent variables in the action balance equation (2.38) avoids terms in the equation with partial time derivatives of the dispersion function. A term of this kind will be present if frequency is chosen as one variable. The partial time derivative of the dispersion function involves time derivatives of water level and current fields. These have to be taken into account for instationary modelling in full generality. Usually however, wave models use a quasi-stationary approximation. According to this, the external fields are treated as functions of time, but their partial time derivatives are neglected (cf. Tolman 1990). Since the question of partial time derivatives does not arise in case of a (k, θ) formulation, it is pointed out that this formulation is suitable for full instationary wave modelling which is possibly needed in tide-dominated areas.

Instationarity of external fields can be considered in the K-model by replacement of the

stationary fields in the action balance equation (2.38) by time functions. These can cause modulation of wave parameters by the following mechanisms:

1. Space-local effects, i.e. depending only on local values of the external fields:
   (a) Variation of current-induced Doppler shifts of integrated period parameters and energy-conserving shifts within the wave spectrum
   (b) Influences of water-depth variation on local wind input and dissipation.
2. Space-nonlocal effects:
   (a) Variation of shoaling and refraction
   (b) Variation of fetch due to up-fetch dry-falling areas
   (c) Variation of effective fetch through current-advected wave energy propagation.

Although some of the effects resulting from space- and time-varying external fields can be scaled and quantified individually, the net resultant of their complex interplay is hard to assess. It can be predicted for specific systems only by simulations carried out with a wave model. An application of this kind will be described in chapter 4.

Treatment in the Wave Model. Some technical aspects of the treatment of time-varying external fields in the wave model will be listed in this paragraph.

1. For a given area and time of investigation, a current model is applied to generate water level and depth-integrated current fields. The output is postprocessed to input fields for the wave model which can be provided with arbitrary time stepping. An interpolation routine similar to the wind field processing in WAM cy. 4 can be applied.
2. With each new field, the following precalculations must be repeated:
   (a) Computation of depth indices for table representations of depth-dependent quantities
   (b) Computation of gradients and dot terms
   (c) CFL check
   (d) Collection of temporarily dry grid points. A grid point is treated as dry whenever the depth is below 0.5 m. Wave energy is set to zero at dry grid points.
3. At selected output points and times, a transformation of the wave-action spectrum to $E(f, \theta)$ output spectra is performed. The frequency axis is fixed and can be chosen by the user. This enables a convenient analysis of spectral time series at a location. The transformation is energy-conserving, but energy beyond the chosen frequency interval is lost. In particular, in the case of opposing currents, energy located at frequencies close to the origin is abandoned to avoid division by zero or small numbers.

2.4 Summary

In this chapter the basic concepts of spectral wave modelling have been reviewed for the purpose of limiting scope, clarifying terminology, and introducing basic equations. The sea state is characterized by slowly varying wave spectra, whose dynamics are governed by the action balance equation. Spectral wave models solve this equation numerically.

The concept of nonlinear dissipation in spectral wave modelling has been introduced. A dissipation source function involving local powers of the wave spectrum is formally consistent with a general nonlinear shape. The source function is physically motivated and can thus be included in the sum of source functions of a spectral model.

A wave model using this source function has been described. It solves the action balance equation in wave number and direction coordinates and is thus suitable for applications to tidal systems. The model is the basic tool for further analysis presented in subsequent chapters of this thesis.

3 Wave Model Analysis and Validation

Spectral wave modelling with nonlinear dissipation will be analysed in this chapter by numerical experiments with a wave model. The dynamical equation of the model will be treated analytically in selected cases. An analysis of wave model performance in idealized "academic" test cases will enable comparison with observational evidence and existing wave models. Finally, the wave model will be tested in an application to a real geophysical system to perform validation against field data and comparison with other models.

3.1 Analysis of Model Equation

This section covers an analysis of the dynamical equation (2.38) used in the K-model. In special cases and in simplifying approximation, analytical treatment will be possible. It will be supplemented by simple numerical analyses. The purpose of this is to clarify principal features of the model and compare these with existing models of third and earlier generations.

3.1.1 Dynamical Equation in Reduced Dimensions

It is convenient for the present discussion to regard the wave-action spectrum $N(\boldsymbol{k}, \boldsymbol{x}, t)$ as function of discretized wave number $\boldsymbol{k}$. The dynamical equation for the wave-action spectrum (2.38) in the K-model can then be understood as a set of coupled partial differential equations for the space and time functions $N_{\boldsymbol{k}}(\boldsymbol{x}, t)$ of wave action in different spectral bins $\boldsymbol{k}$. Here, cases are considered in which the dynamical equation reduces to a set of ordinary differential equations, or algebraic equations. An example is stationary fetch-limited growth as will be defined in subsection 3.2.1. For reasons of symmetry, in this case the wave-action spectrum only depends on the space coordinate describing distance from shore (fetch), here denoted as x. Partial time derivative and longshore space derivative in equation (2.38) are zero. Refraction terms cancel because of spatial homogeneity. Thus, the set of partial differential equations is reduced to a set of ordinary differential equations

$$v_{\mathrm{g}} \partial_x N_{\boldsymbol{k}}(x) = a + b\, N_{\boldsymbol{k}}(x) + c\, N_{\boldsymbol{k}}^2(x)\,, \tag{3.1}$$

where v_{g} denotes the group velocity component in direction of x. Coefficients a, b, and c have been introduced to abbreviate parts of the source functions in which $\boldsymbol{k}$-local wave action $N_{\boldsymbol{k}}(x)$ does not appear explicitly. Detailed formulas can be obtained by comparison with the K-model source term expressions given in section 2.3. The coefficients are constant with respect to x but depend on $\boldsymbol{k}$. Coefficient c also depends on an integral of N over wave vectors. It causes a coupling of the equations (3.1).

Another example leading to a dynamical equation of similar form is duration-limited growth of the wave-action spectrum in a homogeneous system. For this case the wave-action spectrum will be a time function $N_{\boldsymbol{k}}(t)$. The corresponding dynamical equation can be obtained from (3.1) by the replacements $v_{\mathrm{g}} \partial_x \mapsto \partial_t$ and $x \mapsto t$. In the following subsections, solutions of (3.1) in different approximations will be discussed.

3.1.2 Equilibrium Range

Wind-sea wave spectra are characterized by one dominant peak at a thus defined peak wave number, or peak frequency in a frequency direction representation of the spectrum. The energy-containing part of the equilibrium range in a wave spectrum is given roughly by a subrange $1.5\,f_{\mathrm{m}} < f < 3\,f_{\mathrm{m}}$ of the corresponding energy spectrum $E(f)$ (Komen et al. 1994), where f_{m} is the peak frequency of the one-dimensional spectrum. The equilibrium range of wave spectra computed by the K-model can be given in analytical form. To enable comparison, theoretical and observational results are briefly reviewed from literature.

Review of Theoretical Studies and Observations. In theory and observations, equilibrium ranges are usually described with power law relations in frequency or wave number. Phillips (1958) proposed in a pioneering theoretical paper a universal saturation range of the form $E(f) = \alpha\, g^2 (2\pi)^{-4} f^{-5}$, involving the dimensionless "Phillips" parameter $\alpha = 0.0074$. In later papers by Kitaigorodskii et al. (1975), Thornton (1977), and Kitaigorodskii et al. (1983) power laws were given as function of wave number. The same was done by Phillips (1985), but in this expression the equilibrium range level is not universal but depends on wind speed. The wave number formulations of Phillips (1985) and Kitaigorodskii et al. (1983) can be transformed to power laws in frequency. These match the observational f^{-4}-results for the spectral tail in deep water of Toba (1973) and Donelan et al. (1985). A shallow-water equilibrium-range formulation for $E(f)$ spectra was given from the analysis of the TMA data as proportional to f^{-3} (Bouws et al. 1985).

K-model Equilibrium Range. Consider the action balance equation (2.38) as used in the K-model. For large k, the spectrum develops rapidly to a quasi-equilibrium, in which the local time derivative and the energy-conservative terms approach zero. The spectral form can thus be deduced from a balance of the source functions. It is given by equation (3.1), with the left-hand side set to zero. This results in a set of algebraic coupled equations for the wave action spectrum $N_{\boldsymbol{k}}$. In order to derive a closed formula for the equilibrium range from these equations, the individual source functions in the balance will now be analysed under the assumption of k being considerably larger than the peak wave number.

1. In a quasi-equilibrium state at high wave numbers, the Phillips wind input has only little influence on the wave-action level. This stems from the fact that the Phillips input is largest for waves with $u_{10}/c < 1.5$. It can thus be neglected in the present analysis.

2. It is assumed that the equilibrium range can be treated with the deep-water formulations of the source terms. This is no major restriction: influence of water depth scales with the inverse of the dimensionless product kh of wave number and water depth. The influence is thus rather small at wave numbers considerably larger than the peak wave number in most relevant cases. Therefore, bottom interactions and the shallow-water extension of nonlinear dissipation will be neglected.

3. The spectral coupling in the nonlinear dissipation source function leads to a reduction of dissipation for wave numbers around and smaller than the mean wave number, which is

close to the peak wave number, cf. figure 2.1. For large wave numbers, nonlinear dissipation as parametrized in the K-model is practically decoupled, on a level $\gamma = \gamma_0\, p_1$.

4. The modification of Snyder input to account for wind gustiness used in S_{in} of the K-model is effective only for waves in the vicinity of and smaller than $u_{10}/c \approx 1$. For waves in the equilibrium range this ratio is considerably larger than one. In the present analysis, a standard Snyder input, equation (2.31), can thus be considered as valid. In this source term, $\max((28u_* \cos\theta/c) - 1,\, 0) \approx 28u_* \cos\theta/c$ can be set for the same reason.

It is concluded from the preceding that the equilibrium range as computed by the K-model is given by a balance of standard Snyder input and decoupled nonlinear dissipation

$$0 = \beta_0\, \omega\, \frac{28u_*}{c} \cos\theta\, N_{\boldsymbol{k}} - \gamma\, g\, k^5\, N_{\boldsymbol{k}}^2. \tag{3.2}$$

Equation (3.2) is a set of decoupled algebraic equations leading, after transformation to energy spectra, to a law

$$F_{\boldsymbol{k}} \sim u_* \cos\theta\, g^{-1/2} k^{-7/2}, \tag{3.3}$$

with a dimensionless proportionality constant depending on the scaling of Snyder input and nonlinear dissipation. The expression is equivalent to the one given in Phillips (1985). In particular, the equilibrium range is not universal but depends on the friction velocity component $u_* \cos\theta$. This can lead to a fetch-dependent level of the high-frequency tail, if e.g. the drag coefficient c_{d} in u_* is described as wave-age dependent. As pointed out by Kitaigorodskii et al. (1975), the result in terms of wave number includes implicitly the influence of long waves, currents, and water depth on the equilibrium range of the corresponding one-dimensional frequency spectrum. In deep water without external influences it is given by an f^{-4} power law, consistent with the observational studies of Toba (1973) and Donelan et al. (1985).

A similar treatment of the equilibrium range in the K-model for the case of extremely shallow water does not lead to a simple power law formulation as proposed by Kitaigorodskii et al. (1975) and seen in observational data in Bouws et al. (1985). The influence of bottom interaction dissipation results in an additional term which can describe depth limitation of wave spectra. This is discussed, among other features, in the following subsection.

Equilibrium Range in Existing Wave Models. In contrast to the K-model formulation, existing wave models of all generations use prescribed, diagnostic spectral tails, usually given as power laws in frequency. These tails are insensitive to currents and water depths. The constraint of high-frequency tails to a fixed shape can lead to considerable changes in fetch-limited growth computations, cf. Banner et al. (1994). These authors have pointed out that the performance of third-generation models like WAM is influenced significantly by the artificial diagnostic spectral tail. The K-model conceptual idea is advantageous in this respect because a need for artificial prescriptions of spectral shape is not present — neither for physical nor computational reasons.

3.1.3 Solutions in Decoupled Approximation

In this subsection, solutions for the wave action spectrum are discussed which will be valid if the set of ordinary differential equations (3.1) is treated in decoupled approximation. The

approximation cannot be justified by physical argumentation. However, it enables the study of an analytical solution of (3.1). Although this solution will not be very realistic, basic features of the interplay of source functions in the K-model can be studied with it, which should also hold to some degree if the full coupled equations are treated in a numerical approach. The understanding gained by analysis of the decoupled, analytical solution can thus be used for systematic tuning of the full wave model.

The decoupling is performed by approximation of the wave-action-spectrum-dependent functional γ in the nonlinear dissipation source function S_{dis}, equation (2.48), by a dimensionless constant. In addition, for more clarity in the subsequent discussion, gustiness effects in the Snyder input are not considered, expression (2.31) will be used. Now, (3.1) can be interpreted as one ordinary differential equation in which a parameter $\boldsymbol{k}$ appears. Possible solutions of the equation will depend on this parameter and can thus be regarded as wave-action spectra in decoupled approximation. To study the solution classes of the equation, it is given here in a general shape as initial (boundary) value problem

$$\begin{aligned} \frac{\mathrm{d}}{\mathrm{d}x} y &= a + b\,y + c\,y^2 \qquad (x \geq x_0) \\ y(x_0) &= y_0 \end{aligned} \tag{3.4}$$

for a differentiable function $y : x \mapsto y(x)$. The coefficients a, b, and c are constant with respect to x and y. Depending on the initial value y_0 and signs of the coefficients, different general solutions exist for the problem. Here only the ones applying to the shape of the K-model source functions are discussed:

1. Coefficient c is negative because it describes wave-action dissipation
2. Coefficient a is positive because it describes Phillips energy input
3. Coefficient b consists of Snyder input and bottom-interaction dissipation. It is positive in deep water, and can have either sign or be zero in shallow water. In this case, it will be positive for large wave numbers and can turn negative for sufficiently small wind input at small wave numbers
4. The initial value y_0 is greater than or equal to zero since it describes wave action which is essentially nonnegative.

With these presumptions, the general solution of (3.4) can be given for $x \geq x_0$ as

$$y(x) = -\frac{s-b}{2c} - \frac{s}{c}\left(1 + \left[\frac{s}{c}\left(\frac{s-b}{2c} - y_0\right)^{-1} - 1\right] \mathrm{e}^{-s(x-x_0)}\right)^{-1}. \tag{3.5}$$

In the formula, an abbreviation $s = \sqrt{b^2 - ac}$ appears. A unique and stable stationary-state solution $y_{\mathrm{stat}} \equiv y|_{x=\infty}$ exists. It reads

$$y_{\mathrm{stat}} = \frac{-(b + \sqrt{b^2 - ac})}{2c}. \tag{3.6}$$

It can be verified that the given expressions are well defined and nonnegative. They are thus suitable for describing wave-action densities as functions of fetch or time. Some features of the solutions are highlighted here:

1. If y_0 is smaller than y_{stat}, y will grow in x asymptotically to y_{stat}
2. y will decay to y_{stat} if y_0 is larger than y_{stat}
3. For $b \leq 0$, the stationary-state solution will be small but still positive
4. The growth or decay rate is controlled by $s = \sqrt{b^2 - ac}$.

If the coefficients are identified with source term expressions in the K-model dynamical equation, some basic features of the model concept can be deduced from the solutions (3.5) and (3.6). Parameters of the processes represented by the source terms enter the coefficients in the following ways:

1. Phillips-input scaling α determines a
2. Snyder-input scaling β_0 enters b
3. Scaling of u_*/c in the Snyder input also influences b
4. Bottom-interaction-dissipation parameter Γ has a third impact on b
5. Nonlinear-dissipation parameter γ fixes c.

All coefficients a, b, and c depend on wave number $\boldsymbol{k}$. In principal, all listed model parameters are degrees of freedom in the solution to equation (3.4) and can be used for tuning the wave model. In the next paragraph, the influence of the parameters on the stationary-state solution will be discussed.

3.1.3.1 Stationary State Solution

Deep Water. In the context of problem (3.4), the term stationarity is used regardless of the specific interpretation of x as space or time variable. The stationary-state solution (3.6) describes fully developed wave spectra. If it is assumed that a is small compared to b and c, the relation $b^2 \gg ac$ will hold and (3.6) can be approximated to

$$y_{\mathrm{stat}} = -\frac{b}{c}\,. \tag{3.7}$$

This translates to an expression for the fully developed wave-action spectrum

$$N_{\mathrm{stat}}(\boldsymbol{k}) = \frac{\beta_0 \max(\frac{28\boldsymbol{u}_*\cdot\boldsymbol{k}}{\omega} - 1, 0)}{\gamma\, g\, k^5}\,. \tag{3.8}$$

The used approximation is indeed good, because a represents Phillips input which is neglectable in fully developed sea states, as was pointed out e.g. by Tolman (1992) and Snyder et al. (1992).

For an analysis of one-dimensional wave-energy spectra, the wave-action spectrum (3.8) can be transformed and integrated over directions analytically (Günther et al. 1995). The max function imposes a lower limit to wave numbers for which wave action can exist. The existence of a peak frequency for $E(f)$ follows from this. It was analytically obtained by Günther et al. (1995) as

$$f_{\mathrm{m}} = 0.22\frac{g}{28u_*}\,. \tag{3.9}$$

The numerical factor 28 can be seen as tuning parameter for the peak frequency of the fully developed wave-energy spectrum in deep water. The total energy in the spectrum depends on the ratio of Snyder-input magnitude β_0 and nonlinear-dissipation parameter γ. The stationary, one-dimensional energy spectrum resulting from equation (3.8) can be seen in panel (a) of figure 3.1, which will be discussed again in the context of instationary solutions. The stationary solution corresponds to the spectrum for largest fetch $\tilde{x} = 10^6$ shown in the figure. For comparison, the Pierson-Moskowitz (PM) spectrum (Pierson et al. 1964) for nondimensional peak frequency $\tilde{f} = 0.13$ is displayed in addition. Peak frequency and total energy of K-model spectrum and PM spectrum are equal. The spectral shapes are different. The K-model peak energy must be smaller, because the spectral tail is described by a f^{-4} power law instead of a f^{-5} tail as in the PM spectrum.

To calibrate the decoupled stationary solution in deep water, two of the five model parameters of the decoupled wave model have been fixed. In deep water, one degree of freedom remains undetermined: β_0 or γ can be chosen arbitrarily as long as the ratio of the two stays constant. This model parameter can be used to calibrate the fetch-limited or duration-limited growth rate of a selected wave parameter, as will be discussed below in the context of the instationary solution.

Shallow Water. In shallow water, the coefficient b in (3.4) contains bottom-interaction dissipation besides Snyder input. Since b can be negative in this case, the approximation $b^2 \gg ac$ no longer holds throughout the spectrum. It is still justified to approximate ac by zero, however, because the approximation will not affect total energy and peak frequency very much. The general stationary-state expression then becomes

$$y_{\mathrm{stat}} = \frac{-(b+|b|)}{2c} = \max\left(-\frac{b}{c}, 0\right). \tag{3.10}$$

The corresponding stationary shallow-water wave-action spectrum reads

$$N_{\mathrm{stat}}(\boldsymbol{k}) = \frac{\max\left(\beta_0 \max(\frac{28\boldsymbol{u}_*\cdot\boldsymbol{k}}{\omega} - 1, 0) - \Gamma k^2 \sigma^{-2}(1-\tanh^2 kh), 0\right)}{\gamma\, g\, k^5 (\coth 2kh + kh(\sinh^2 kh)^{-1})}. \tag{3.11}$$

This expression can be transformed and integrated numerically to yield expressions for fully developed wave-energy spectra and integrated wave parameters. Here, only the effect of depth limitation will be discussed.

For a suitable choice of environmental parameters friction velocity u_* and water depth h, the outer max function in the numerator of (3.11) will prohibit wave-energy growth for small wave numbers long before the deep-water peak wave number is reached. Spectral wave energy will be restricted to wave numbers higher than a depth limit k_{min}. The bottom dissipation not only imposes a depth limit on peak frequency, but also on total energy. Scaling of Γ can be chosen for correct depth limitation of either one of the two parameters, not for both. In panel (b) of figure 3.1, a series of depth-limited wave spectra for different nondimensional water depths $\delta = gh/u_{10}^2$ is shown. The spectra have been computed according to equation (3.11). The figure illustrates both the reduction of total energy and peak frequency with decreasing water depth.

A condition for the depth-limited minimum wave number of the stationary spectrum can be obtained by setting the numerator of expression (3.11) to zero. This gives an equation for the

minimum wave number $k_{\min}$. It can be solved analytically for the case of large wind speeds and low water depths, yielding

$$\tilde{k}_{\min} \sim \frac{\Gamma}{g\,\delta\,u_{10}} \tag{3.12}$$

for the dependence of nondimensional minimum wave number $\tilde{k}_{\min} \equiv k_{\min} u_{10}^2/g$ on nondimensional water depth δ and on wind speed u_{10}. The proportionality constant involved is dimensionless and only depends on the scaling of Snyder wind input. Since the bottom-interaction parameter Γ has a dimension $\mathrm{m}^2/\mathrm{s}^3$, the minimum wave number cannot be given as function of nondimensional depth δ alone: wind speed and gravitational acceleration also appear in (3.12). The formula can be used to obtain an upper limit of wave length in a shallow-water wind sea.

Stationary State in Existing Wave Models. The stationary state in the K-model follows from a balance of source functions, not from prescription of a limiting spectral shape as in first-generation models. In third-generation models, the existence of a fully developed spectrum depends on the chosen parametrization of white-capping dissipation and can be analysed only numerically (Komen et al. 1984). If nonlinear transfer is neglected, the K-model formulation is the only way of obtaining a reasonable stationary-state solution. The use of a quasilinear dissipation function depending otherwhise only on integrated spectral parameters will lead to a singular wave solution as described by Snyder et al. (1992).

3.1.3.2 Instationary Solution

The instationary solution (3.5) of the decoupled ordinary differential equation (3.4) describes the development of an initial wave-action spectrum at fetch x_0 to a fully developed, stationary spectrum at fetch ∞. One-dimendional energy spectra and integrated wave parameters can be computed from the general solution (3.5). The influence of wave-model parameters on the solution can be studied if the formal parameters a, b, and c are substituted by the corresponding source term expressions as given in section 2.3.

The growth rate of wave-action density at a given wave number $\boldsymbol{k}$ is characterized by $s = \sqrt{b^2 - ac}$, cf. equation (3.5). Growth of y from y_0 to y_{stat} is monotonous in x. The growth rate depends on wave vector. In cases for which $b^2 \gg ac$ holds, it is controlled exclusively by the parameter b. This means that the growth rate at a wave number is entirely influenced by Snyder input and bottom dissipation. Regarding the growth rate, the approximation of zero a is good in most cases. The parameter $a > 0$ is essential in (3.4), however. It enables a nonzero stationary-state solution in case of a zero initial value y_0.

Panel (a) of figure 3.1 displays a series of fetch-limited growing one-dimensional energy spectra. The motion of the spectral peak to lower frequencies with increasing fetch is demonstrated in the figure. This motion can be understood as follows:

1. The growth rate decreases with wave number, resulting in a faster rise of wave energy at higher frequencies.

2. The nonlinear dissipation also decreases with wave number, with a higher power in k than the input. For this reason, the stationary energy levels increase with decreasing frequency.

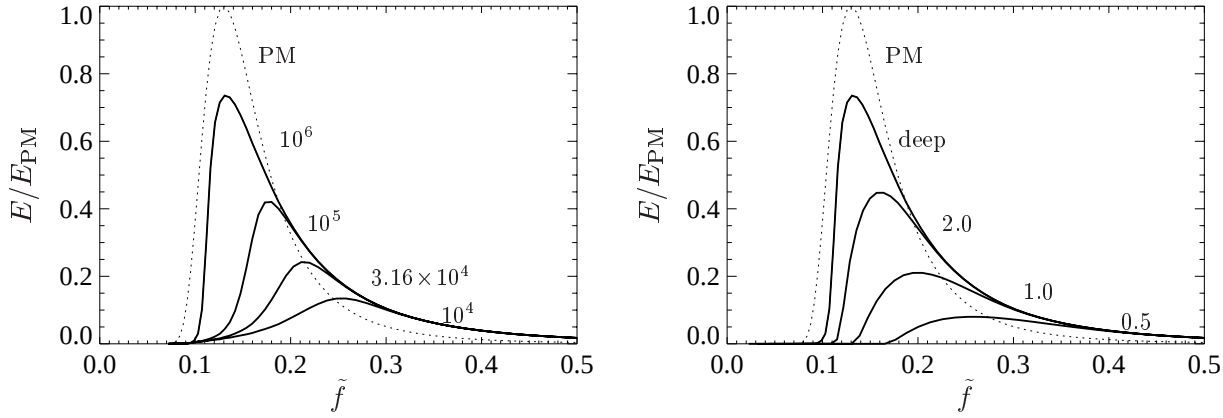

(a) Variation of fetch χ

(b) Variation of water depth δ

Figure 3.1: One-dimensional energy spectra in decoupled approximation as function of fetch and water depth. Quantities are nondimensional, units have been reduced with u_{10}. Energies have been normalized with the Pierson-Moskowitz peak energy. The dotted line is the Pierson-Moskowitz spectrum for a nondimensional peak frequency $\tilde{f} = 0.13$. Labeling numbers correspond to values of the varied parameter.

3. As a result, at low frequencies the stationary energy level is reached at later stages of development (larger fetches) and at higher levels.

The listed features explain a gradual peak motion to lower wave numbers in the course of spectral development. The same mechanism is present in first generation models, but it is caused there not by a dynamical balance of source functions, but by an artificial prescription of a limiting spectrum as parametrization of dissipation (e.g. Cavaleri et al. 1981). In contrast, the motion of the spectral peak in a developing wind sea has been primarily attributed to the influence of nonlinear energy transfer by Young et al. (1993).

In deep water, the motion of the peak, i.e. fetch dependence of peak frequency, can be adjusted by scaling of the Snyder input parameter β_0, since this parameter largely influences the growth rate. To ensure a correct total energy in the fully developed state, the magnitude of nonlinear dissipation must be chosen accordingly for a constant ratio of both parameters. Now all free model parameters of the decoupled model in deep water have been fixed. In particular, there is no means of tuning the fetch development of total energy. It is revealed that for fetch-limited growing wave spectra the energy content is too large in the decoupled solution. The same fact is expressed by an incorrect relation of nondimensional total energy ϵ to nondimensional peak frequency ν for growing spectra. The ϵ-ν relation is fixed in the decoupled solution. It cannot be influenced by any of the model parameters. For this reason, the decoupling approximation is unrealistic and not suitable for quantitative wave modelling applications.

Figure 3.1 also illustrates the above-stated monotonous fetch growth of wave energy at given frequency. Equivalent to this feature is the apparently missing overshoot of young spectral peaks over high-frequency tail energies of spectra at larger fetches.

The influence of the magnitude of a, containing the Phillips wind-input parameter α, on

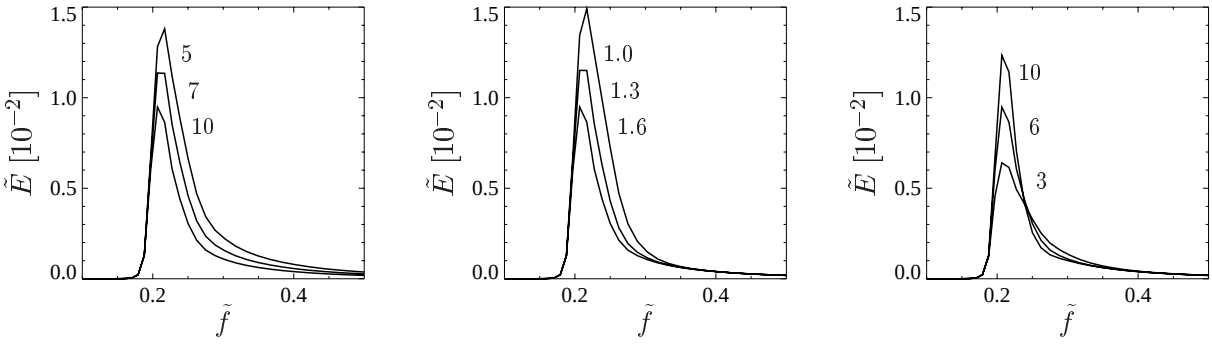

(a) Variation of parameter p_1 (b) Variation of parameter p_2 (c) Variation of parameter q

Figure 3.2: Influence of varying coupling parameters p_1, p_2, and q on a fetch-limited one-dimensional energy spectrum in deep water. The chosen fetch is $\tilde{x} = 8.5 \times 10^3$. Quantities are nondimensional, units have been reduced with u_{10}. Variations with respect to a calibration $p_1 = 10$, $p_2 = 1.6$, and $q = 6$ are shown. Labeling numbers correspond to values of the varied parameter.

peak frequency and total energy as computed from solution (3.5) was analysed. It is of minor importance for stationary solutions, as was mentioned above. However, the parameter α has an influence on the energy content of spectra at small fetches. It must be scaled carefully to avoid an overestimation of wave energy in these cases.

3.1.4 Influence of Coupling Parameters on the Spectral Shape

If the decoupling approximation which led to results presented in the preceding subsection is not applied, the dynamical equation (3.1) cannot be treated analytically. In this subsection, numerical solutions will be discussed which show the influence of the coupling parameters in the formulation of nonlinear dissipation, equation (2.48), on the spectral shape of one-dimensional energy spectra. The wave-action-spectrum-dependent dissipation parameter γ, equation (2.49), involves a magnitude γ_0 and three parameters p_1, p_2, and q. The influence of the parameters on γ has been illustrated in figure 2.1. Comparable variations of parameters as given in the figure will be used here to illustrate the influence of coupling parameters on a fetch-limited, deep-water, one-dimensional energy spectrum. The three panels of figure 3.2 are discussed to this end. Parameter p_1 controls the magnitude of dissipation enhancement for large wave numbers. For $p_1 = 1$ the decoupled approximation is obtained, increasing $p_1 > 1$ increases the degree of coupling in γ. Panel (a) shows that variation of p_1 changes spectral levels for frequencies equal to or larger than the peak frequency. Total energies change, whereas the peak frequency stays the same. It follows that p_1 can be used to tune the energy/peak-frequency ratio of the spectrum at a given fetch. Parameter p_2 basically shifts the curve γ along the wave number axis. It influences levels of the spectrum at the peak and frequencies higher than peak frequencies, but the energy content of the spectral tail does not change, see panel (b). Parameter q controls the slope of the dissipation enhancement with growing wave numbers. Panel (c) shows that rising q enhances the peak energy, but reduces the spectral level at higher frequencies. Energy levels at the tail are not influenced by q.

It is concluded that the parameters p_1, p_2, and q which determine the spectrum-dependent dissipation parameter γ can be used to adjust the spectral shape of fetch-limited growing wind sea. For given peak frequency, the level of the spectral tail, the level of the spectral peak, and the width of the spectral peak can be controlled. Note that the coupling parameters have been introduced to parametrize the physical effect of enhanced dissipation at wave numbers above the peak. The capability of controlling the spectral shape with the parameters is not merely "engineering", but it is a hint that observed spectral shapes may be considerably influenced by coupled dissipation effects, and not exclusively by internal nonlinear energy transfer.

Since the dissipation parameter γ in the K-model does not depend on wave directions in the given parametrization but only on wave vector moduli k, cf. equation (2.49), variation of the parameters cannot influence directional characteristics of wave spectra. It can be shown by numerical experiments that e.g. the directional spread parameter $s(f)$, cf. section 3.2, is not influenced by variation of p_1, p_2, and q.

3.1.5 Model Tuning Strategy

The one-dimensional analysis of the decoupled and coupled dynamical equations of the K-model in subsections 3.1.3 and 3.1.4 has resulted in a thorough insight into basic features of the dynamical behaviour of the model. The characteristic influence of different model parameters on wave spectra and integrated parameters has been clarified. This understanding can be used to formulate a tuning strategy of the model:

1. Peak frequency of fully developed spectra in deep water is tuned by scaling of u_* (variation of the numerical constant 28)

2. Total variance of fully developed spectra in deep water is tuned by fixing the ratio of Snyder input parameter β_0 and nonlinear dissipation parameter γ

3. The fetch development of peak frequency in deep water is fixed by scaling of β_0, which also fixes γ because of the condition in 2.

4. Coupling parameters in γ are fixed for correct fetch development of total variance and spectral shape parameters

5. The Phillips input constant α is rescaled to reduce its influence on young fetch-limited wind sea.

The various parameters do not influence the dynamics independently. For example, the total dissipation in a spectrum is influenced by γ_0 and also by the coupling parameters p_1, p_2, and q. For this reason, the process of tuning must be conducted in an iterative manner. The iteration has resulted in values of the various parameters as given in section 2.3. The quantitative performance of this tuning will be analysed in section 3.2.

3.2 Academic Tests and Comparison with Observational Knowledge

This section contains quantitative analyses of wave modelling with nonlinear dissipation. Applications of the K-model in so-called "academic" test cases will be described. Academic tests are wave simulations of idealized, simple systems which allow the isolation of principal features of the investigated model. Included in this section are fetch-limited growth, duration-limited growth, relaxation of swell, and response to turning winds.

3.2.1 Fetch-limited Growth

The idealized case of fetch-limited growth is characterized by a stationary and homogeneous wind field directed orthogonally offshore. In this situation wave spectra are a function of distance to the coastline only. The distance is called fetch. In most cases, fetch-limited growth is essentially in deep water because water depth increases with fetch-developing waves, resulting in $kh \gg 1$ throughout the analysed fetch range. The test case is very important, because fetch-limited wave development has been observed in a number of field studies which will be reviewed briefly in the next paragraph. Ocean wave models are usually tuned to fetch-limited growth observations. The test case has been applied as standard test in wave-model intercomparison studies and in publications on new ocean wave models. It allows a comparison of the K-model with other existing wave models and a comparison of K-model results with observations.

It is stressed that model behaviour in deep-water fetch-limited growth is important even for models which are designed for small-scale shallow-water applications. Any wave growth is initiated in deep water. If a shallow-water wave model fails to describe the waves correctly in the initial stage, it cannot be expected to perform well in the gradual transition to shallow water and finally depth limitation.

3.2.1.1 Review of Observations and Model Intercomparison Studies

Observational studies on fetch-limited growth resulted in empirical laws describing wave development in a quantitative manner. These results are briefly reviewed here to provide criteria upon which the K-model can be assessed and validated in comparison with other models.

Growth Curves and One-dimensional Spectra. The Kitaigorodskii similarity law (Kitaigorodskii 1962) has been commonly used to describe growth laws for nondimensional wave parameters as function of nondimensional fetch. The parameters can be nondimensionalized with respect to wind speed in 10 m height u_{10} or friction velocity u_*:
dimensionless fetch

$$\chi \equiv \frac{g\,x}{u_{10}^2}, \quad \chi_* \equiv \frac{g\,x}{u_*^2}, \tag{3.13}$$

dimensionless energy

$$\epsilon \equiv \frac{g^2 E}{u_{10}^4}, \quad \epsilon_* \equiv \frac{g^2 E}{u_*^4}, \tag{3.14}$$

dimensionless peak frequency

$$\nu \equiv \frac{f_{\mathrm{m}}\, u_{10}}{g}, \quad \nu_* \equiv \frac{f_{\mathrm{m}}\, u_*}{g}. \tag{3.15}$$

In the same manner, quantities time, frequency, and one-dimensional energy spectrum can be nondimensionalized, e.g. using u_{10}:

$$\tau \equiv \frac{g\, t}{u_{10}}, \quad \tilde{f} \equiv \frac{f\, u_{10}}{g}, \quad \tilde{E}(f) \equiv \frac{E(f) g^3}{u_{10}^5}. \tag{3.16}$$

Friction velocity u_* has been introduced in subsection 2.1.2. Further notation is x for fetch, E for total energy, and f_{m} for peak frequency of the one-dimensional spectrum $E(f)$, cf. appendix A.1. Although u_* scaling is favored today over scaling with u_{10} (Janssen et al. 1987), observational results can be given more accurately using u_{10}. This quantity is usually measured. Transformation to u_* introduces uncertainties about the drag coefficient c_{d}. It is commonly used in a wind-dependent parametrization by Wu (1982), e.g. in Kahma et al. (1992) and Van Vledder et al. (1993).

Important observational studies dealing with fetch-limited development of one-dimensional spectra and integrated wave parameters in deep water were the JONSWAP experiment (Hasselmann et al. 1973), and experiments by Toba (1973), Kahma (1981), Donelan et al. (1985), and Donelan et al. (1992).

The JONSWAP results suggested a self-similar spectral form for growing one-dimensional wave spectra. It was parametrized using the parameters peak frequency f_{m}, Phillips constant α, overshoot parameter γ, and peak-width parameter σ, henceforth called JONSWAP parameters. The JONSWAP spectrum is given in appendix A.1. As pointed out in section 3.1, it has a f^{-5} spectral tail. Fixed fetch relations for peak frequency and Phillips parameter were found, whereas for the rest of the JONSWAP parameters no fetch dependence was observed. A fetch relation for total energy followed from integration of the JONSWAP spectra. The JONSWAP parameters are statistically correlated. Fixed parameter relations for fetch-limited growing spectra in JONSWAP were summarized by Hasselmann et al. (1976), referred to as HRMS in what follows. Relations important for comparison with K-model results are cited here from HRMS.

Total energy - fetch (ϵ-χ) relation:

$$\epsilon = 1.6 \times 10^{-7}\, \chi\,, \tag{3.17}$$

peak frequency - fetch (ν-χ) relation:

$$\nu = 2.84\, \chi^{-0.3}\,, \tag{3.18}$$

Phillips parameter - fetch (α-χ) relation:

$$\alpha = 0.0662\, \chi^{-0.2}\,, \tag{3.19}$$

total energy - peak frequency (ϵ-ν) relation:

$$\epsilon = 5.3 \times 10^{-6}\, \nu^{-10/3}\,. \tag{3.20}$$

In addition to checking these relations, the rest of the JONSWAP parameters can be determined from fit to model spectra in order to compare spectral shapes with empirical evidence from the JONSWAP experiment.

Toba (1973) and following observational studies all pointed out a f^{-4} dependence of the spectral tail. A reanalysis by Battjes et al. (1987) showed consistency with a f^{-4} tail also for the JONSWAP data set. An important reanalysis study by Kahma et al. (1992), henceforth referred to as Kahma, addressed discrepancies in observed growth laws in the JONSWAP, Kahma (1981), and Donelan (1985) data sets. Part of the discrepancies were attributed to effects of atmospheric stratification and could be decreased. The Kahma reanalysis resulted in new growth laws which are widely used today for tuning of wave models, e.g. in Tolman (1996). The laws were given both for u_* and u_{10} nondimensionalisation. The K-model growth curves will be compared both with the Kahma laws and the original JONSWAP laws.

Fetch-limited wave growth terminates at a stage of full development, given by the Pierson-Moskowitz spectrum (Donelan et al. 1992). This spectral form was deduced from an analysis of open-ocean stationary wave spectra by Pierson et al. (1964). The spectral form is illustrated in appendix A.1 in connection with the JONSWAP spectrum. The fetch-limited growth data sets cited above do not include information on the transition of wave growth from large fetches to full development and the length scale associated with it. This was achieved in an observational study using remote sensing techniques by Walsh et al. (1989). One result indicated the existence of a fully developed sea state, and agreement of the total energy growth curve with the original JONSWAP law according to HRMS, delimited by the Pierson-Moskowitz level. Yet another study of fetch-limited wave growth by Donelan et al. (1992) covered a different physical length scale than in Walsh et al. (1989), but wave development was also observed up to full development. The result was a smoother transition to full development. An important remark in the conclusions of Donelan et al. (1992) questioned the existence of a universal power law for fetch-limited growth. Such a conclusion imposes difficulties for wave-model tuning, because no general evidence can be assumed to compare with. The conclusion supports the idea that wave models must be tuned for each individual application to reach maximum accuracy.

Directional Spread. Directional distributions of measured fetch-limited growing wave spectra in deep water have been studied e.g. by Mitsuyasu et al. (1975), Hasselmann et al. (1980), Holthuijsen (1983), and Donelan et al. (1985). Mitsuyasu et al. (1975) gave a parametrical form of the directional distribution which depends on a frequency-dependent spread parameter $s(f)$. It is given in appendix A.1. The studies of Hasselmann et al. (1980) and Holthuijsen (1983) both supported this form of the spreading function. Donelan et al. (1985) suggested a new parametrical form. The results of Donelan et al. (1985) differ from Mitsuyasu and Hasselmann. Donelan et al. observed a significantly narrower directional spread. The Donelan results were obtained with a higher resolution, they are commonly accepted today for the case of deep water (Young 1994, Young et al. 1996c).

Observations in Shallow Water. In contrast to deep-water fetch-limited growth, only few experimental data sets of shallow-water fetch-limited growth can be found in the literature. This corresponds to the above mentioned fact that in most cases fetch-limited growth is essentially

in deep water. An analysis of shallow-water wave spectra was performed by Bouws et al. (1985, 1987). The analysed TMA data did not exclusively consist of purely fetch-limited wave spectra. The study resulted in an extension of the JONSWAP deep-water self-similar spectral shape to shallow water. The corresponding parametrical spectral shape is called TMA spectrum. A correlation of total energy ϵ with nondimensional spectral peak wave number κ as growth parameter was found in which an explicit depth dependence was not apparent. In contrast to the deep-water JONSWAP analysis, no statistical relations between spectral parameters and fetch could be found in the TMA data set. One reason was an insufficient amount of available fetch-limited wave data.

An analysis of shallow-water fetch-limited growth data was published by Young et al. (1996a, 1996b, 1996c). This data set is the only one consisting exclusively of fetch-limited growing wave spectra in shallow water. As a result of the analysis, the authors gave growth curves for total energy and peak frequency for various nondimensional water depths $\delta = gh/u_{10}^2$. Principal features of these are essential deep-water behaviour quantitatively corresponding to growth laws of HRMS or Kahma for small fetches, and depth limitation for large fetches. K-model growth curves in shallow water will be compared with the Young et al. observational results. Further results of Young et al. concerned spectral evolution and directional spread in shallow-water fetch-limited growth. According to these, the one-dimensional spectra are well described by the TMA spectral shape, and as in the analysis of Bouws et al. (1987), a correlation of ϵ and κ was found in the data. Directional distributions are broader than the ones measured by Donelan et al. (1985) for deep water.

In a recent study, Young (1997) applied a differential analysis first used by Donelan et al. (1992) to the data set of Young et al. (1996a). As for deep water (Donelan et al. 1992), the existence of one nondimensional growth curve is called into question. Consideration of varying water depths and wind speeds along fetch resulted in the explanation of anomalous features in Young et al. (1996a). As pointed out above, this result imposes difficulties for wave-model tuning.

Wave Model Intercomparison Studies. The test case of fetch-limited growth was used in the SWAMP intercomparison study of ocean wave models (SWAMP 1985) and in the SWIM intercomparison study of shallow-water operational wave models (SWIM 1985). The SWAMP study revealed qualitative differences between first- and second-generation models for deep-water fetch-limited growth. The SWIM study showed qualitative differences of the three investigated models concerning depth limitation. K-model results will be related to these findings.

3.2.1.2 K-model Results

Since fetch-limited wave growth is a one-dimensional problem, cf. section 3.1, the K-model fetch-limited-growth results presented here were obtained by one-dimensional integration of the dynamical equation. The model was set up on a one-point grid. The time variable was transformed to fetch by division with group velocities. In this way, very high-resolution model computations were achieved. A fetch increment of 30 m ensured model results to be independent of the discretization. This was checked numerically. The model results thus give an accurate picture of the source function interplay. They are not influenced by numerical problems arising

from the propagation algorithm, as is the case in full three-dimensional applications (Tolman 1992). In particular, development from a zero-energy boundary does not impose a considerable error any more.

For convenience in the presentation of figures, fetch-limited growth results of the K-model are discussed in the following for deep and shallow water in a parallel manner. For the fetch-limited growth analysis of the K-model, the following values for the model parameters were used:

1. Nonlinear dissipation: $\gamma_0 = 0.09485$, $p_1 = 10$, $p_2 = 1.6$, and $q = 6$
2. Snyder input: $\beta = 0.0009$
3. Phillips input: rescaled by a factor 0.1 with respect to (2.47)
4. Bottom dissipation: $\Gamma = 0.038\,\mathrm{m}^2/\mathrm{s}^3$.

Aspects of this choice will be discussed subsequently in connection with the results. For all fetch-limited growth computations, a wind speed of $u_{10} = 10$ m/s was prescribed.

Growth Curves. In figure 3.3, growth curves for nondimensional energy and peak frequency as computed by the K-model are displayed. Panel (a) of the figure illustrates the ϵ-χ relation:

1. The panel shows the group of growth curves for various water depths and deep water as thick lines. The additional thin line is a result according to a tuning as used in the North-Sea-storm hindcast described in section 3.3. Empirical laws according to Kahma and HRMS are given as dashed, dotted, and dash-dotted lines. They are delimited by the Pierson-Moskowitz energy level.

2. The K-model growth curve computed with the North-Sea tuning is consistent with the Kahma empirical law for stable atmospheric stratification in the case of small fetches. It reaches the Pierson-Moskowitz level at large fetches. The growth curve according to the model tuning as given in this subsection is consistent with the HRMS empirical law for small fetches, which has less energy content. The curve fails to reach the Pierson-Moskowitz level at full development. The model tuning for agreement with HRMS has been chosen for the small-scale applications given in chapter 4. For relevant cases, nondimensional fetch will be well below $\chi = 10^4$ in these applications. This will be shown in chapter 4.

   The qualitative shape of both deep-water growth curves differs from the power-law formulation of the empirical laws: power-law formulations appear as straight lines, whereas the K-model growth curves are curved for any fetch, describing a smooth transition to full development from the very start at initial fetches. This feature is also observed in third-generation ocean wave models, as was pointed out by Banner et al. (1994).

3. The group of growth curves for various nondimensional water depths δ demonstrates depth limitation of total energy in the K-model. The shape of the curves in transition to depth limitation is consistent with observations of Young et al. (1996a). The depth limits of

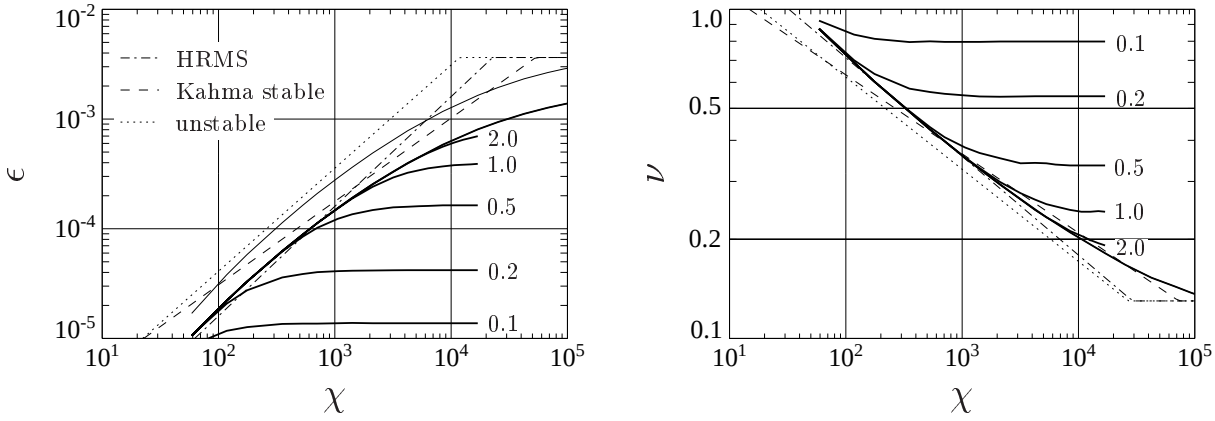

(a) Total energy ϵ vs. fetch χ

(b) Peak frequency ν vs. fetch χ

Figure 3.3: Growth curves for ϵ and ν as function of χ for various δ, as labelled by numbers. Dotted, dashed, and dash-dotted lines are empirical relations according to Kahma for unstable and stable atmospheric stratification, and according to HRMS. The thin line in panel (a) is a K-model growth curve computed according to the model calibration for the North Sea hindcast, cf. section 3.3.

energy as computed by the K-model are considerably lower than the observed limits, however. This can be checked by comparison with figure 12 in Young et al. (1996a). But comparison of quantitative depth limitation with the Young et al. empirical law is misleading, since this law is given exclusively with nondimensional quantities. Depth limitation in the K-model depends on wind speed, however, as was pointed out in section 3.1 of this thesis. This was confirmed by a numerical experiment using double wind speed ($u_{10} = 20$m/s). In this case, depth limitation as computed by the K-model was less severe.

Panel (b) of figure 3.3 illustrates the ν-χ relations as computed by the K-model:

1. This panel shows growth curves for nondimensional peak frequency, with information content and labeling according to panel (a). Only the tuning version as given in this subsection is discussed here, however.

2. The deep-water growth curve for peak frequency as computed by the K-model matches the HRMS results for small fetches, and the Kahma stable-stratification results for large fetches. The curve approaches the Pierson-Moskowitz peak frequency at large fetches. A rescaling of Snyder input to the above given value of $\beta = 0.0009$ from originally $\beta = 0.0003$ was needed to obtain sufficiently fast development of peak frequency. As pointed out in section 3.1, motion of peak frequency in the K-model results depends largely on the scaling of wind input.

   As in the case of the total energy growth curve, the shape of the peak frequency growth curve as computed by the K-model does not obey a power law.

3. The depth limitation of K-model peak frequencies is illustrated by the group of curves for various nondimensional water depths δ. Again, the depth limitation is revealed as depending on wind speed in the K-model, cf. the discussion for total energy.

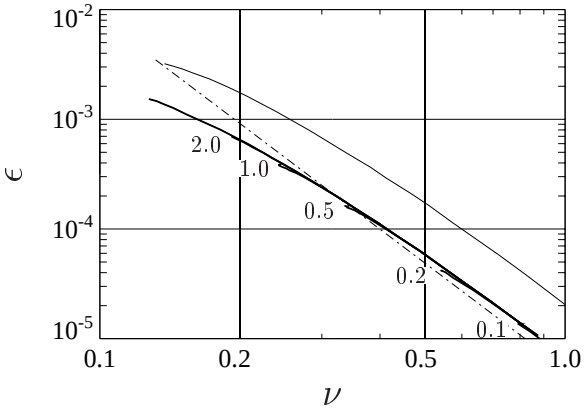

Figure 3.4: K-model ϵ-ν relations. Annotation as in figure 3.3

Finally, in figure 3.3 K-model ϵ-ν relations are displayed:

1. The content of this figure corresponds to panel (a) of figure 3.3. Only one empirical law (HRMS) is given, because the Kahma curves are very close to it. Information in this figure can, of course, be inferred from the preceding one.

2. Since peak frequency roughly matches HRMS throughout the given fetch range and total energy is low at large fetches, the ϵ-ν curve matches HRMS for low ϵ, but is too low for large.

3. The K-model ϵ-ν relation does not depend on water depth. This is in contrast to the TMA-data-analysis result by Bouws et al. (1983) showing no depth dependence in ϵ-κ relations.

4. The ϵ-ν relation for the North-Sea calibration of the K-model (thin line) matches HRMS only for fully developed sea states. It is parallel to the curve corresponding to the tuning presented in this section. The analysis reveals that the slope of ϵ-ν relations in the K-model does not agree with observational evidence. The slope can obviously not be influenced by calibration of free K-model parameters. For this reason, the relation can be correct only for a limited fetch range, e.g. for fetches $\chi < 10^4$ as shown here. It can be anticipated that this shortcoming has to do with the neglect of nonlinear transfer of energy in the model formulation.

In the following, K-model growth-curve results will be related to results of existing wave models. The K-model deep-water fetch-limited growth curves for total energy and peak frequency shown in figure 3.3 lie inside the bulk of modelled curves of the SWAMP (1985) study. In the SWAMP study, scatter in fetch-limited growth of total energy as modelled by various operational wave models was removed by rescaling the drag coefficients to achieve agreement of model results with the HRMS empirical law. After rescaling, the two first-generation models of the SWAMP study, i.e. MRI and VENICE, failed to reach the Piersion-Moskowitz energy for full development, cf. figure 7.8 in SWAMP (1985). This behaviour is in one aspect similar to the K-model: after tuning to HRMS for smaller fetches, the fully developed energy content is low.

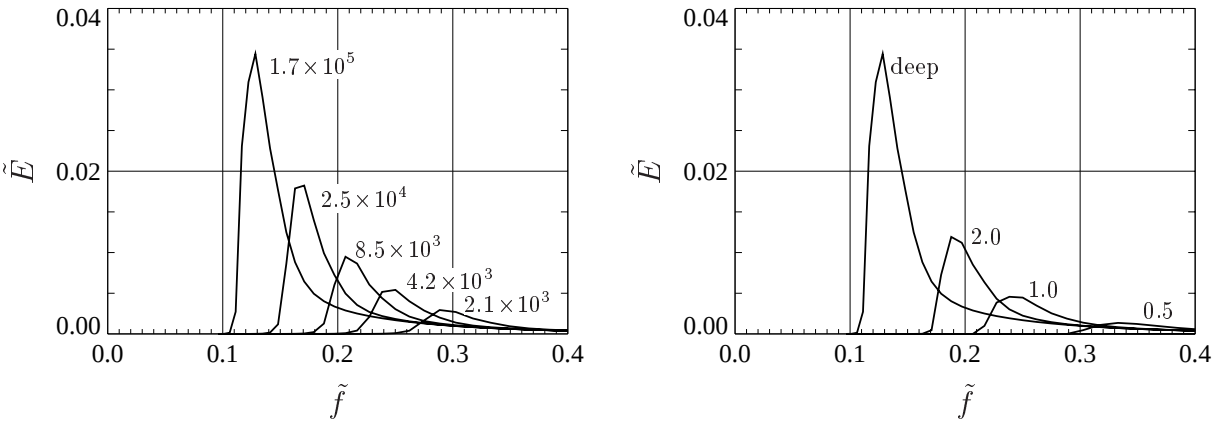

(a) Varying nondimensional fetch χ

(b) Varying nondimensional water depth δ

Figure 3.5: One-dimensional energy spectra. Labeling numbers indicate values of nondimensional fetch χ (panel a) and water depth δ (panel b).

The behaviour of peak frequency of the VENICE model after rescaling is different to the K-model. The K-model reproduces empirical laws. VENICE fails to reach the Pierson-Moskowitz peak frequency, and the slope of the curve is too low, resulting in too low peak frequencies at small fetches. This means that the ϵ-ν relation of VENICE is incorrect throughout the modelled fetch range, whereas it is correct in the K-model for fetches $\chi < 10^4$.

A similarity to VENICE is the scaling of Snyder input: VENICE uses $\beta \approx 0.001$. Large inputs are needed in both models since nonlinear interactions are neglected which support the motion of peak frequency to lower values with increasing fetch. Further qualitative comparisons with SWAMP results will be given below in the discussion of duration-limited growth.

The shallow-water growth curves of the K-model can be compared with the results of the SWIM study regarding depth limitation. K-model depth limitation of total energy and peak frequency is qualitatively similar to the results of the BMO and GONO models, which both use a bottom-dissipation source function. Qualitatively different are the HYPAS results. This model has implicit depth-dependent dissipation via the TMA spectral shape. For a quantitative comparison with BMO and GONO, results for model runs with equal wind speeds must be compared, since depth limitation in the K-model is wind dependent. It should be wind dependent also in GONO, since it similarly uses a constant dimensional bottom-interaction-dissipation coefficient Γ. Quantitative agreement of K-model, BMO, and GONO with respect to depth limitation of total energy and peak frequency for the first test case in SWIM was shown in Schneggenburger et al. (1997).

One-dimensional Spectra. Figure 3.5 displays one-dimensional fetch-limited energy spectra as computed by the K-model. Panel (a) contains deep-water spectra for various fetches. The spectra are labelled with the corresponding values for χ. Besides the development of total energy and peak frequency which was given quantitatively by growth curves in the last paragraph, the figure illustrates an overshoot of developing spectra in the K-model. The overshoot results from the spectral coupling in nonlinear dissipation. In one-dimensional spectra in decoupled

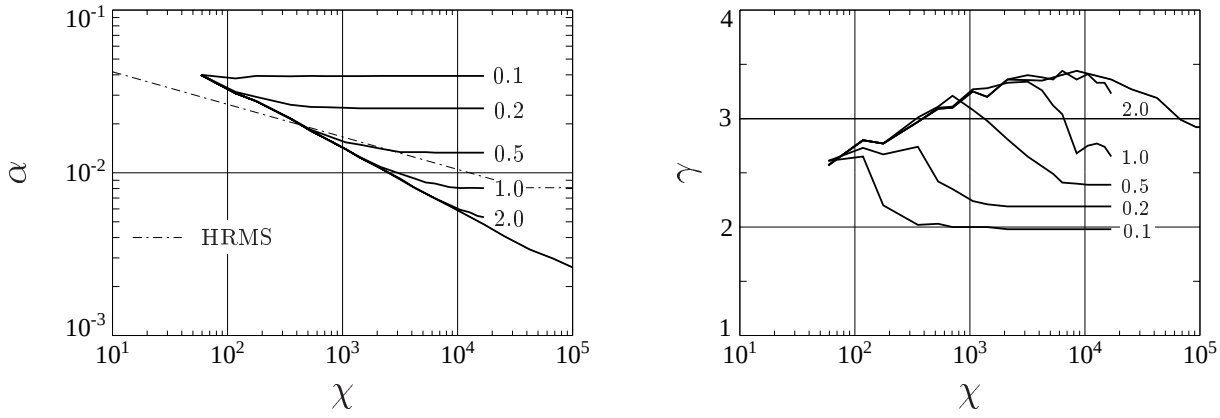

(a) Parameter α vs. fetch χ

(b) Overshoot parameter γ vs. fetch χ

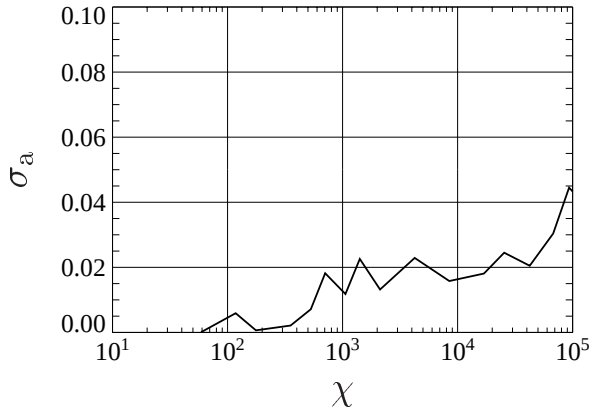

(c) Forward-face peak width σ_a vs. fetch χ

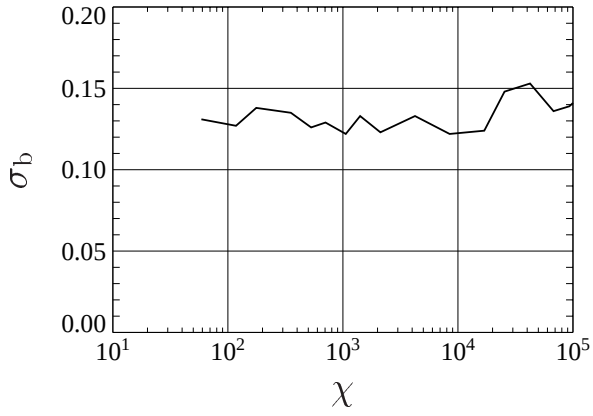

(d) Rear-face peak width σ_b vs. fetch χ

Figure 3.6: Growth curves for the JONSWAP shape parameters as function of nondimensional fetch. Labeling numbers in panel (a) and (b) indicate values of nondimensional water depth δ. The dash-dot line in panel (a) is the corresponding relation according to HRMS.

approximation the overshoot was not present, cf. figure 3.1 of section 3.1. Panel (b) illustrates one-dimensional shallow-water spectra for various nondimensional depths δ at a fetch of $\chi = 1.7\times10^5$. Depth limitation of total energy and peak frequency is clearly visible.

The spectral shape of the K-model one-dimensional energy spectra can be compared with the JONSWAP self-similar spectral shape by fitting a JONSWAP spectrum to the K-model spectra and comparing the resulting JONSWAP parameters with the fetch relations for the parameters as given in Hasselmann et al. (1973) and HRMS. The fit was carried out with the method according to Müller (1976). Figure 3.6 displays the fetch development of JONSWAP parameters α, γ, σ_a, and σ_b. For α and γ, curves for various nondimensional water depths δ are given.

1. The K-model α is fetch dependent according to the used fit, because in the method of Müller α is determined from data within the frequency range $1.35f_m \leq f \leq 2f_m$. The

level of spectral tail, however, is constant with fetch in the K-model. But to be able to compare with observed spectra, the same fit algorithm must be applied. According to this algorithm, the K-model α parameters are indeed fetch dependent. In panel (a) it is apparent that the slope of the α-χ curve differs from the HRMS empirical law. The order of magnitude of the K-model results generally agrees with the JONSWAP data, however. Parameter α is depth limited, corresponding to the depth limitation of total energy.

2. The overshoot parameter γ has values around 3, which agrees with JONSWAP results. With decreasing water depth, γ also decreases. This is qualitatively different to measured shallow-water results of Young et al. (1996b).

3. The mean JONSWAP results for the σ parameters were $\sigma_\mathrm{a} = 0.07$ and $\sigma_\mathrm{b} = 0.09$, data were scattered by an order of magnitude. The K-model values are within the same order of magnitude, but the forward-face width is smaller and the rear-face width is larger than the JONSWAP mean values. The overall width of spectral peak corresponds to the JONSWAP result, however. The σ parameters are not depth dependent in the K-model results. Therefore, results for shallow water are not shown.

It was shown in section 3.1 that the shape of one-dimensional energy spectra as computed by the K-model can be controlled with the coupling parameters of nonlinear dissipation. The agreement of spectral shape parameters computed by the K-model with the JONSWAP values as shown here results from tuning of the coupling parameters. It is shown by this that self similarity of fetch-limited growing wind sea can be caused by coupled dissipation instead of exclusively by the influence of nonlinear energy transfer.

Directional Spread. An analysis of directional spread of wave spectra completes the discussion of K-model fetch-limited-growth results. Directional spread is quantified here by the frequency-dependent directional spread parameter $s(f)$ of the Mitsuyasu parametrical distribution defined in appendix A.1. It was determined from the first directional Fourier coefficients of two-dimensional energy spectra according to equations (A.7) and (A.9).

Figure 3.7 illustrates K-model directional spread in deep water for two fetches, and for two water depths at given fetch. The figure contains empirical laws from observational results by Mitsuyasu et al. (1975), Donelan et al. (1985), and Young et al. (1996c).

1. Since dissipation in the K-model is isotropic, the directional spread of computed wave spectra follows entirely from the directional characteristics of wind input. The asymptotic value of $s|_{f \gg f_\mathrm{m}} \approx 4$ appearing in all curves is determined by Snyder input. For large frequencies, it behaves roughly as $\max(\cos\theta, 0)$, with cutoffs induced by directional discretization. This distribution is best fit by a value around 4 for the parameter s. The asymptotic value $s|_{f \ll f_\mathrm{m}} \approx 10$ of the curves can be explained with similar arguments by the $\cos^4$ directional dependence of Phillips input, which supplies residual energies at small frequencies.

2. In panel (a), peak values of s are large and increase with approach to full development. This is explained by the fact that Snyder input to the spectra is possible only where

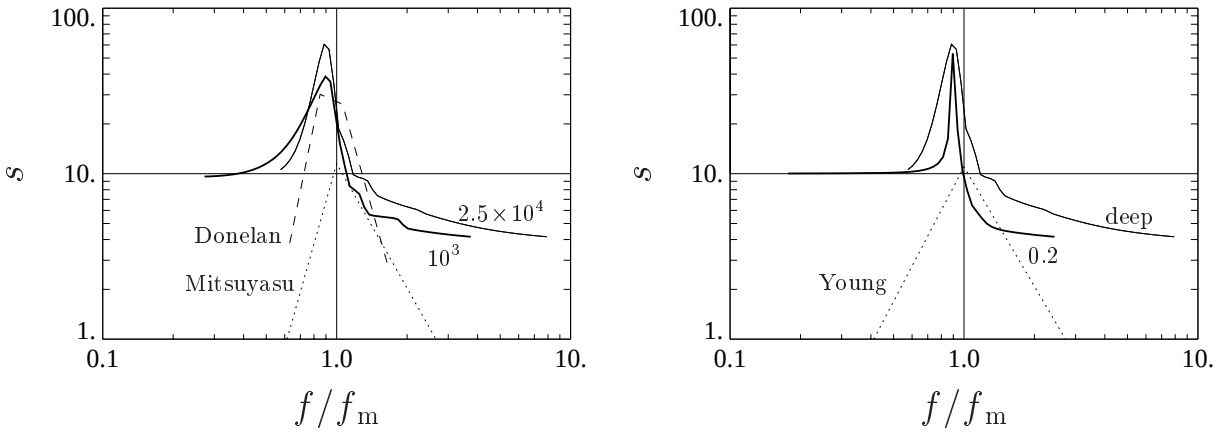

(a) Deep water, varying fetches χ

(b) Fetch $\chi = 2.5\times10^4$, varying water depths δ

Figure 3.7: Directional spread parameters vs. frequency in units of peak frequency. Curves are labelled with corresponding values for χ and δ, respectively. Observational results of Mitsuyasu and Donelan for deep water are given in panel (a), of Young for shallow water in panel (b).

the forcing wind speed is larger than the wave speed, a region which is gradually confined to directions in the spectrum matching the wind direction. Very narrow directional distributions at the fully developed peak result from this.

3. The deep-water directional-spread parameters of the K-model are much larger than the Mitsuyasu empirical law suggests. The K-model results correspond better to the Donelan results, which have been digitized from figure 29 of Donelan et al. (1985). Their data for an inverse-wave-age range of $U_c/c_p = 1$ to 2 are displayed here. The K-model spread curve for $\chi = 2.5\times10^4$ falls in this range, the curve for $\chi = 10^3$ is slightly outside (corresponding U_c/c_p values are 1.05 and 2.22). At the spectral peak, the K-model results for deep water are narrower than the Donelan et al. (1985) results, but qualitatively agree with these regarding a wave-age dependence of directional spread.

4. Panel (b) shows that K-model spectra are broader in shallow water. This agrees with qualitative results of Young et al. (1996c). The K-model results are within the order of magnitude of the measured data except for a severe narrowing at the spectral peak. Results are within the scatter of measured data for $f/f_m = 0.9$ to 2, cf. figure 5 (a) in Young et al. (1996c). The narrowing at the peak can be explained by the influence of bottom-interaction dissipation in the model. Near the spectral peak in a depth-limited sea, spectral energy content will be confined to directions close to the wind direction. Forcing of waves in other directions will be depth-limited since bottom friction counterbalances the relatively weaker input to these directions. This leads to a narrow spreading similar to the case of fully developed spectra in deep water.

The K-model deep-water results for the spread parameter can be compared with results of WAM given in figure 6 of WAMDI (1988). The WAM results match the observational result of Hasselmann et al. (1980) very well. The Hasselmann empirical law is close to Mitsuyasu as

displayed in panel (a) of figure 3.7. Accordingly, the WAM spread is much broader than the K-model results and than the observational results of Donelan. Taking into account the superior quality of the Donelan results (Young 1994, Young et al. 1996c), it is concluded that the K-model directional spread is more realistic than the WAM spread. Apparently, the nonlinear interaction computation in WAM leads to an overestimation of directional spread. This was reported before, see e.g. Cardone et al. (1998).

The severe increase of K-model directional-spread parameters at the peak of large-fetch spectra and depth-limited spectra is unrealistic. As discussed above, this effect is caused by the directional characteristics of the wind input. It will be diminished if realistic directional gustiness is taken into account in the Snyder input source term. Assuming that this will improve the directional characteristics at the spectral peak, it is concluded that directional spread in wind seas depends to a large part on the directional characteristics of external energy-input processes, and not exclusively on internal nonlinear energy transfer.

The analysis of directional spread has been confined to an investigation of the spread parameter $s(f)$ defined in connection with the Mitsuyasu parametric directional distribution. This distribution is unimodal. Bimodal spreading for frequencies larger than twice the peak frequency was experimentally detected by Young et al. (1995). The K-model cannot reproduce this feature. It has been reproduced with a model using an exact numerical representation of nonlinear energy transfer (Young et al. 1993, Banner et al. 1994, Young et al. 1995). It was concluded in these studies that bimodal spreading is essentially caused by quadruplet nonlinear interactions.

3.2.2 Duration-limited Growth

Duration-limited growth is an idealized situation describing the development of a wave field from an initial state to full development in a homogeneous ocean with time-constant wind field. The problem is one-dimensional. Spatial homogeneity allows the neglect of propagation and refraction for reasons of symmetry. The wave spectra are functions of time only. The case can be computed with wave models on a one-point grid, only retaining the source-term integrations in the computations.

In contrast to fetch-limited growth, observational studies of duration-limited growth do not exist in the literature. The phenomenon is difficult to observe because requirements cannot be strictly fulfilled. This is because waves essentially propagate and thus contain information on distant coastlines and storm areas. There are only vague ideas based on subjective experiences, e.g. a nomogram for significant wave heights depending on wind speed and duration in the Shore Protection Manual (1984).

The SWAMP (1985) intercomparison study revealed substantial differences in the behaviour of first-generation models in duration-limited growth compared to second-generation models. After scaling all models to equal results in fetch-limited growth, the first-generation models VENICE and MRI exhibited much more rapid wave growth in the initial stage of duration-limited growth. Although it cannot be decided from comparison with observational evidence which behaviour is closer to reality, a comparison of K-model results with the described feature will allow a classification of the K-model behaviour with respect to this case. Furthermore, model

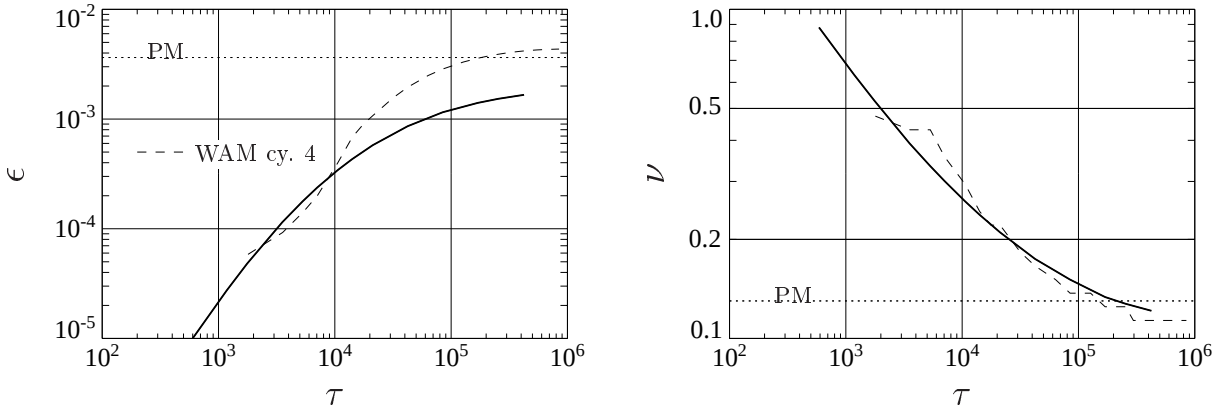

(a) Total energy ϵ vs. time τ

(b) Peak frequency ν vs. time τ

Figure 3.8: Growth curves for ϵ and ν as function of τ. Dashed and dotted lines show results of WAM cy. 4 and the Pierson-Moskowitz levels, respectively.

behaviour in idealized duration-limited situations can lead to an understanding of features in simulations of more complex systems.

3.2.2.1 Growth Curves

K-model computations for the duration-limited-growth case were performed with the tuning as given in the previous subsection. The prescribed wind speed was $u_{10} = 10$ m/s. Figure 3.8 displays growth curves of nondimensional quantities total energy and peak frequency versus time as computed by the K-model. Computations of the same case with WAM cy. 4 are given as dashed lines, the Pierson-Moskowitz levels appear as dotted lines. Comparison with the third-generation model WAM cy. 4 enables a qualitative relation of K-model results to the described findings of the SWAMP study.

1. In panel (a), growth curves for total energy are displayed. For large times, the K-model fails to reach the Pierson-Moskowitz level. This is analogous to the fetch-limited growth case, where this feature was accepted in favor of a correct reproduction of HRMS results for smaller fetches. In contrast, WAM reaches the Pierson-Moskowitz level.

2. Panel (b) shows growth curves for peak frequency. Here, the K-model reaches the Pierson-Moskowitz level for full development, analogous to the fetch-limited-growth behaviour.

Quantitative comparison with the WAM growth curves for both quantities must be performed with care. True duration-limited development starts in WAM only at time $\tau \approx 5 \times 10^3$. Before this time, influence of the prescribed initial state in WAM is apparent. This can be deduced from the unsmoothness of the WAM peak-frequency growth curve. If both growth curves of WAM are extrapolated roughly by eye to smaller times, a comparison with K-model curves shows that the K-model gives slightly larger results for total energy, but considerably smaller peak frequencies for small times. This corresponds qualitatively to the differences of first-generation models

in SWAMP to second-generation models. The K-model gives more rapid wave development for small times. However, a quantitative difference to the VENICE model can be found by comparison with figures 7.10 and 7.11 in SWAMP (1985). VENICE gives larger energies for small fetches, and fails to reach the Pierson-Moskowitz level for the peak frequency.

3.2.3 Relaxation of Swell

Analysis of swell relaxation in deep water is quite substantial in the context of this thesis. In the K-model formulation, the dissipation source function will be the only source function acting on the development of the wave spectrum in this case. Quantification of a relaxation time scale and its comparison with observational evidence is therefore a direct test for the validity of the nonlinear dissipation source function.

Observations of swell attenuation in deep water are sparse in literature. One experiment was reported by Snodgrass et al. (1966), henceforth referred to as Snodgrass. In this study, swell systems generated in southern parts of the Indian and Pacific Oceans were traced across the Pacific by measurement at six stations ranging from New Zealand to Alaska. A qualitative result was strong attenuation of swell close to the generation area, but very small attenuation beyond the first observing station. Tractability of swell was restricted to systems with small frequencies below 0.08 Hz, indentification of swell events was lost at higher frequencies. Quantitative results for attenuation were not reproducible but orders of magnitude were given. These will be compared with corresponding K-model results.

3.2.3.1 Model Results

Relaxation of swell in deep water is simple to treat in the K-model formulation, since in this case only nonlinear dissipation contributes to the sum of source functions in the dynamical equation. An analytical treatment will be described in the following paragraph. A subsequent paragraph covers a numerical experiment, in which K-model and WAM cy. 4 are compared.

Analytical Treatment. The Snodgrass experiment can be analysed with the K-model dynamical equation. To facilitate the analysis, it is presumed that the swell-generating wind field is time-independent and restricted to a limited area. The swell field between the points of observation and the location of generation will be stationary in this case (after a sufficiently long spin-up time). It is assumed further that the swell is unidirectional. The presumptions lead to a one-dimensional problem which is described by a dynamical equation similar to equation (3.1) of section 3.1. The Snodgrass results were given in terms of swell energy in different frequency bands. From unidirectionality follows that the spectrum is a function of wave number only. After transformation to one-dimensional energy spectra E_f (with respect to discretized frequency bands f) and retaining only nonlinear dissipation as source function, the dynamical equation of the problem reads

$$v_{\mathrm{g}} \partial_x E_f = \frac{\gamma (2\pi)^5 f^6}{2g^2} E_f^2 \,. \tag{3.21}$$

The distance to swell generation is denoted here by x. Equation (3.21) is actually a set of coupled ordinary differential equations for spectral energies $E(f)$ in different bins f. The coupling is

established via γ, which depends on the mean wave number of the spectrum, cf. equation (2.1) of section 2.3. To be able to proceed with an analytical treatment, γ will be considered as fixed, i.e. constant with respect to x, for each frequency bin f. This is a good approximation in the case of swell dissipation, since swell spectra are narrow-banded with constant mean frequency (in the absence of currents). The decoupling approximation leads to solutions for spectral energy in each spectral bin:

$$\frac{E_f(x)}{E_0} = \left(1 - E_0 \frac{\gamma(2\pi)^6 f^7}{g^3}\,(x - x_0)\right)^{-1}. \tag{3.22}$$

The solutions describe the decay of energy normalized to $E(f)/E_0$ in bin f as function of distance $x - x_0$, depending on initial energy E_0 at distance x_0. For large distances $x \gg x_0$, the decay is a power law in x with exponent -1. The nonlinear dissipation leads to an attenuation constant (the factor in front of $(x - x_0)$) depending on initial energy. A strong frequency dependency of the attenuation constant is present. It depends linearly on dissipation constant γ.

To assess whether nonlinear dissipation leads to swell attenuation consistent with the measurements of Snodgrass, the solutions (3.22) are compared with attenuation observations of swell events as given in figure 34 of Snodgrass. To this end, curves according to (3.22) are displayed in figure 3.9 for matching values of E_0 and f and compared with the Snodgrass attenuation rates. The initial energy was chosen to $E_0 = 3.16\,\mathrm{m^2 s}$, matching the characteristic values in Snodgrass of 15 dB above $1\,\mathrm{cm^2(mc/s)^{-1}}$. The frequency bands are the same as in figure 34 of Snodgrass. The dissipation constant was chosen as $\gamma = 0.1$, matching the choice of γ_0 in the K-model tuning presented in subsection 3.2.1. Figure 3.9 displays in addition relaxation curves according to the Snodgrass attenuation rates of 0.1 dB/deg and 0.05 dB/deg. These rates were given in Snodgrass for the frequency band of $f = 0.08\,\mathrm{Hz}$ to $0.075\,\mathrm{Hz}$, and the remaining bands respectively.

The K-model gives swell-dissipation results which are consistent with the observational study of Snodgrass. Qualitative features are reproduced, e.g. strong dissipation at small distances to the generation area depending on the initial energy of an event. The order of magnitude of measured attenuation rates of Snodgrass is reproduced by the K-model. The results give strong support to the concept of nonlinear dissipation in the K-model. Note that attenuation rates describe exponential decay. The corresponding curves therefore differ in shape from the power-law relaxation curves of the K-model, cf. figure 3.9 (a). But the attenuation results of Snodgrass exhibit large scatter. The specification of rates by Snodgrass was done to give orders of magnitude, not to point out a functional form of the relaxation curve.

It is pointed out that in the numerical K-model as presented in chapter 2.1, the value of γ as used in this analytical investigation will not be reproduced. The coupling functional will enhance the dissipation from γ_0 to a somewhat higher value below $p_1\gamma_0$, cf. section 2.3. This leads to enhanced swell dissipation. If the numerical model is to be applied in swell cases, an additional parameter should be introduced in the γ functional which reduces coupling for decreasing spectral widths. This has not been investigated in this thesis, however, because its primary purpose is analysis of a wave-modelling approach for small-scale shallow-water applications.

Numerical Experiment. To supplement the analytical results on swell relaxation, a numerical experiment is described here, in which relaxation of significant wave height with time is

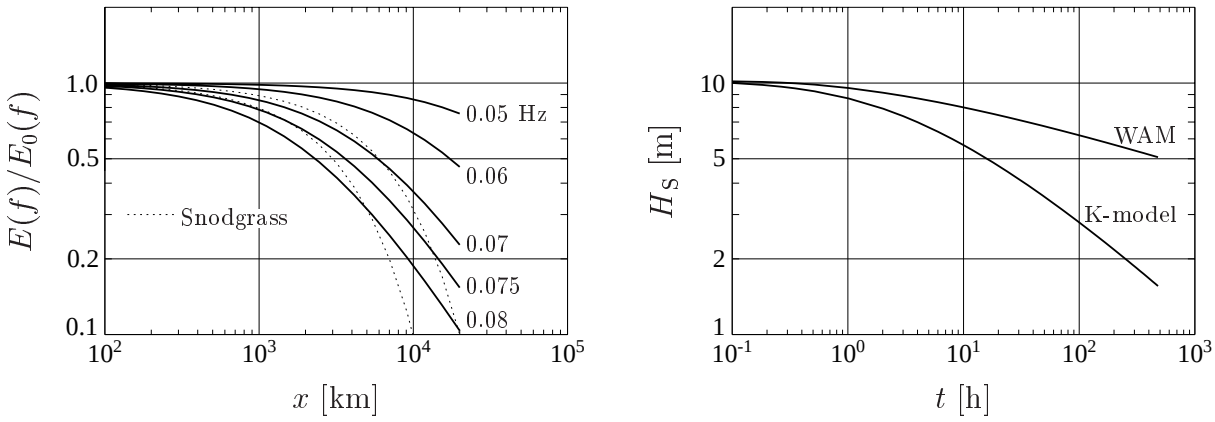

(a) Spectral energy $E(f)/E_0(f)$ vs. distance from source x

(b) Significant wave height H_S vs. time t

Figure 3.9: Panel (a): Development of spectral energy $E(f)/E_0(f)$ with distance x to generation. Labeling numbers indicate frequency bands f in Hz. The energy at location of generation is E_0. Dotted lines illustrate relaxation according to measured rates by Snodgrass et al. (1966). Panel (b): Significant wave height H_S versus time after a sudden wind turn-off. Results according to WAM cy. 4 and K-model are shown. The initial spectrum was a Pierson-Moskowitz spectrum for $u_{10} = 20$m/s.

studied. Model results of the K-model are compared with WAM cy. 4. The numerical experiment is performed on a one-point grid resembling a spatially infinite homogeneous deep-water ocean. A Pierson-Moskowitz spectrum corresponding to wind speed $u_{10} = 20\,\mathrm{m/s}$ is prescribed initially for both models. The wind speed is zero, the models thus describe attenuation of a fully developed wind sea. Results are given in panel (b) of figure 3.9. It displays relaxation curves for significant wave height H_S versus time t in a double-logarithmic plot for both models. The K-model gives a faster decay of wave height. For large times, the curve is a straight line approaching slope -0.5. This indicates a power-law decay of wave height. It matches the power law with exponent -1 which resulted for attenuation of energy in a frequency band with distance from generation, as given in the previous paragraph. The overall strong attenuation of wave height in the K-model results from strong dissipation of energy in moderate and high frequencies. Dissipation at low frequencies is very small, as was shown in panel (a) of the figure. WAM cy. 4 gives small overall decay of wave height.

3.2.4 Response to Turning Winds

The response of ocean waves in deep water to turning winds has been the subject of both observational and theoretical studies within the past two decades. In a pioneering observational study by Hasselmann et al. (1980), the response of frequency-dependent mean wave direction to turning winds was analysed. The subject of following papers by Günther et al. (1981), Allender et al. (1983), Holthuijsen et al. (1987), Masson (1990), and van Vledder et al. (1993) was the response of frequency-integrated mean wave direction $\langle\theta\rangle$, or mean direction of wave momentum. Van Vledder et al. (1993) performed a reanalysis which allowed the comparison of all listed studies regarding response time scales as function of peak frequency. This response

time scale τ was defined by Holthuijsen et al. (1987) in connection with a linear relaxation model

$$\partial_t \langle\theta\rangle = \frac{1}{\tau} \sin(\theta_\mathrm{w} - \langle\theta\rangle), \tag{3.23}$$

where θ_w denotes wind direction. A comparison of all observational results, cf. figure 3 in Van Vledder et al. (1993), revealed considerable scatter of almost an order of magnitude in τ. This was commented on in Holthuijsen (1994) as unsatifactory, and attributed to the use of linear relaxation models and difficulties in estimation procedures.

The observational studies by Günther et al. (1981) and Holthuijsen et al. (1987) were supplemented by computations with parametric ocean wave models. Further theoretical results were published by Young et al. (1987) and Van Vledder et al. (1993), both used the third generation wave model EXACT-NL (Hasselmann et al. 1985). Results of these studies will be compared with K-model results in the following paragraph. In SWAMP (1985), one test case was the response of the modelled wave field to a sudden shift of 90° in wind direction. Instead of relaxation time scales, time series of decay and development of old and new wind-sea peaks were analysed. The investigated models could be grouped into two classes, wind-sea/swell coupled and decoupled models, which behaved in a qualitatively different manner. The K-model will be related to this classification.

3.2.4.1 Model Results

In computational studies, the response of model wave spectra to changes in wind direction have been treated in the idealized case of a homogeneous ocean. The same has been done in this study. The developing wave spectrum is in this case a function of time only. The integration of the dynamical equation is once again a one-dimensional problem which can be solved on a one-point grid. Following the computational analysis of Van Vledder et al. (1993), sudden wind shifts of 30°, 45°, 60°, and 90° have been prescribed in the K-model computations, which ocurred in a developing wind sea at a peak frequency of twice the Pierson-Moskowitz frequency. The wind velocity was $u_{10} = 10\mathrm{m/s}$.

Time series of mean wave direction $\langle\theta\rangle$ starting at the time of wind shift are displayed in panel (a) of figure 3.10. Curves are labelled with the corresponding wind-shift angles. The K-model results can be compared with the EXACT-NL results given in figure 6 (a) of Van Vledder et al. (1993). Both models behave in a similar manner. The response in the K-model is slightly faster for the angles 90° and 60°, for the smaller angles the results are roughly the same.

In panel (b) of figure 3.10, K-model response time scales as function of peak frequency are displayed. To enable comparison with Van Vledder et al. (1993), nondimensionalization with u_* has been chosen. As in Van Vledder et al. (1993), the drag coefficient for the calculation of u_* from u_{10} was chosen according to Wu (1982). Data of all four wind-shift situations are included in the figure. The K-model results are very close to the regression line for the EXACT-NL computations given by Van Vledder et al. (1993). For small peak frequencies, values of the relaxation time are above an extrapolation of the regression line. This corresponds to results of Young et al. (1987) displayed in figure 11 of Van Vledder et al. (1993). For small peak frequencies, K-model relaxation times are smaller than the ones computed by Holthuijsen et al. (1987) and EXACT-NL, again cf. figure 11 of Van Vledder et al. (1993). The group of data

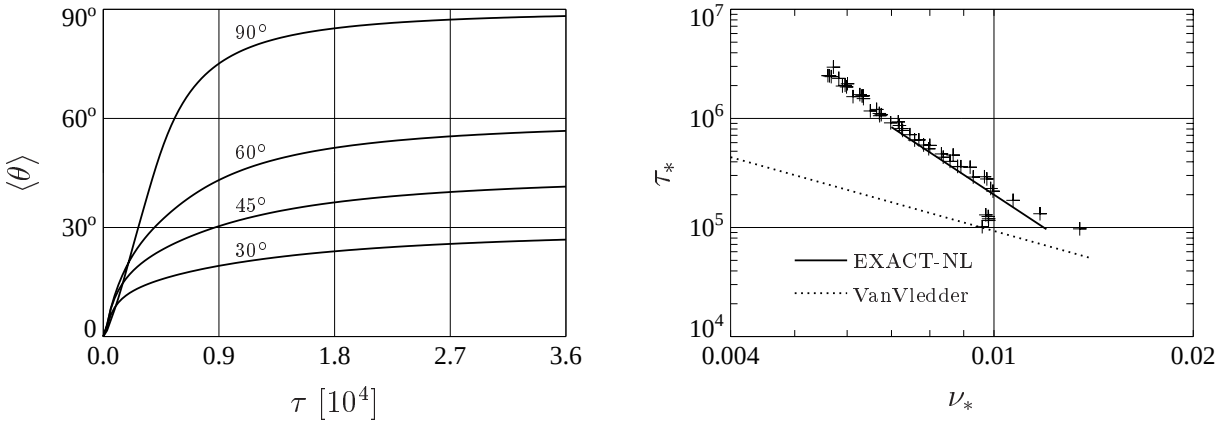

(a) Mean wave direction $\langle\theta\rangle$ vs. time τ

(b) Relaxation time τ_* vs. peak frequency ν_*

Figure 3.10: Panel (a): Development of mean wave direction $\langle\theta\rangle$ with time τ after a sudden wind shift of labelled angle. Panel (b): Relaxation time τ_* for response of wave mean direction to a sudden wind shift versus peak frequency ν_*, data for shifts of 30°, 45°, 60°, and 90° are included.

points at $\nu_* = 0.01$ and $\tau_* = 10^5$ corresponds to shifting mean wave direction in cases where the spectral peak has not changed to the new wind-wave system, yet. K-model results are withn the bulk of observational data. They agree best with the results of Günther et al. (1981). As for EXACT-NL, K-model relaxation times are larger than the observational data of Van Vledder et al. (1993), which are displayed in figure 3.10 (b) of this thesis as regression line to their data.

The dynamics of response to turning winds in the K-model is principally governed by decay of the old wind sea and development of a new wind sea in an independent, decoupled manner. The model is similar in this feature to the SWAMP models with decoupled wind-sea/swell treatment. But a principal difference is the nonlinear dissipation in the K-model. It acts mainly locally with respect to direction. The dissipation of swell energy is not very strongly coupled to the development of a new wind sea, because the dissipation does not depend on integrated energy, but on local energy. A weak coupling is present merely via the development of mean wave number in the new wind sea. In contrast to this, the model EXACT-NL includes directional coupling via nonlinear energy transfer and white-capping dissipation. The latter acts differently to nonlinear dissipation in this case, because its dependence on total energy results in a strong coupling of swell and wind sea. It is remarkable that both models give similar results for response time scales of mean wave direction, although the dynamical treatment of the problem is substantially different. Nonlinear transfer of energy seems to play a minor role in turning-wind cases. This was also indicated by the computational results of Van Vledder et al. (1993): main effects in the used model were attributed to wind input and white-capping dissipation.

3.3 Wave Model Validation: Wave Hindcast of a North Sea Storm Period

In this section, an application of the K-model in a wave hindcast of a North Sea storm in November 1981 is described. Comparison with other shallow-water wave models is possible because the same storm event was hindcasted in the SWIM intercomparison study (SWIM 1985). A parallel hindcast with WAM cy. 4 which was performed within this study will allow comparison with a state-of-the-art third-generation wave model. For results of this section reference is made to Schneggenburger et al. (1997).

3.3.1 Purpose

The hindcast serves as a test of the modelling approach realized in the K-model in a realistic application with time- and space-variable wind fields and space-variable bottom topography. Wave hindcast on corresponding length and time scales has been a major purpose to develop today's ocean wave models like WAM cy. 4. It will be investigated here if the K-model concept leads to comparable hindcast quality in these scales. However, it is not the primary purpose of this study to introduce an improved modelling approach for large and intermediate scales. Emphasis is set on small-scale applications, where the K-model conceptual idea has advantages over the modelling approaches of existing third-generation models. The purposes of the North Sea storm hindcast with the K-model can be summarized as follows:

1. Show the K-model performance in a shallow-water shelf-sea application and compare with the SWIM models and WAM cy. 4
2. Show the applicability of the modelling approach to intermediate scale systems
3. Justify the use of the K-model as a coarse-grid model for small-scale applications.

The last point will be important in the next chapter, where the K-model setup as used here will serve as model to deliver boundary spectra for small-scale applications in the Sylt-Rømø tidal basin.

3.3.2 Model Setup

The North-Sea storm event 20th to 26th November 1981 was selected in the SWIM intercomparison study of operational shallow-water wave models (SWIM 1985) because it fulfilled two essential requirements: available wind fields for forcing of the models and available wave measurements at a number of stations for validation. The storm has been selected in the present study to take advantage of the SWIM results for a comparison of the K-model with the SWIM wave models and with measurements.

The area of investigation surrounding the North Sea is illustrated in figure 3.11, which gives the computational grid of K-model and WAM. Contour lines illustrate the bathymetry. Three field stations of interest are indicated:

1. Station Fulmar at 56.4°N 2.1°E, depth 80 m (deep)

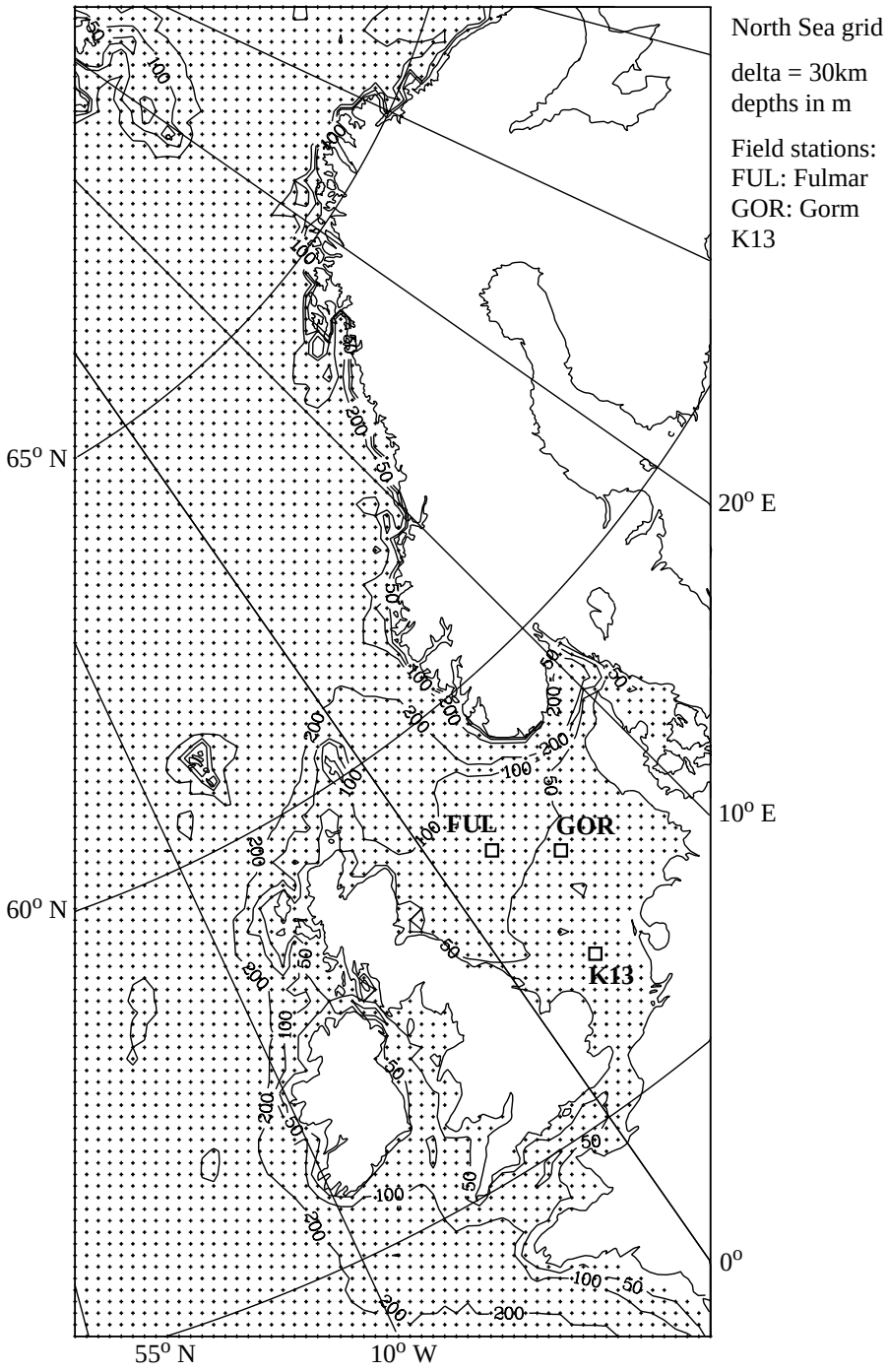

Figure 3.11: Fine grid of K-model and WAM for the SWIM North Sea storm hindcast. Crosses indicate grid points. Contour lines illustrate water depths. The locations of field stations Fulmar, Gorm, and K13 are given.

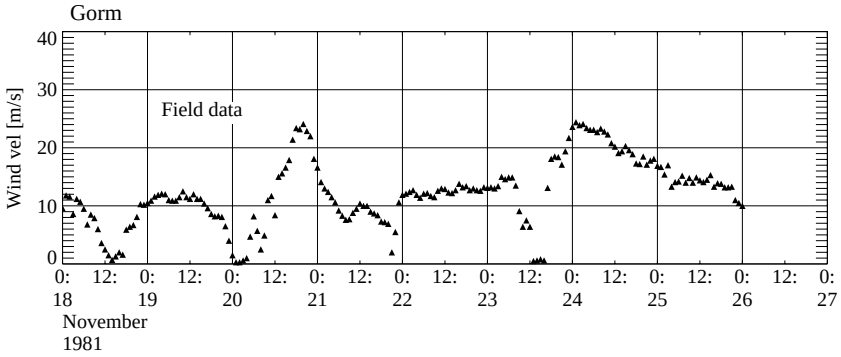

Figure 3.12: Time series of wind velocity u_{10} at North Sea station Gorm.

2. Station K13 at 53.2°N 3.2°E, depth 28 m (shallow)

3. Station Gorm at 55.6°N 4.8°E, depth 32 m.

The North Sea at Fulmar, its northern part, and its extension into the Norwegian Sea and the Atlantic can be termed deep-water areas in the context of wave modelling. The water depths are larger than 80 m. The southern North Sea, around station K13, is shallow. Here, water depths decrease to roughly 20 m to 30 m.

The synoptical situation of the selected period can be characterized as follows, cf. SWIM (1985). The period was dominated by two consecutively passing active low-pressure areas. The first one was fast moving over the North Sea on 21st November, producing a WSW wind above $u_{10} = 30$ m/s in a short peak of about two hours in the central North Sea at Fulmar. Winds in the south-easterly part were W 25 m/s six hours later. The next two days had reduced winds of WSW 10 m/s to 15 m/s due to a weak high-pressure ridge over the North Sea. A second low-pressure area moving more slowly from Scotland to Scandinavia on 23rd and 24th November produced on the 24th northerly winds throughout the North Sea, at Fulmar again above 30 m/s, and this time more sustained. The maximum wind speeds at K13 were roughly 20 m/s for both storm peaks. Wind velocities measured at station Gorm illustrate the synoptical situation in the hindcast period, see figure 3.12. This station has been chosen for the figure because of the quantity of available wind measurement data.

Wave models in the SWIM STUDY were the UK Meteorological Office Operational Wave Model (BMO), the KNMI Operational Wave Model (GONO), and the Hybrid Parametrical Shallow-water Wave Model (HYPAS), which is operational at DWD. Following SWIM (1985), validation and comparison are performed at stations Fulmar and K13, which represent deep-water and shallow-water situations. Measurements at Fulmar were available from wave staff and electromagnetic current meters. K13 measurements were performed with a waverider buoy. In both cases, H_S and T_{m1} were integrated from one-dimensional wave spectra. These are the two parameters for the validation and comparison. The wind fields used for the hindcasts computed with WAM and K-model for the purpose of this thesis are the production wind fields of the NESS (North European Storm Study) 1986-1991 Project (NESS Project Consortium 1992). These winds may be slightly different from the winds used in the SWIM study. In particular, the NESS winds are only given in time steps of six hours. The SWIM wind time step was

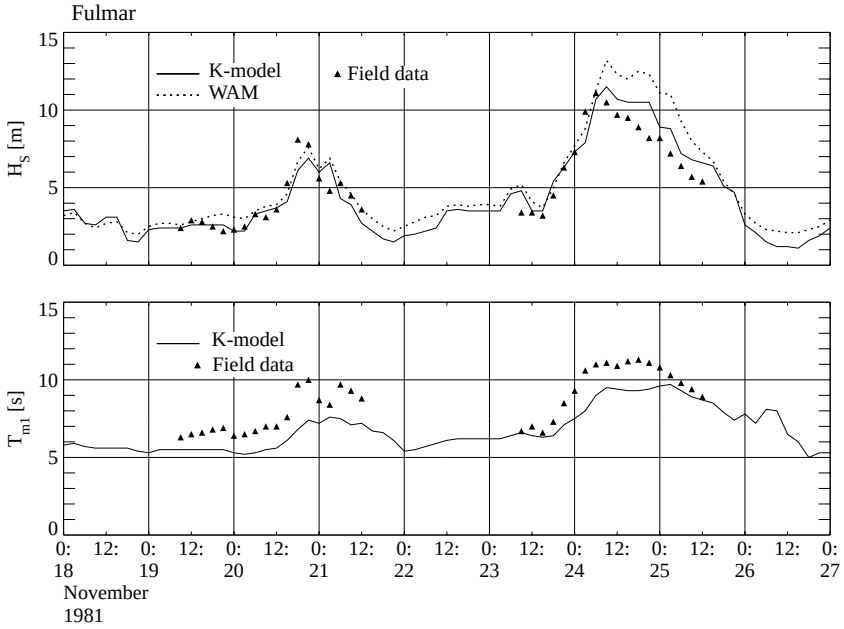

Figure 3.13: Time series of wave parameters H_S and T_{m1} at North Sea station Fulmar.

three hours. This can be a problem especially in the case of the fast-moving first storm peak. Fortunately, the local peak at station Fulmar ocurred at midnight and is thus resolved in the K-model and WAM hindcasts.

The hindcasts with K-model and WAM have been performed in the time period 18th to 27th November. For both models, a deep-water coarse-grid run covering the North Atlantic in a grid resolution of 150 km delivered boundary spectra for the fine grid. The fine grid is illustrated in figure 3.11. It has a resolution of 30 km $\times$ 30 km. The tuning for the K-model has been

1. Nonlinear dissipation: $\gamma_0 = 0.06775$, $p_1 = 4$, $p_2 = 1.2$, and $q = 8$
2. Snyder input: $\beta = 0.0006$
3. Bottom interaction: $\Gamma = 0.01\,\mathrm{m}^2/\mathrm{s}^3$.

This calibration has also been used for the computations displayed as thin lines in figures 3.3 and 3.4 of section 3.2, and in Schneggenburger et al. (1997). In the next subsection, results of the hindcast experiment will be given and discussed.

3.3.3 Hindcast SWIM Storm

Time Series. Time series of significant wave height H_S and integrated period T_{m1} at stations Fulmar and K13 are given in figures 3.13 and 3.14. Hindcast results of K-model and WAM, and field data are given in the figures. For comparison with the SWIM models, reference is made to figures 14 and 16 in SWIM (1985). Small deviations of model results between K-model (and WAM) and the SWIM models must be expected from the use of different wind fields in the hindcasts.

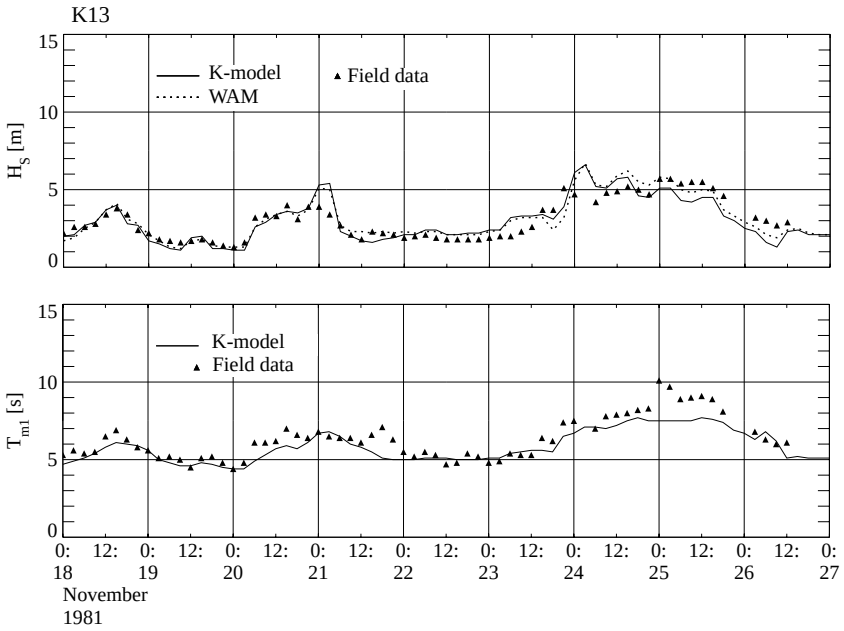

Figure 3.14: Time series of wave parameters H_S and T_{m1} at North Sea station K13.

Computed significant wave heights H_S of K-model and WAM are similar at station K13. At Fulmar, WAM and K-model deviate during the second storm peak, where WAM gives waves nearly 2 m higher. The agreement of both models with the field data is good except for minor deviations during the storm peaks at K13 and a major overestimation of wave heights on 24th and the beginning of 25th November at Fulmar. Here, the K-model is approximately 1 m too high, whereas WAM deviates by 2 m to 3 m from the measurements. Compared to the SWIM models, K-model and WAM give more satisfying results for the first storm peak at Fulmar. Both approach the peak fairly well and come close to the maximum value of 8 m, WAM better than the K-model. The SWIM models either overestimated the approach and agreed with the peak (GONO), or gave a satisfying approach but failed to come close to the peak wave height (BMO and HYPAS). The approach to the second storm peak at Fulmar is modelled in a much better way by K-model and WAM. But since the maximum height and decay is largely overestimated by WAM, the SWIM models do better at this stage of the hindcast. The K-model gives the correct maximum wave height, but in the decay of the second storm peak compares with the moderately high results of GONO and HYPAS. Comparing all models, the measured wave heights of the second storm peak at Fulmar are best reproduced by the K-model. At K13, K-model and WAM give similarly good results as BMO and HYPAS during the first storm peak and the following moderately calm days. GONO generally overestimates measured wave heights in this period, but agrees better with the measurements during the second peak. Here, K-model and WAM exhibit some variations not present in the SWIM model results which may be due to the differing wind fields.

Results for the T_{m1} period are not given for WAM, because T_{m1} is not a standard output parameter of the model. The K-model periods agree well with measurements at K13 except for an underestimation at the second storm peak. The periods at Fulmar are underestimated

by the K-model throughout the hindcast period, especially strong at the storm peaks. The SWIM models behave similarly to the K-model with respect to T_{m1} periods at K13. They also underestimate at the second peak. At Fulmar the SWIM models give better results than the K-model, but all models underestimate the periods during the storm peaks. Only HYPAS can reproduce the maximum period of 11 s, but delayed by eight hours. BMO and GONO give maximum periods of almost 10 s, whereas the K-model reaches a maximum of 9.5 s.

Table 3.1: Validation statistics for wave heights H_{S} at two North Sea stations from 20th to 26th November 1981 for various wave models. The number of observations is denoted by n. $\overline{H}_{\mathrm{S}}$ is the mean of observed wave heights. See appendix A.4 for a definition of statistical parameters.

Location	n $\overline{H}_S$ [m]	Model	Model depth [m]	Mean height error [m]	rms height error [m]	Scatter index	No. of positive errors	No. of negative errors
Fulmar	31	K	79	0.3	1.1	18	18	10
	6.1	WAM	79	1.1	1.8	31	26	4
		BMO	82	−0.4	1.1	19	11	20
		GONO	80	0.4	0.9	14	23	8
		HYPAS	75	−0.4	1.5	24	12	19
K13	50	K	31	−0.1	0.8	24	22	28
	3.3	WAM	31	0.1	0.7	20	29	18
		BMO	27	−0.2	0.4	13	19	31
		GONO	25	0.4	0.5	14	40	10
		HYPAS	31	−0.1	0.5	16	26	24

Validation Statistics. The validation statistics for wave heights and periods at stations Fulmar and K13 are given in tables 3.1 and 3.2. As above, WAM results are only given for wave heights. Although the time series of K-model and WAM exceed the ones given in SWIM (1985) by three days, the same field data points have been used for the statistical validation. For a definition of statistical parameters reference is made to appendix A.4. Note that the scatter index is defined here according to SWIM (1985), involving the rms error. Today, an alternative definition involving the standard deviation of the data set is commonly used in the wave modelling community.

The validation statistics give a quantification of model performances which were seen in the preceding paragraph by discussion of the time series. The statistics do not reveal additional features in the case of this hindcast, but merely support the behaviour described above. With respect to wave heights at Fulmar, the validation statistics of the K-model compare well with the SWIM models. The rms error and scatter index of wave heights are slightly less satisfying for the K-model at K13. This may stem from the deviations at the time of the second storm peak, which was discussed above as possibly due to differences in the forcing wind fields. Especially in comparison to WAM, the K-model statistics are satisfying. However, the WAM statistics are obscured by the severe overestimation of wave heights during the second storm peak at Fulmar.

Table 3.2: Validation statistics for wave periods T_{m1}, annotation as table 3.1. $\overline{T}_{\mathrm{m1}}$ is the mean of observed periods.

Location	n $\overline{T}_{m1}$ [s]	Model	Model depth [m]	Mean period error [s]	rms period error [s]	Scatter index	No. of positive errors	No. of negative errors
Fulmar	31	K	79	−1.4	1.5	18	0	31
	9.0	BMO	82	−0.6	0.7	8	8	23
		GONO	80	−0.7	0.9	10	4	27
		HYPAS	75	−0.7	0.9	10	7	24
K13	50	K	31	−0.6	0.9	14	11	37
	6.6	BMO	27	−0.2	0.6	9	20	30
		GONO	25	−0.1	0.7	10	21	29
		HYPAS	31	−0.3	0.7	10	19	31

In the case of T_{m1} periods, all models have negative biases at both stations. The K-model performs slightly less well at K13, but considerably less well at Fulmar. This corresponds to the discussion of time series as given above.

Concluding Discussion. Time series and validation statistics have shown that the K-model gives satisfactory results for significant wave heights, but the periods are too low. This fact is consistent with a disagreement of the K-model ϵ-ν relation (valid for the North-Sea calibration) with the HRMS empirical law, cf. figure 3.4. The use of a modified calibration which agrees better with HRMS should therefore improve the model performance for T_{m1}. A calibration of this kind is the one given in section 3.2.1, which was used in the computations of academic test cases, section 3.2, and of small-scale applications, chapter 4.

It has been shown in this section that the K-model conceptual idea can lead to a satisfying quality in wave-parameter hindcasts in intermediate- and large-scale applications. It is thus justified to use the K-model as a coarse-grid model for the delivery of boundary conditions to small-scale applications. This is done in the K-model applications which will be discussed in chapter 4.

3.4 Summary

In this chapter various aspects of spectral wave modelling with nonlinear dissipation have been investigated. The K-model served as principal tool for the investigation. The analysis has been performed in three parts. In a first section, important features of the modelling approach were clarified by an analysis of the K-model dynamical equation in simple cases and simplifying approximations. The second section covered a quantitative analysis of model behaviour in idealized "academic" test cases. In the last section of this chapter, the quality of a wave model with nonlinear dissipation in a realistic geophysical application was demonstrated by a hindcast experiment which was performed with the K-model. The following general conclusions can be

drawn from the results of these investigations:

1. The model formulation allows analytical treatment in simple cases. This has led to a thorough understanding of basic model features. A spectral tail exists which is sensitive to wind speed, water depth, and currents. Its functional form agrees with most recent theory. A stationary state exists. It is determined by a balance of source functions in the model. Depth limitation of peak frequency has been analytically confirmed and quantified.

2. The modelling approach leads to quantitative agreement with observations in a range of small and moderate nondimensional fetches ($\chi < 10^4$). In idealized situations, there are similarities and differences to existing models of all three generations. The K-model cannot be classified into any one of these categories. Some qualitative differences to second- and third-generation models directly result from the neglect of nonlinear energy transfer in the K-model. However, this never leads to disagreement with observational evidence in the specified fetch range.

3. In a North-Sea application, statistical validation showed that the hindcast performance of a wave model with nonlinear dissipation is satisfying and comparable to other models.

The given conclusions indicate that satisfying K-model performance can be expected in applications to geophysical systems characterized by limited fetches. The above specified criterion can be checked by dimensional analysis of involved scales. This will be done in chapter 4 as part of the analysis of wind waves in the Sylt-Rømø tidal basin.

4 Wave Model Applications to the Sylt-Rømø Tidal Basin

In this chapter, applications of the K-model to the Sylt-Rømø tidal basin will be described. The area of investigation and the setup of the model system will be introduced. Results from two case studies for prescribed wind situations and a one-month hindcast will be discussed. Conclusions from these numerical experiments will address the applicability and performance of the K-model as well as dynamical features of the investigated coastal system. Results of the chapter can be in part found in Schneggenburger et al. (1998).

4.1 Area of Investigation and Model System

4.1.1 Sylt-Rømø Tidal Basin

The Sylt-Rømø tidal basin is located off the North Sea coast adjacent to the Danish German border. The basin is enclosed by the islands Sylt and Rømø. Both are connected to the main land with artificial dams. This leaves only one opening to the North Sea. The bathymetry of the basin is shown in figure 4.1. The basin is approximately 30 km long and 20 km wide. The opening to the North Sea between Sylt and Rømø has a width of about 3 km. This opening is the only tidal inlet to the basin. There are three tidal channels within the basin with water depths of 5 m to 10 m. The remaining parts of the water body are less than 3 m deep. Large areas – the tidal flats – fall dry at low tide. The approximate tidal range is 2.3 m. Tidal currents can have velocities of up to 2 m/s in the inlet. In the tidal channels the current velocities usually are less than 1 m/s. The currents over the tidal flats are weak compared to those in the channels. Figure 4.1 indicates the location of various measurement stations. The Sylt-Rømø tidal basin was chosen as test area of the K-model for a number of reasons:

1. Since there is only one narrow opening to the North Sea, the wave regime in the Sylt-Rømø tidal basin is expected to be dominated by wind waves. Waves over flooded tidal flats will be depth-limited. Resulting from the short fetches, the wave group velocities will be of the same order of magnitude as the current velocities. For this reason, a considerable influence of the tidal currents on the waves is expected.

2. The opening of the basin to the North Sea is particularly suitable for realistic current modelling. A current model can be driven with measured water-level gauges at the basin entrance, as will be described below.

3. Recent interest in suspended-matter dynamics and morphology of the basin creates the demand for wave modelling in the area in order to be able to predict mobilization of sediments by wave/bottom interactions.

4. Wave model results can be validated using wave measurements from recent field campaigns carried out by GKSS.

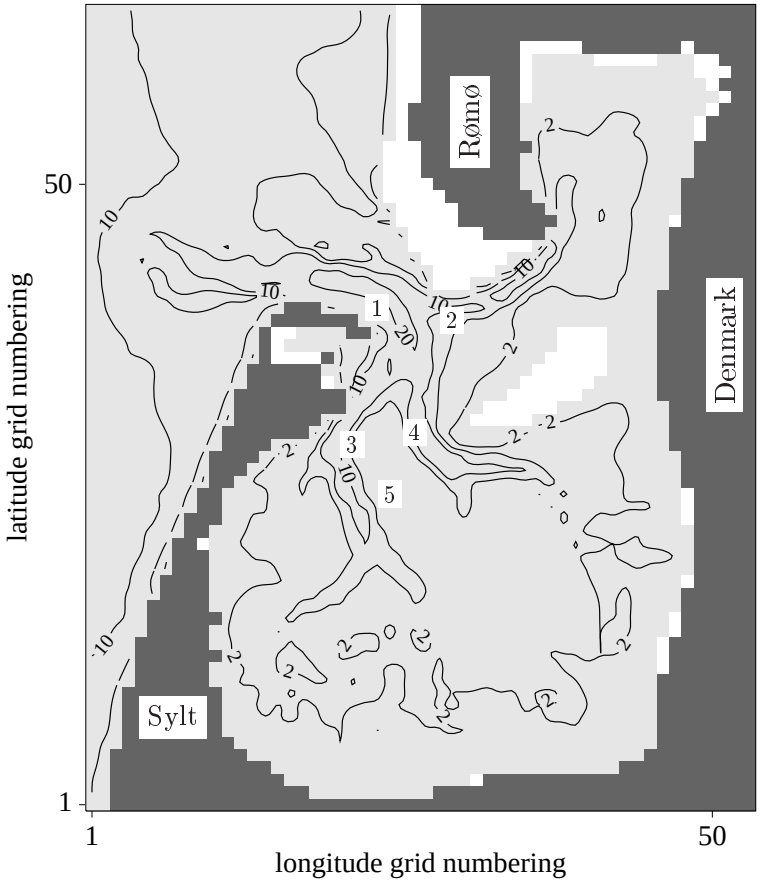

Locations of interest:

1: Lister Tief
2: P3 Rømø Dyb
3: P1 Lister Ley
4: P2 Højer Dyb
5: P4 Hunnigensände

Figure 4.1: Bathymetry of the Sylt-Rømø tidal basin. Land points are dark grey, dry sea points are white, and wet sea points are light grey. Water depths represent levels at a selected high tide. Contours show depths of 2 m, 5 m, 10 m, and 20 m. Numbers in white boxes indicate five field stations of interest.

4.1.2 Relevant Dimensional Scales

It will be shown in this subsection that following from the physical dimensions of the system, the sea state in the Sylt-Rømø tidal basin is essentially instationary and characterized by finite nondimensional fetches. Both of these results justify the use of the K-model for investigation of the wave regime in this area.

Instationarity. Surface winds, water levels, and currents are external fields which influence development of the wave field in a given area of investigation. Time variations of external fields are easily taken into account in the frame of the K-model, cf. section 2.3. But the significance of these variations for the sea state in a given area of investigation at a specified time is not obvious. It depends roughly on the ratio of a characteristic time scale of the wave field in that area to the time scales of variation of the external fields. Tolman (1990) analysed the characteristic scales for wave-modelling applications in tidal shelf seas and concluded that tidal currents form an essentially inhomogeneous and instationary medium for wind wave propagation in these cases. This result was confirmed in wave-modelling experiments in the North Sea. An influence of tides and storm surges on mean wave parameters was detected which could not

be sufficiently described with quasi-homogeneous and quasi-stationary approximations (Tolman 1991a). Tolman (1990) pointed out further that for small-scale coastal applications, currents can usually be treated as time constant, or in quasi-stationary approximation. This point of view was also adopted by Holthuijsen et al. (1993) in the stationary SWAN model. The model can be applied very efficiently to analyses of coastal wave fields at fixed points in time.

The quality of a stationary treatment in small-scale coastal wave modelling must be checked with a dimensional analysis of scales for each individual application. A characteristic time scale of the wave field in a regarded system is the travel time of typical waves, say waves at the peak of a typical spectrum, through the system. It can be estimated as ratio of the spatial dimension of the system to the peak group velocity, which describes the dominant propagation velocity of spectral wave action. Typical time scales for variation of external fields can be deduced from measurements. Stationary treatment will be possible if

$$\Psi = \frac{\text{travel time}}{\text{time scale of variation}} \ll 1 \tag{4.1}$$

holds. To carry out the analysis, an estimation of the orders of magnitude of the scales for the case of the Sylt-Rømø tidal basin is now performed. The wave regime in the basin is dominated by locally generated wind waves with peak frequencies down to 0.2 Hz. This can be inferred e.g. from measurements as given in section 4.3. Corresponding group velocities at the peak are below 5 m/s. The spatial dimension of the basin is roughly 20 km. The travel time of spectral wave action through the basin is accordingly larger than one hour. Measurements of tidal currents shown in figures 4.14 and 4.15 show that substantial variations in time of tidal currents can occur within one hour. The ratio of travel time to time scale of variation of the medium, parameter Ψ, is thus of order one. It follows that stationary treatment of wave modelling in the specified system is inappropriate.

Limited Fetch Range. It was concluded from section 3.2 that a calibration of the K-model exists which gives results of fetch-limited wave growth comparable to observations in a nondimensional fetch range $\chi < 10^4$. It will be shown here that relevant fetches in the Sylt-Rømø tidal basin fall in this range.

Nondimensional fetch $\chi = g\,x/u_{10}^2$ is not limited in a given area of investigation since it increases with decreasing wind speed. But interest in sea states is restricted to wave heights above an individually defined minimum value. Consider a wind speed $u_{10} = 5$ m/s. Physical fetches in the Sylt-Rømø tidal basin are below $x = 20$ km. This corresponds to $\chi = 8 \times 10^3$ for the given wind speed. The empirical fetch growth law of HRMS (Hasselmann et al. 1976) gives a significant wave height $H_S = 0.36$ m in this case. This is of the order of magnitude of an individually defined minimum wave height which can be of interest. It is inferred that wind speeds below $u_{10} = 5$ m/s are not of major interest for a wave model user. The corresponding relevant nondimensional fetches in the Sylt-Rømø tidal basin are thus below $\chi = 10^4$, which is the desired conclusion.

4.1.3 Setup of Model System

Wave modelling in the Sylt-Rømø tidal basin must be performed as part of a model system. Current modelling is inevitable for the specification of water levels and the distribution of

tidal flats, even if the influence on waves by the currents themselves should prove to be of minor importance. For realistic wave modelling, mesoscale structures of the wind field should also be considered (it has not been done in this study). This suggests the application of a mesoscale atmospheric model. Since quite large efforts are needed to fulfill these requirements, it is especially important to have an efficient code for the wave modelling, as has been realized in the K-model by neglect of quadruplet nonlinear interactions.

Current Model. For the specification of current and water-level fields, the model TRIM3D (Casulli et al. 1992, 1994) was applied. The model was used before e.g. for the creation of a current climatology of the Sylt-Rømø tidal basin (Behrens et al. 1997). Results of these computations are used for the case studies with east and northwest wind. The current model was set up by Behrens et al. with the following features:

1. TRIM3D was applied in two-dimensional, hydrostatic, barotropic mode.
2. A rectangular computational grid with 100 m $\times$ 100 m resolution was used, with a bathymetry as described in Behrens et al. (1997).
3. The open boundary of the model area was installed at the basin entrance to enable the use of measured water levels as boundary conditions.
4. Input parameters for model forcing were: water levels at the boundary, and six-hourly surface winds from the DWD (German Meteorological Office) Europe model, interpolated to one-hourly, homogeneous input fields. For the case studies, space- and time-constant winds of east and northwest 20 m/s were used.
5. The boundary water levels were obtained from measurements at Westerland, located on the seaward coast of Sylt. These measurements were transformed to basin-entrance water levels by linear regression. The regression line was obtained from periods in which field data were available for both locations. For the case studies, representative periods of two to three days with matching wind situations were selected. In this way, realistic water-level forcing, including complex tide and wind effects representative for the chosen weather situation, could be obtained.
6. As model output, two-dimensional current fields and water-level variations were obtained within the basin.

Wave Model. The K-model was run with a calibration to HRMS growth laws, valid for a nondimensional fetch range $\tilde{x} = 10^2$ to 10^4, as given in subsection 3.2.1.2. Calibration to Kahma et al. (1992) growth laws led to an overestimation of wave heights in the Sylt-Rømø application, because these laws predict larger energies at small fetches. Details of the K-model setup for the two numerical experiments are listed in the following:

1. A 500 m $\times$ 500 m resolution grid was chosen, see figure 4.1. The bathymetry is a coarser version of the current-model bathymetry. It was obtained by selecting one in every five grid points of the 100 m $\times$ 100 m grid. The used selection avoids unrealistic land sea patterns in the northern part of Sylt.

2. The K-model spectral resolution was 12 directions and 25 wave numbers. The output frequency axis ranged from 0.1 Hz to 1 Hz, from 0.04 Hz to 1 Hz for the case studies. The spectral directions were shifted to avoid propagation directions into principal grid directions.

3. The source-term-integration time step was 60 s. Propagation, current-refraction, and depth-refraction time steps were 20 s, 20 s, and 4 s, respectively. The small depth-refraction time step is caused by large depth gradients. It is no major obstacle, since depth refraction is only a small part of all propagation and refraction computations. For the choice of time steps, care was taken to avoid a mismatch between propagation and source-term integration, since this can lead to oscillatory peaks as observed before in other small scale applications (Schneggenburger et al. 1997b).

4. As wind input, stationary and homogeneous $u_{10} = 20\text{m/s}$ with directions (coming from) east and northwest was prescribed for the case studies. In the hindcast experiment, the wind measured at station P3 Rømø Dyb (see figure 4.1) was transformed to u_{10} assuming a logarithmic profile and the Charnock relation to provide the roughness length (e.g. Komen et al. 1994). This wind was applied homogeneously with a time step of 15 minutes. No time interpolation was performed. The preference of measured winds as input fields over e.g. DWD model winds will be discussed in subsection 4.3.1.

5. Water levels and currents were provided from the described TRIM3D runs. The 100 m output resolution was reduced to the wave-model resolution. Water depths at the grid boxes representing the field stations P1 Lister Ley and P3 Rømø Dyb were adapted to measured values to ensure correct local processes for the wave modelling. The water-level and current-input time steps were 15 minutes, no time interpolation was performed. The wave-model computational area extends out into the North Sea. Beyond the boundary of the current-model grid, zero currents and stationary water levels were prescribed.

6. For the hindcast study, boundary spectra were provided from a North Sea 30 km $\times$ 30 km resolved K-model run with setup similar to the one described in section 3.3. The model was driven with DWD-Europe-model six-hourly wind fields. The spectra from a corresponding grid point of the North-Sea model were transformed to match the (k, θ) axes of the small-scale model, and distributed to all boundary points with water depths larger than 3 m. The boundary-value-input time step was 15 minutes.

7. For the east-wind case study, boundary spectra were obviously not needed. For the northwest-wind case, a matching date from the hindcast period was selected to obtain a realistic boundary spectrum.

4.2 Case Studies for Strong East and Northwest Winds

The case studies in the Sylt-Rømø tidal basin have been performed to demonstrate the applicability of the K-model in investigations of wave climate in coastal environments. Emphasis in the studies is set on the analysis of tidal impact, in particular tidal current impact, on the sea

state. The current impact will be analysed by comparison of model results with wave/current interaction switched on and off. The cases have been chosen to represent contrary meteorological situations. A different quality of current effects can be expected for the two because wave directions will be considerably different, whereas current directions roughly stay the same.

4.2.1 Model Results

The model periods for the case studies were fixed by the available current and water-level fields from the current atlas of Behrens et al. (1997): two days in February 1994 for the east 20 m/s case, and three days in June 1994 for the northwest 20 m/s case. Results are given in four paragraphs which contain, for both cases, wave-parameter fields at selected times, wave-parameter difference fields for model runs with current input and without, wave- and current-parameter time series at selected locations, and selected two-dimensional spectra. To facilitate notation, the acronyms E20 and NW20 will be used for wind at ten meters height of east 20 m/s and northwest 20 m/s, respectively.

Parameter fields. An impression of the wave climate in the Sylt-Rømø tidal basin can be obtained from figure 4.2, in which fields of significant wave height and T_{m1} period for the E20 and NW20 cases at selected high tides are displayed. In panels (a) and (c), wave heights in meters are represented by contour lines. Wave directions are given by arrows whose lengths are scaled proportional to significant wave height. Panels (b) and (d) give contour lines of T_{m1} periods in seconds. Grey shades are as in figure 4.1, e.g. temporarily dry points are white.

General features visible from parameter fields of both case studies are listed in the following.

1. Water levels for the NW20 case are higher at high tide than for the E20 case, as is obvious from an increased number of dry gridpoints in the E20 case. This is caused by wind-driven currents leading to water-level setup in the NW20 case, and the opposite effect for the E20 case. The result shows that water levels are realistically modelled in the current model by utilization of measured gauges at the basin entrance. These gauges contain information on wind-driven currents in the open North Sea.

2. Waves in the inner parts of the basin are strongly depth-influenced. This is visible for both cases from spatial patterns in the wave parameters resembling the structure of topography in the basin. Depth influence can be quantified by assessment of the parameter $\omega_h = \omega\sqrt{h/g}$ which determines the Kitaigorodskii factor Φ_{K} (Kitaigorodskii et al. 1975) used for shallow-water scaling in the TMA spectral shape (Bouws et al. 1985). Roughly it can be stated that significant depth influence is present for $\omega_h < 1$, noticeable influence for $\omega_h < 1.5$. These numbers correspond to values of Φ_{K} of 0.5 and 0.9, respectively. To assess ω_h values from within the basin for the two cases, water depths of figure 4.1 and T_{m1} fields of figure 4.2 as measure for peak frequencies can be used. This assessment indeed reveals strong depth influence in the inner parts of the basin. Wave heights are below 1 m and T_{m1} periods below 3 s in both cases due to this effect.

Features typical for either case E20 or NW20 are briefly described in the next list.

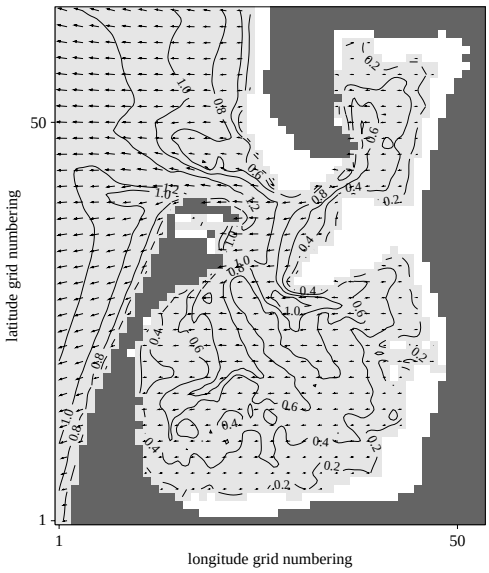

(a) Case E20 significant wave heights

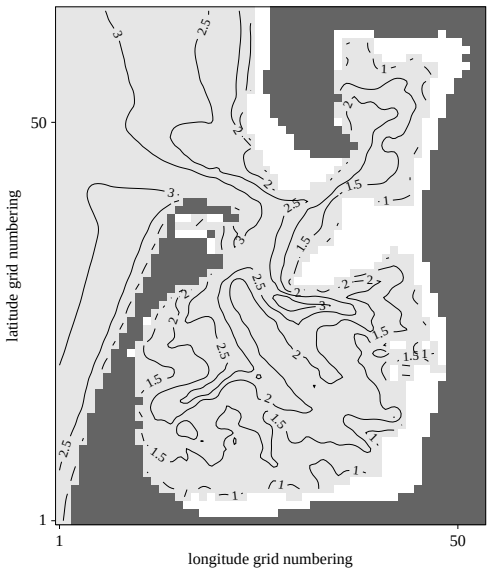

(b) Case E20 T_{m1} periods

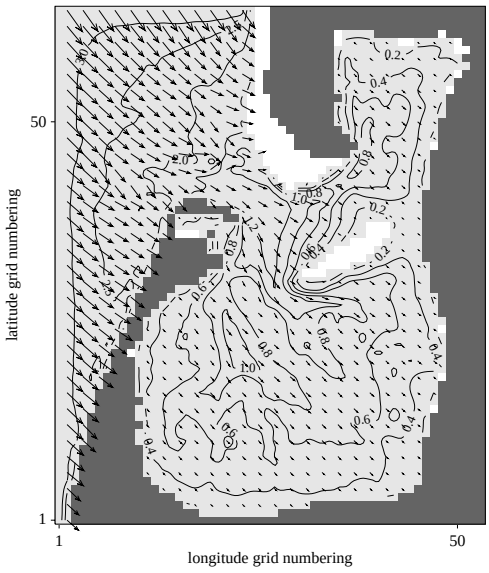

(c) Case NW20 significant wave heights

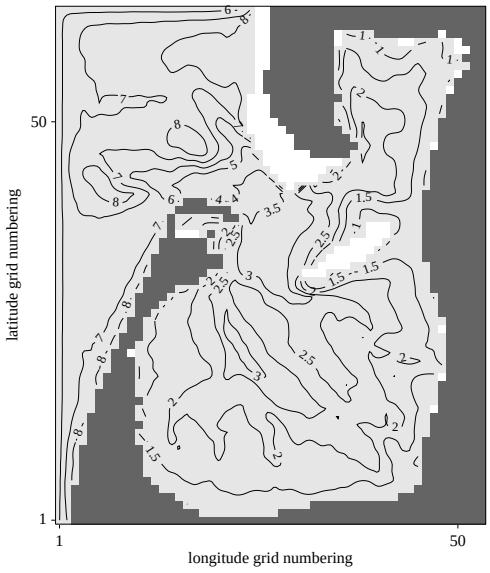

(d) Case NW20 T_{m1} periods

Figure 4.2: Fields of wave parameters for the two cases at selected high tides. In panels (a) and (c), contour lines represent wave heights in meters. Arrows give wave directions. Arrow lengths are scaled proportional to significant wave height. In panels (b) and (d), contour lines give T_{m1} periods in seconds. Grey shading as in figure 4.1.

1. For the E20 case, results consistent with fetch-limited growth and slanted fetch conditions are visible outside the basin. These are disturbed by increased fetch at the basin entrance. Fetch-limited growth within the basin is strongly depth-influenced.

2. In the NW20 case, wave heights and periods at the western and northern boundaries to the open North Sea are fixed by provided time-constant boundary spectra. Wave heights decrease with increasing distance from the boundaries, whereas the periods increase. This is caused by a dynamical balance of shallow water dissipation and shoaling. The shoaling increases T_{m1}, whereas total energy is decreased by enhanced dissipation in shallower water. This explanation is supported by the fact that rising T_{m1} periods coincide with steep depth gradients as present at the western beach of Sylt and the flats in front of the basin entrance.

3. In the NW20 case, refraction of propagating waves into the basin entrance is visible by varying mean wave directions. Since a high-tide situation with marginal tidal currents is displayed in the figure, the refraction is due to depth gradients.

Difference Fields. To indicate orders of magnitude of current effects on wave parameters and to show current-induced spatial patterns in wave-parameter fields of the Sylt-Rømø tidal basin, differences of the parameters significant wave height and T_{m1} period computed with current input and without are given for the E20 and NW20 cases at selected times in figures 4.3, 4.4, 4.5, and 4.6. For each case, one flood tide and one ebb tide situation was chosen. Times were selected to show extreme current influences on wave parameters. In the plots, positive differences appear as red contour lines, negative differences as blue lines. For wave heights, contour line stepping is 0.05 m, for periods 0.3 s. Arrows in the plots illustrate the current fields. Arrow lengths are proportional to current velocities, a length equivalent to the arrow grid step size corresponds to a velocity of 1 m/s.

Distinct features visible in the difference fields are pointed out in the following.

1. For flood tide in the E20 case, panel (a) of figure 4.3 shows that wave heights can increase through current influence by 10 cm to 15 cm. Effects are visible only at the basin entrance and at Højer Dyb. For both, opposing currents are present in the fetch development of waves to the locations. Effects on wave height in ebb tide situations are marginal, as can be seen in figure 4.4.

2. The T_{m1} periods are influenced more significantly by currents, see panels (b) of figures 4.3 and 4.4. For both flood and ebb the current-induced changes obviously depend on the local current component parallel or antiparallel to mean wave direction. Changes are larger for opposing currents: the T_{m1} increase is in maximum 0.9 s east of Højer Dyb (figure 4.3). Reduction of periods by parallel currents is always below 0.6 s (figure 4.4).

3. Current impacts on wave parameters are generally larger in the NW20 case. For flood tide, panel (a) of figure 4.5 shows a decrease of wave height of 15 cm at the basin entrance. In ebb-tide situation, wave height increases by 30 cm at the same location (figure 4.6), but significant increases are also visible within the basin up to Højer Dyb.

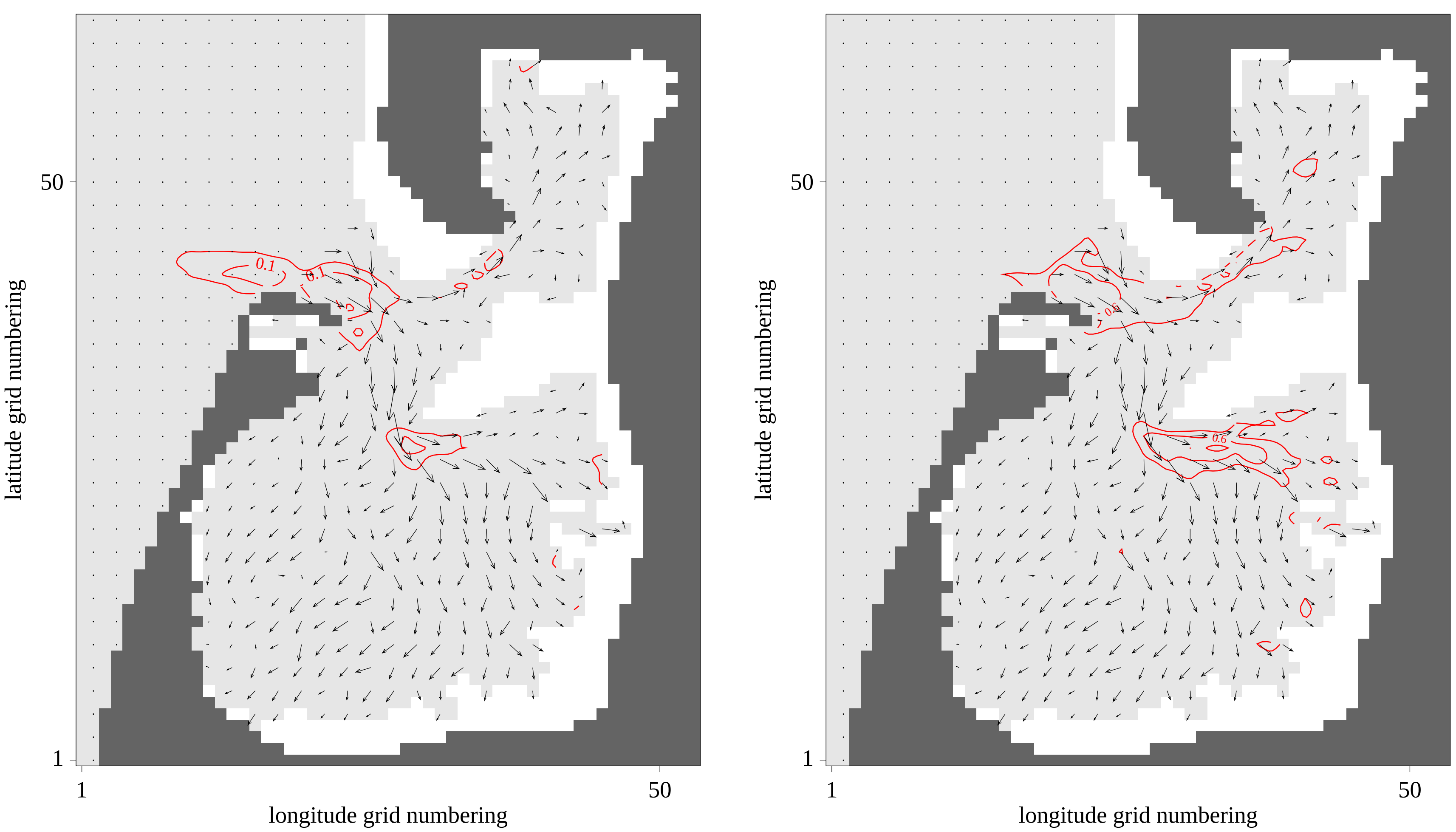

(a) H_S differences at flood tide

(b) T_{m1} differences at flood tide

Figure 4.3: Difference fields of significant wave height and T_{m1} period for the E20 case at a selected date 1 hour before high tide. Differences are model results obtained with current input minus model results without currents. Red contour lines indicate positive differences, blue lines negative differences. Step size of contour levels is ± 0.05 m for wave heights and ± 0.3 s for periods. Arrows indicate the current field.

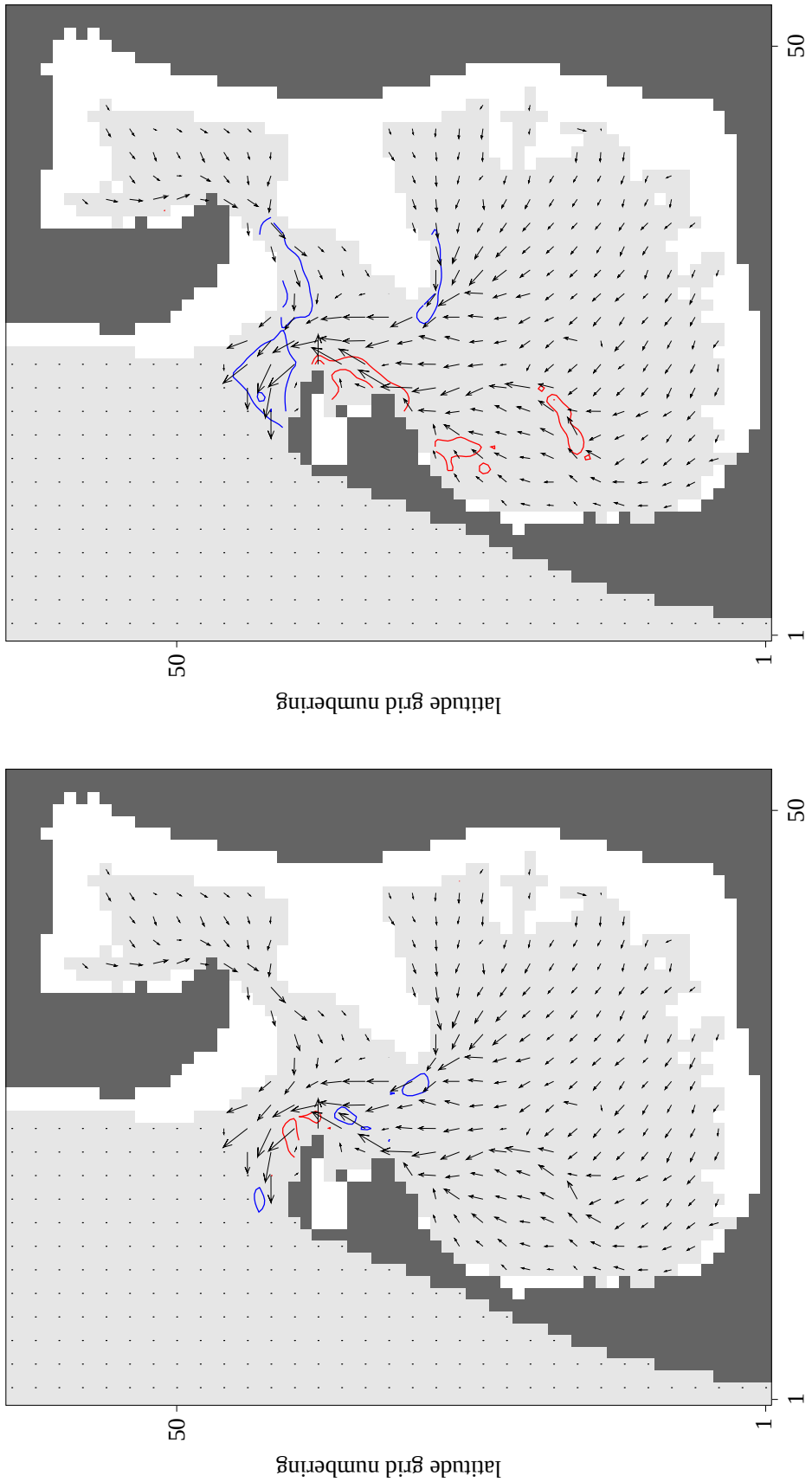

(a) H_S differences at ebb tide

(b) T_{m1} differences at ebb tide

Figure 4.4: Difference fields of significant wave height and T_{m1} period for the E20 case at a selected date 2 hours after high tide. Annotation as in figure 4.3.

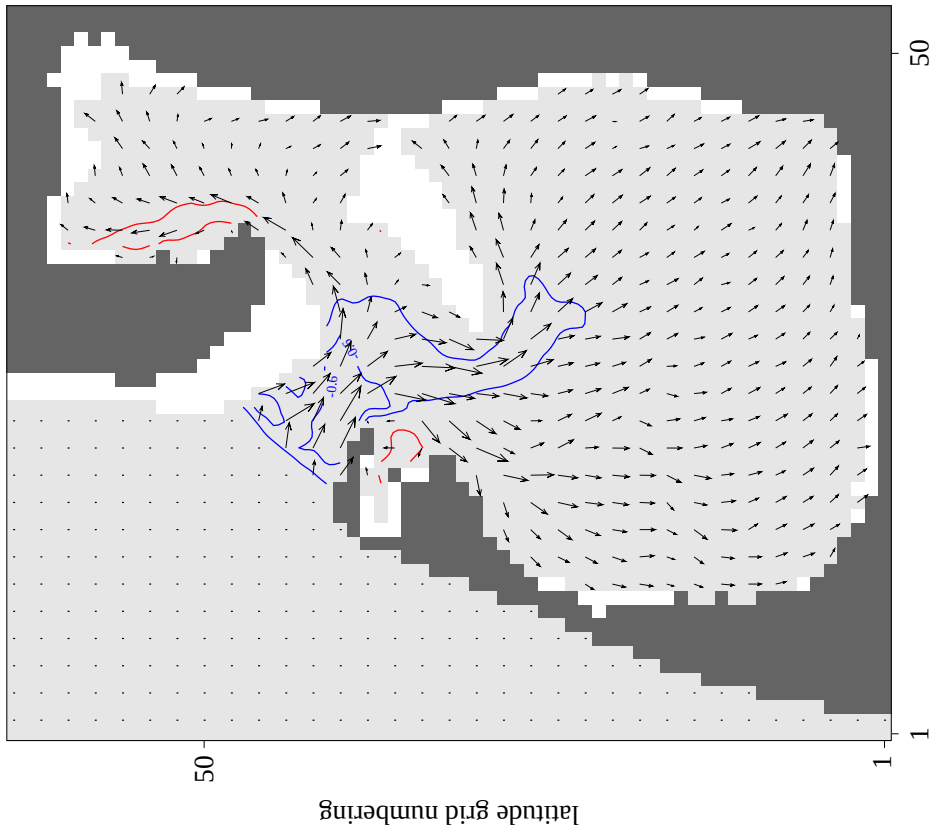

(a) H_S differences at flood tide

(b) T_{m1} differences at flood tide

Figure 4.5: Difference fields of significant wave height and T_{m1} period for the NW20 case at a selected date 1.5 hours before high tide. Annotation as in figure 4.3.

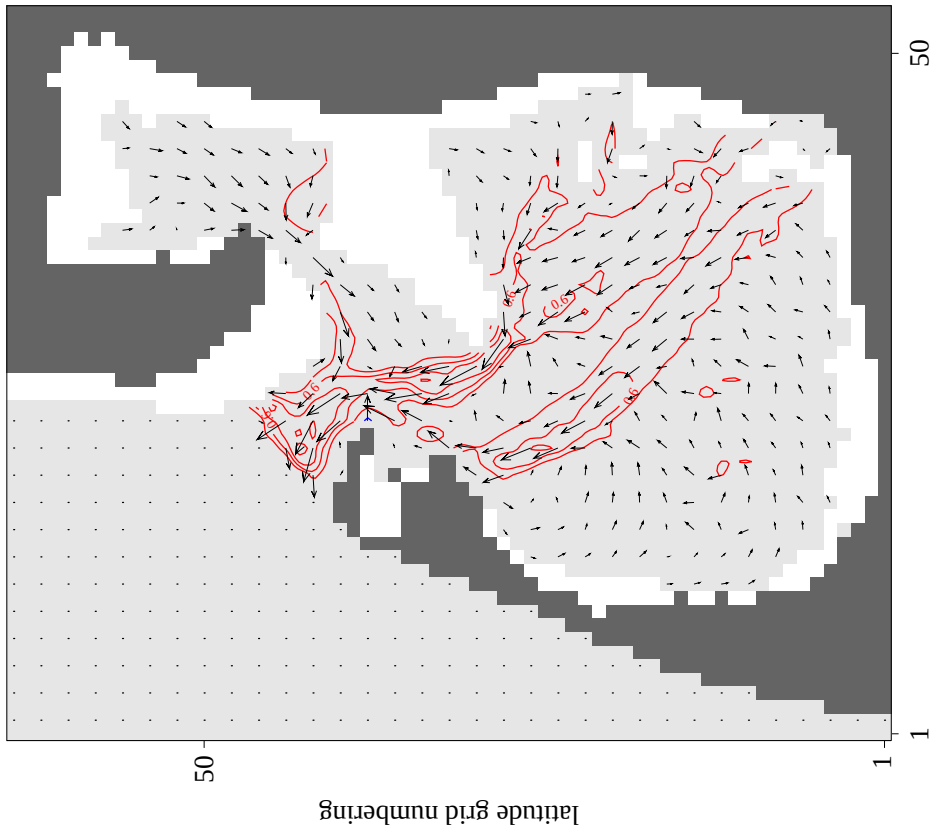

(a) H_S differences at ebb tide

(b) T_{m1} differences at ebb tide

Figure 4.6: Difference fields of significant wave height and T_{m1} period for the NW20 case at a selected date 2.5 hours before low tide. Annotation as in figure 4.3.

4. For T_{m1} periods in the NW20 case, panels (b) of figures 4.5 and 4.6 reveal the same quality of effects as for E20, but on a higher level. Current-induced increases are well above 1 s at the basin entrance and north of Højer Dyb.

Time Series. To indicate various tidal effects on wave parameters, time series of wave and current parameters at selected locations are presented in this paragraph. For each situation, significant wave heights and T_{m1} periods computed with current input and without will be given in the figures as thick and thin lines, respectively. To elucidate current-induced variations, current velocities, current directions (dotted), and mean wave directions (thick and thin lines) are plotted in addition. The length of the time series covers two tide cycles.

Characteristic features related to tidal impacts, in particular current impacts, on wave parameters visible in the time series are described in the following.

1. Figure 4.7 displays parameters at location P1 Lister Ley for the E20 case. A distinct tidal modulation of significant wave height and T_{m1} period is visible, but the current influence is rather small, as can be seen by similar curves for both model versions (with current input and without). The mean wave direction changes through current influence by 16 degrees at most. The tidal modulation of this parameter without currents is very small. For both flood and ebb tide, the mean wave direction is perpendicular to the current directions.

2. Parameters for the E20 case at location P3 Rømø Dyb in figure 4.8 also exhibit tidal modulations. The current impact on significant wave height is again negligible, but at this location there is a distinct variation of T_{m1} periods by currents. This variation exceeds in magnitude the tidal modulation without current influence. Current velocities are roughly equal for flood and ebb tide, viz. around 0.5 m/s at most, but T_{m1} variations are stronger for opposing currents than for currents travelling with mean wave directions. Mean wave directions are parallel and antiparallel to current directions, and show no tidal modulation. The same feature for the wave directions will be present in the rest of the figures.

3. At location Lister Tief for case E20, figure 4.9 shows negligible tidal modulation of wave parameters without current influence, but currents again cause a strong T_{m1} variation. At this location, a current impact on significant wave height is also present. It leads to an enhancement of wave heights for both flood and ebb tides.

4. Figure 4.10 gives time series for the NW20 case at location P1 Lister Ley. The time structure of currents is complicated. During the flood semi-cycle, current directions change continuously from southeast to west. Current velocities during flood also exhibit a structured time development. Wave parameters are modulated by tides, as was seen in the E20 case. But for this case a distinct, ebb-flood nonsymmetric current variation of wave heights is additionally present. Wave heights according to the model version with currents are larger during flood, during ebb no difference is visible. The current impact on T_{m1} follows the course of current-direction evolution.

5. Figure 4.11 gives an impressing example of orders of magnitude of current effects on both significant wave heights and T_{m1} periods at Lister Tief for the NW20 case. Tidal

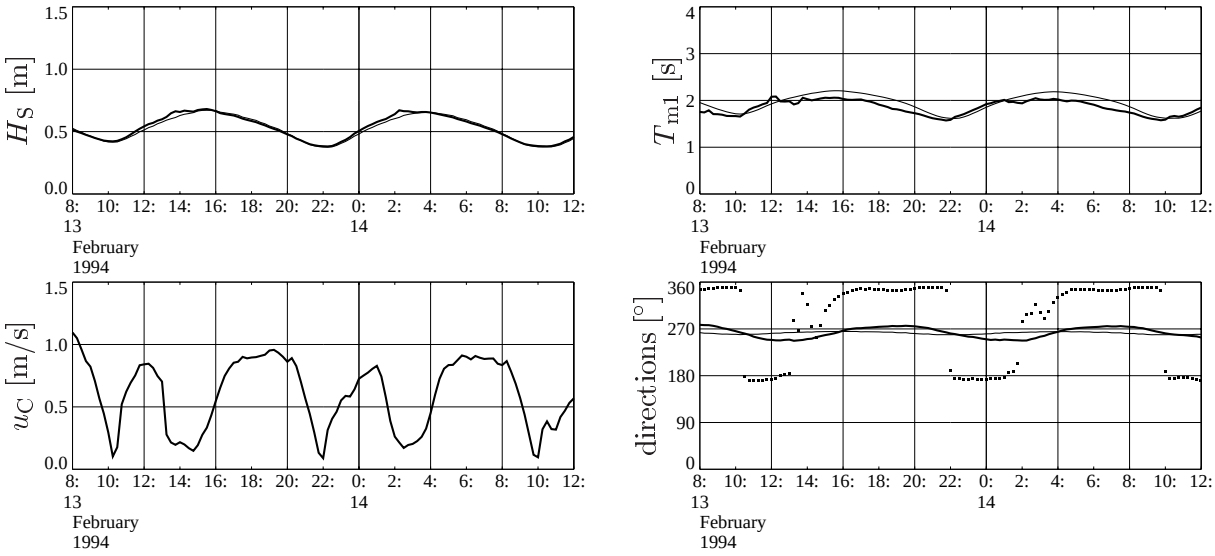

Figure 4.7: Time series of wave and current parameters for the E20 case at location P1. Wave parameters computed with current input are given as thick lines, without currents as thin lines. The current direction is given as dotted line (bottom right panel).

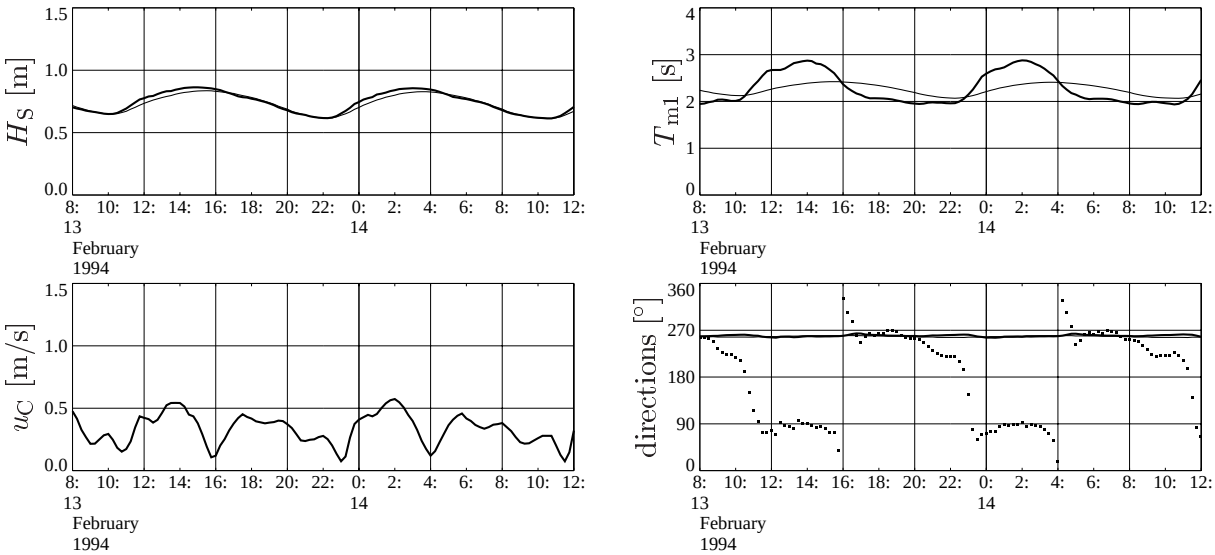

Figure 4.8: Time series of wave and current parameters for the E20 case at location P3. Line styles are as in figure 4.7.

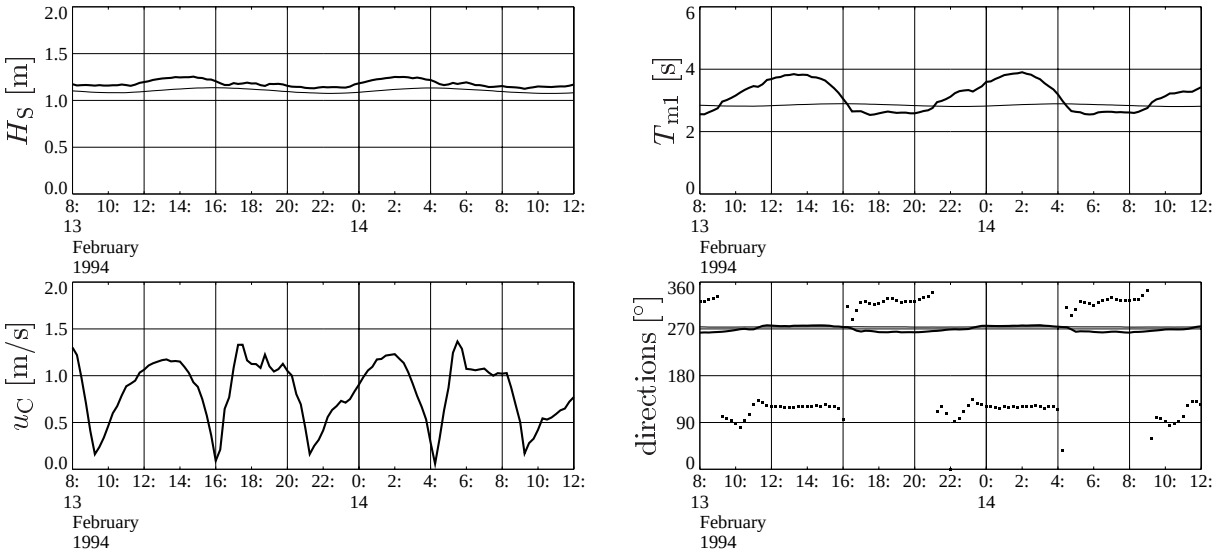

Figure 4.9: Time series of wave and current parameters for the E20 case at location Lister Tief. Line styles are as in figure 4.7.

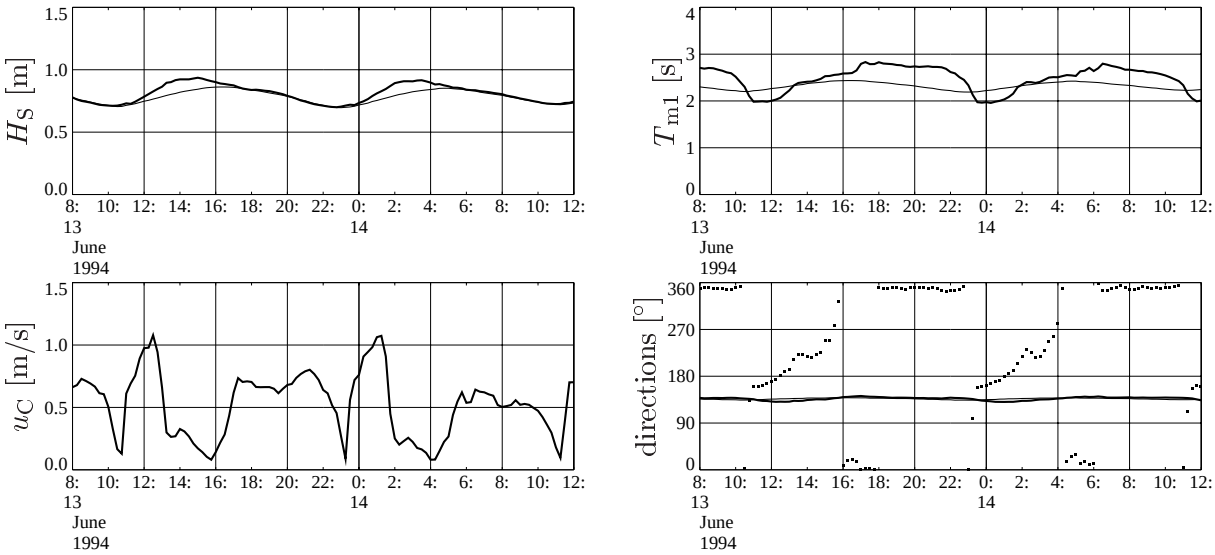

Figure 4.10: Time series of wave and current parameters for the NW20 case at location P1. Line styles are as in figure 4.7.

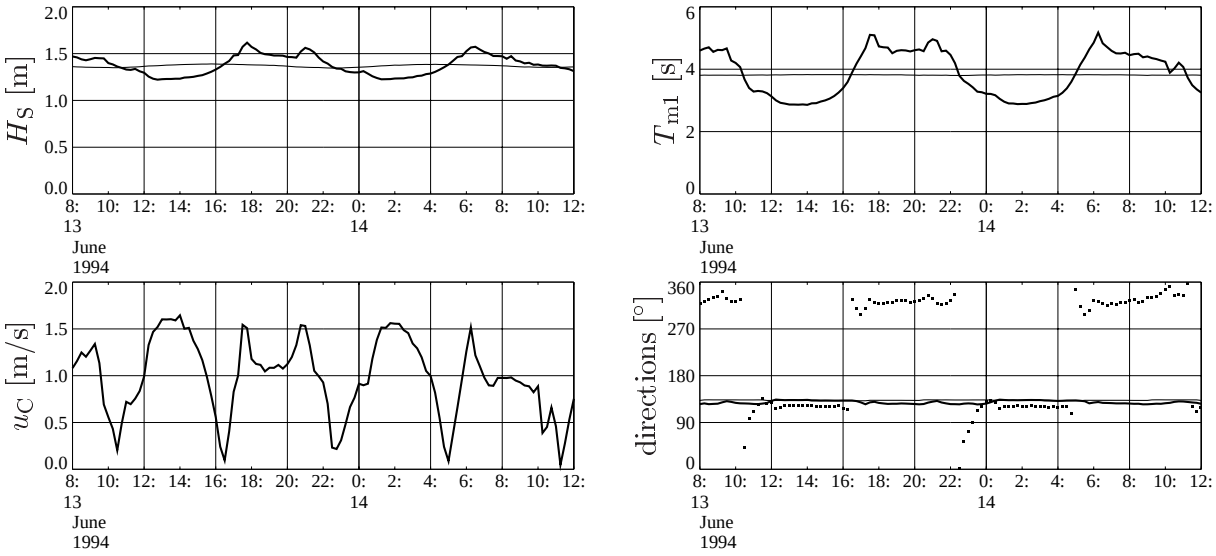

Figure 4.11: Time series of wave and current parameters for the NW20 case at location Lister Tief. Line styles are as in figure 4.7.

modulations apart from current effects are negligible, as was the case for E20 at this location. Current directions are roughly parallel and antiparallel to mean wave directions.

In all presented time series it has been obvious that current impacts appear in a systematical manner in the course of the tidal cycles: effects visible in the two presented cycles are roughly the same.

Two-dimensional Wave Spectra. To visualize principal current impacts on wave spectra, a selection of two-dimensional wave spectra for the NW20 case at four locations is given in figure 4.12. Left panels display results obtained with current input, right panels without. As for the time series, this enables a direct demonstration of current impacts. Contour-line stepping is given in logarithmic scale to enhance clarity of the plots.

At the chosen time, strong ebb currents were present. At all stations, current directions were opposed to wave directions in specific spectral bins. All spectra therefore exhibit indentations in the directions where opposing currents induced Doppler shifts to the energy in the spectral bins. At Lister Tief, this led to the formation of a bimodal spectrum. Spectral peaks are slightly shifted to lower frequencies. Spectra computed with currents are broader at all locations.

The influence of low-frequency wave energy from the open North Sea can be seen in the spectra. The level of low-frequency energy decreases with propagation into the inner basin. Spectra at locations are presented in figure 4.12 in the order of proceeding propagation into the basin to elucidate this feature. At P2 Højer Dyb, the low-frequency energy level is larger if currents are taken into account in the wave model. Residual low-frequency energy can even be seen at station P1 Lister Ley, but its level is insignificant. In general, low-frequency wave influence is small. Its distinct visibility in the plots is caused by the logarithmic contour-line stepping.

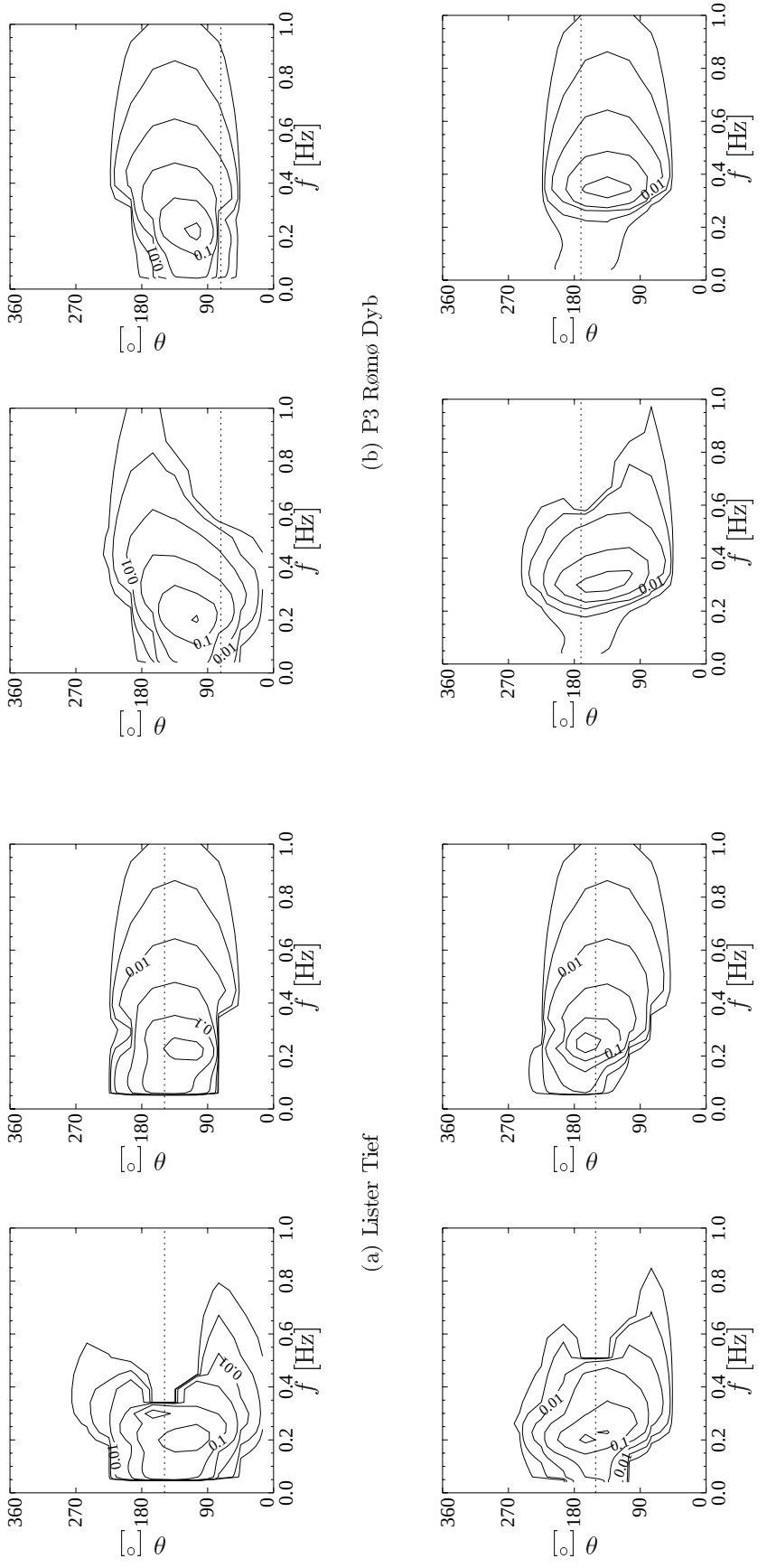

Figure 4.12: Two-dimensional wave spectra of case NW20 at a selected date (2.5 hours before low tide), at various locations. Left panels give spectra computed with currents, right panels without currents. Contour-line stepping is in logarithmic scale, steps are (1.E−3, 3.16E−3, 1.E−2, ...) m^2/Hz. Labels give spectral energy densities in m^2/Hz. Dotted lines indicate wave directions opposed to local current directions.

4.2.2 Discussion

Tidal Modulation of the Sea State. The given results of the two case studies have revealed tidal impacts on wave parameters in the Sylt-Rømø tidal basin. This has been expected from the discussion of principal effects of inhomogeneous and instationary external fields in section 2.3. It will be attempted here to attribute some of the indicated effects to individual mechanisms.

Water-depth-induced tidal modulations visible in the time series can result from depth-dependent source functions and varying fetches due to dry falling areas. At location Lister Tief, depth modulations are marginal due to a larger local water depth.

Current-induced effects appear in various qualities in the case-study results. Different effects will be discussed separately for the wave parameters T_{m1} period, significant wave height, and mean wave direction. Largest current-induced variations are visible for the T_{m1} periods. The principal mechanism responsible for these are local current-induced frequency shifts, i.e. Doppler shifts within the frequency-direction spectra. This can be deduced from the systematic dependence of shifts on current directions, visible in the parameter difference fields as well as in the time series. The two-dimensional spectra also demonstrate the effect via distinct energy shifts to lower frequencies in spectral direction bins opposed to current directions. The obvious fact that T_{m1} variations are larger in magnitude for opposing currents, see figure 4.8, is explained by the nonlinearity of the dispersion function (equation (2.13)). Nonlocal current effects on T_{m1} are also present, but are obscured by the dominant role of the Doppler shifts. Corresponding mechanisms have been discussed in section 2.3.

Current-induced variations of wave heights are in most cases less distinct than for T_{m1} periods, because the discussed Doppler shifts are energy conserving and thus do not affect significant wave height. In some cases, current modulation of wave heights is negligible, cf. figures 4.7 and 4.8. Variations of wave height at the basin entrance as visible in figures 4.6 and 4.11 are mainly caused by current shoaling of incoming waves from the open North Sea. This mechanism increases wave heights in rising gradients of opposing currents, and decreases wave heights in rising gradients of currents travelling along the waves. Advection of wave energy with currents is probably the cause for increases of wave height in flood tides of case NW20 at P1, cf. figure 4.10. An increase of effective fetch for opposing currents may enlarge wave heights at the basin entrance for case E20, as visible in difference fields for E20 plotted in figure 4.3. It becomes clear that various mechanisms can take leading impacts in current-induced variations of wave height. An impressing example of this is the wave-height time series at location Lister Tief for case E20, figure 4.9. Different leading mechanisms cause an unexpected increase of wave height by currents during both tidal semi-cycles.

Of all wave parameters shown in the time series, mean wave directions are least influenced by tidal currents. The only considerable impact is visible in the time series of case E20 at P1, figure 4.7. Mechanisms which can contribute to variation of mean wave direction are advection of wave energy by currents, current refraction, and an interplay of wind input and current-advected propagation leading to effective slanted-fetch conditions. A current impact depending on local properties, such as Doppler shifts, is only possible through wave blocking leading to an inversion of propagation direction for energy in certain spectral bins. The modulation of mean wave direction at P1 for the E20 case is probably caused by refraction: P1 is located at the

boundary of the roughly north-south-directed tidal channel Lister Ley. Considerable current gradients in east-west direction are thus likely to occur. These gradients have no impact on wave energy in bins aligned with the west-pointing mean wave direction. But energy in direction bins to the left and right of this are refracted, both into the same direction. The direction of the current gradient is consistent with a shift of mean wave direction into the current direction as observed in figure 4.7.

The Doppler shift mechanism has a leading impact in current-induced variation of spectral shape. It can explain the observed broadening, figure 4.12. Energy in directional bins opposed to the current is transferred to lower frequencies where it accumulates, thus raising the flanks of the spectrum in the vicinity of the peak. As for the T_{m1} periods, nonlocal mechanisms also contribute, but usually with minor significance.

Both in the parameter difference fields and the time series, it is obvious that current-induced changes in wave parameters are larger for the NW20 case than for the E20 case. Different behaviour for the two case studies was expected since relative angles of current directions and mean wave directions are different for the two cases. It is summarized that significance of current impacts in relation to water-depth impacts varies with location, meteorological situation, and regarded wave parameter. A leading impact of currents on tidal modulations is possible at all regarded locations. The case studies show that neither tidal currents nor tidal depth variations can be classified as dominant mechanism for tidal modulation of the sea state regardless of the specific situation.

Relation to Previous Studies. The K-model was designed for applications to coastal environments with tidal influence. The ability to take into account instationary external fields allows for investigations leading to results as presented in the preceding subsection. Other available spectral wave models are not able to reproduce these results. HYPAS cannot take into account current influence on waves at all. WAM cy. 4 can be applied only in quasi-stationary mode, and in larger-scale applications. SWAN can be used only in stationary mode. This is inadequate for applications to the Sylt-Rømø tidal basin, as was shown in section 4.1. Inofficial extended versions of SWAN and WAM are in progress, but these are yet to be tested and published.

The discussed current effects on wind waves in the Sylt-Rømø tidal basin can be compared with results from a similar study in a Dutch coastal environment (the Friesche Zeegat) reported by Ris (1997). To detect current effects Ris similarly compared wave-model results obtained with current input and without. The simulations were carried out with SWAN in stationary mode. The stationary treatment is justified in the Friesche Zeegat application, since emphasis was set in this study on the analysis of approaching waves from the open sea into the tidal inlets (cf. the remarks on stationarity in section 4.1). The quality of current impacts on wave parameters reported by Ris is similar to the results described in this thesis: a major impact on T_{m1} periods was reported, whereas significant wave heights were influenced less distinctly. Variation of mean wave direction was termed significant by Ris, but changes are in the same order of magnitude as reported in this thesis. Results of the two studies are thus generally consistent. Tidal influence on significant wave height in the Sylt-Rømø tidal basin was investigated with a coastal wave model also by Winkel (1994), but only impacts of varying water depths were analysed.

4.2.3 Conclusions

Based on the presented model results and discussion, the following conclusions can be drawn from the E20 and NW20 wave-modelling case studies in the Sylt-Rømø tidal basin.

1. The K-model can be used successfully for coupled investigations of coastal environments with tidal influence.

2. Two case studies for different prescribed wind situations have revealed considerable and systematic tide, in particular tidal-current impacts on integrated wave parameters and spectral shape of wind waves in the Sylt-Rømø tidal basin.

3. Orders of magnitude of wave-parameter modulations through tidal currents can be of equal size as depth-induced modulations at locations both at the basin entrance and the inner parts of the basin. Both effects are equally important for wind wave modelling in coastal environments.

4. By analysis of model results, current-induced changes of wave parameters have been attributed to leading mechanisms in selected cases. However, a multitude of mechanisms can have an influence, cf. subsection 2.3.6. The net resultant of their interplay can only be assessed by analysis with a wave model which takes into account instationary water-level and current fields.

4.3 Hindcast April 1997

The April 1997 hindcast of wind waves in the Sylt-Rømø tidal basin has been performed to validate the K-model for applications in small-scale tidal systems. In addition, statistical validation of the model runs with currents and without will give an objective quantitative assessment of current significance at the field-station locations.

4.3.1 Meteorological Situation and Measurements

The period April 1997 was chosen for a hindcast experiment with the K-model because the meteorological situation was dominated by strong winds and thus promised interesting sea-state situations in the Sylt-Rømø tidal basin. Furthermore, measurement data have been available for this period and can be used for comparison and validation.

Meteorological Situation. The surface-wind situation in the Sylt-Rømø tidal basin for the month of April 1997 is illustrated in figure 4.13. The figure displays measured ten-minute-average wind velocities and directions at pile P3 Rømø Dyb. Six-hourly analysed winds according to the German Weather Services (DWD) Europe model are given for comparison. During April 1997, measured wind speeds at ten meters height exceeded 15 m/s on six days. On 14 days, measured wind velocities at P3 were above 10 m/s. Major peaks occured on April 11th, 14th, and 24th. The first two were above 20 m/s. Wind speeds above 10 m/s came from directions between west and north in most cases. The peak on April 24th had a southwest direction.

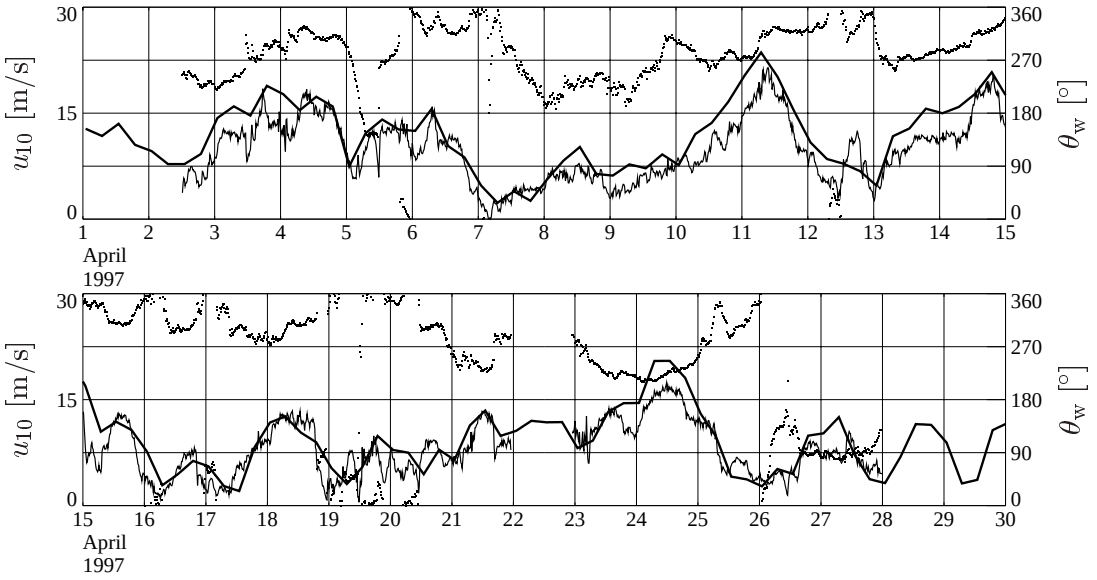

Figure 4.13: Measured wind velocities at pile P3 Rømø Dyb (thin lines). For comparison, DWD six-hourly analysed wind velocities are given as thick lines. Dotted data are measured wind directions. Directions are given with respect to the right-side y-axis, in meteorological convention (wind coming from direction).

From wind directions in the Sylt-Rømø tidal basin in the considered period of time it becomes clear that boundary spectra must be provided for wave modelling to capture the effect of incoming waves from the open North Sea. From a comparison of the time variability of the measured wind-velocity time series with the DWD model winds it is obvious that higher-resolution winds are needed for the wave modelling than the DWD Europe model can provide. Therefore, measured time series of winds were processed to input wind fields for the K-model, as described above.

Wave Measurements Available. Field data from the Sylt-Rømø tidal basin were compiled by GKSS within PROMISE in the years of 1996 and 1997. Wind, wave, and current measurements (plus other parameters not needed in this study) are available for the month of April 1997 at the two measurement piles P1 Lister Ley and P3 Rømø Dyb. One-dimensional wave-energy spectra were obtained from floater time series available in ten-minute intervals. From the spectra, wave height and different wave-period parameters were computed via integration. The quality of wave-height measurements at P3 Rømø Dyb can be cross-checked by comparing with a nearby wave-rider buouy. The wave-rider data are available in one-hour intervals. Throughout the month of April 1997, the two independent wave-height measurements at P3 agree very well, cf. figure 4.15. This supports the credibility of wave height measurements. The floater wave heights and T_{m1} periods at both stations roughly fulfill the energy-frequency relations following from a TMA spectral shape. This gives a first quality check for the period measurements. The periods obtained from the wave-rider-buouy data agree well with the floater data from P3 except for situations with wave heights below 0.2 m. Here, the wave-rider periods are generally larger than the floater periods, cf. figure 4.15.

4.3.2 Model Results

In the April 1997 hindcast experiment, comparison with field data is a major objective. For this reason, the presentation of results will be confined to selected wave- and current-parameter time series and validation statistics at the two field stations.

Selected Time Series. Time series of wave and current parameters are given for the period 10th April to 16th April 1997. The wind speed maximum of the month of April occurred in this period, cf. figure 4.13. Wind directions were west to north, at the wind-velocity peak northwest.

Figure 4.14 displays significant wave height, T_{m1} period, current velocity, and current and mean wave directions at station P1 Lister Ley. For the wave parameters in the top two panels, model results with current input (red lines) can be compared with model results without current input (blue lines) and floater measurements (green lines). In the third panel, wave-model input current velocities (red line) and measured current velocities (black line) are presented. Analogous colouring has been used for the current directions in panel four. Mean wave directions modelled with current input are given in addition (black dots).

The quality of current input into the wave model at P1 can be assessed from panels three and four of figure 4.14. The TRIM3D model was successfully validated in Sylt-Rømø tidal basin applications by Behrens et al. (1997). Here, the quality of input current fields for the wave model can be seen. Note that these currents are postprocessed results from the current model which have been reduced in spatial resolution from 100 m to the 500 m resolution of the wave-model grid. The model current velocity agrees well with measurements in the ebb semi-cycles of the tide. The structure of the measured flood semi-cycle – a short peak followed by a sharp decline in current velocity – is not captured well in the model input current field. Model current directions are reproduced reasonably well in the wave model input.

Model results for significant wave height at P1 agree well with floater measurements at the wind speed peaks, but are high for moderate wind speeds in between peaks. For low wind speeds, agreement of model and measurement is better. A quantitative analysis of performance will be given via validation statistics in the next paragraph. Differences of significant wave heights from model runs with current input and without are small at P1. The model with currents is systematically higher for flood tides. At ebbing tides, no difference can be seen. This qualitative result was already obtained in the NW20 case study at location P1. Differences in significant wave height within the displayed period are at most 7 cm, or 9 per cent.

Model results for T_{m1} periods agree well with measurements. The influence of currents on the wave-model results is more obvious for the T_{m1} periods. The tidal modulation of the measured periods at P1 is reproduced remarkably well by the wave model with current input. Agreement with measurements improves significantly by inclusion of currents into wave modelling. If currents are accounted for, the T_{m1} periods can change by as much as 0.5 s at location P1. Model mean wave directions have been added to panel four to show that current effects on T_{m1} periods are largest for current directions parallel and antiparallel to wave directions, as was discussed above for the case studies.

Figure 4.15 displays significant wave height, T_{m1} period, current velocity, and current and mean wave directions at station P3 Rømø Dyb. In the first two panels, results from wave-rider measurements appear in addition (black lines).

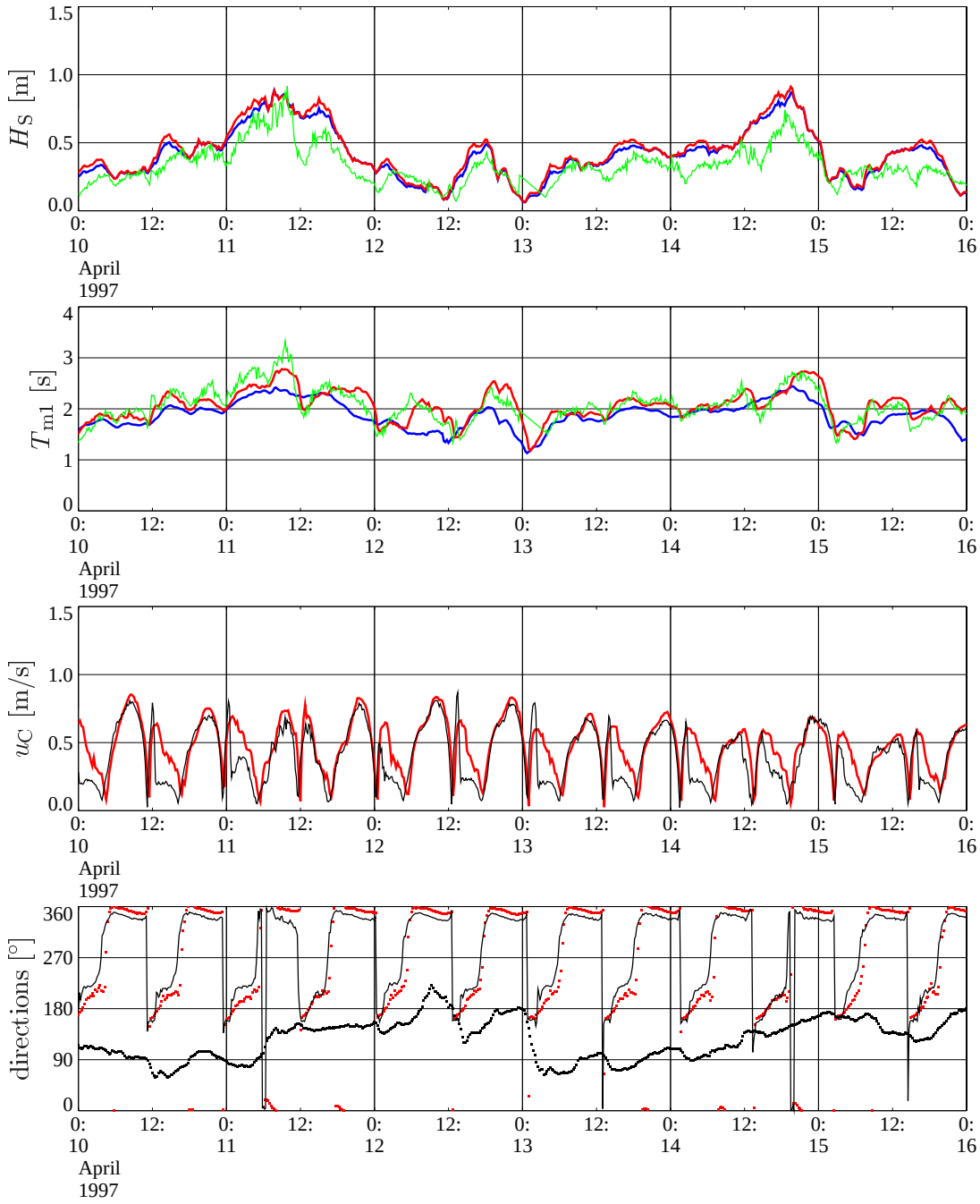

Figure 4.14: Time series of wave and current parameters for a selected period of the April 1997 hindcast at location P1 Lister Ley. The top two panels display significant wave height and T_{m1} period. Red lines are model results with current input, blue lines model results without. Green lines are floater measurements. The third panel displays model input current velocity as red line, measured current velocity as black line. In the bottom panel, model input current directions appear as red dotted, measured current directions are black lines. Modelled mean wave directions are displayed as black dotted.

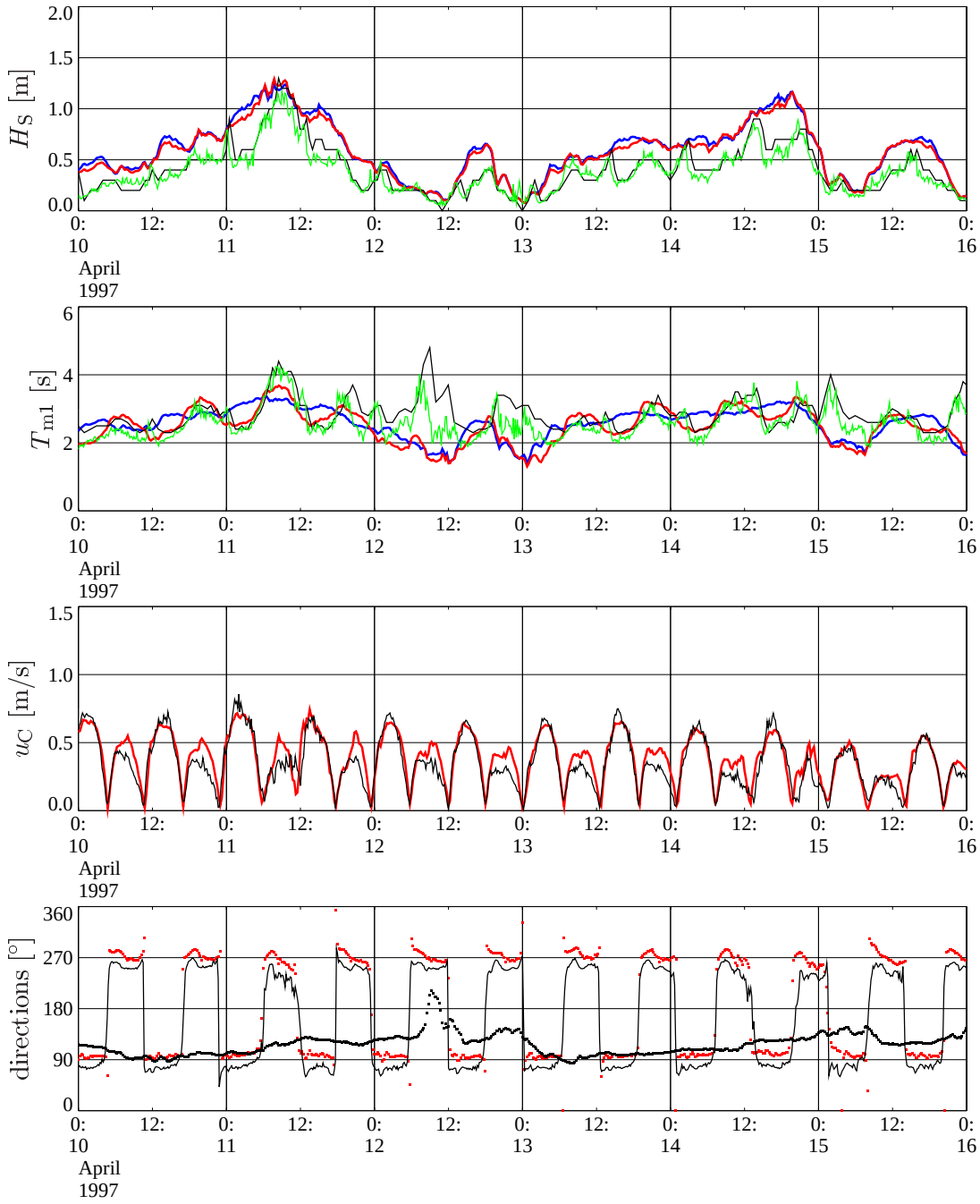

Figure 4.15: Time series of wave and current parameters for a selected period of the April 1997 hindcast at location P3 Rømø Dyb. The top two panels display significant wave height and T_{m1} period. Red lines are model results with current input, blue lines model results without. Green lines are floater measurements, black lines wave-rider measurements. The third panel displays model input current velocity as red line, measured current velocity as black line. In the bottom panel, model input current directions appear as red dotted, measured current directions are black lines. Modelled mean wave directions are displayed as black dotted.

The quality of current input to the wave model at P3 is comparable to P1. For current velocities, agreement with measurements is good in the flood semi-cycle, whereas the current magnitudes are too large at ebb tides. The directions are captured fairly well.

The overall picture of wave-model results for wave heights is similar to P1. At measured peaks, the wave heights are reproduced well but generally a positive bias can be expected. Note that throughout the measured wave-height time series a periodic modulation with semi-tidal period exists. The measured wave heights exhibit local maxima shortly after high tide and low tide, i.e. after current-velocity minima independent of current direction. This is particularly obvious in the period 13th to 15th April. This modulation of wave heights is not reproduced by the wave model in either version. The influence of currents on modelled wave heights is similarly small as seen at location P1. At P3, a qualitatively opposite effect occurs: at flood tides, wave heights computed with current input are systematically lower than computed without. At ebbing tides, no differences can been seen in the results. As for P1, this behaviour at location P3 was observed already in the NW20 case study. Differences in modelled wave heights from the two model verions are in maximum 10 cm, or 10 per cent.

The magnitudes of measured T_{m1} periods are reproduced fairly well by both model versions except for low wind situations with wave heights below 20 cm. Here, measured T_{m1} periods increase to roughly 5 s, see e.g. 06:00 to 12:00 12th April. The models do not reproduce this rise of periods. It is likely that the observed rise of periods is not artificial even though both measuring devices disagree in magnitude of the effect. It can be attributed to influence of incoming residual wave energy from the open sea which becomes noticeable in cases where the wind sea is low. This wave energy is captured inadequately in the wave model, as will be discussed in the next subsection. At moderate and higher wind speeds, the wave-model version with current inclusion reproduces well the tidal modulation of measured periods, as was the case for location P1. Differences in both model versions can be well above 0.5 s at P3.

Validation Statistics. Validation of wave-model results against measurements from floaters at locations P1 and P3 and wave rider at location P3 are given in tables 4.1 and 4.2. The tables display statistics for the wave parameters significant wave height and T_{m1} period, computed with current input and without. This enables a quantitative and objective assessment of current influences on wind waves as seen at the two locations. For the statistics, wave-modelling results from the entire hindcast period ranging from 12:00 2nd April to 0:00 28th April 1997 have been used. The hindcast period was fixed by the availability of measurements. The fairly dense field data set ensures statistical relevance since it allows for consideration of roughly 2000 data points for comparison with floater measurements and roughly 750 data points from wave-rider measurements.

Table 4.1 contains the wave height statistics. Statistical parameters of results from the two model versions are similar. This has been expected from the small current influence as visible in the time series. Biases are positive at all locations, but reasonably small: 5 to 7 cm at P1 and 12 cm at P3 for both measuring devices. Root-mean-square (rms) errrors range from 10 cm to less than 20 cm. Resulting from low mean values of measurements, the scatter indices look fairly high with values from 30 to 40. The reduction of variance is always positive, ranging from roughly 0.2 to 0.6 for different stations and model versions.

Table 4.1: Validation statistics for significant wave height for three measurement stations within the Sylt-Rømø tidal basin. Statistics for the K-model with currents taken into account and without. See appendix A.4 for definition of statistical parameters.

Location & field method	Number of points	Mean of measurements [m]	Stand. dev. of measurements [m]	Currents in model?	Stand. dev. of model [m]	Bias [m]	rms error [m]	Scatter index	Reduction of variance
P1 floater	2061	0.31	0.15	yes	0.19	0.07	0.11	28	0.44
				no	0.18	0.05	0.10	27	0.58
P3 floater	2065	0.32	0.20	yes	0.27	0.11	0.17	39	0.31
				no	0.27	0.12	0.18	44	0.19
P3 waverider	757	0.38	0.25	yes	0.28	0.12	0.17	30	0.56
				no	0.29	0.12	0.18	33	0.50

Table 4.2: Validation statistics for T_{m1} period, annotation as table 4.1.

Location & field method	Number of points	Mean of measurements [s]	Stand. dev. of measurements [s]	Currents in model?	Stand. dev. of model [s]	Bias [s]	rms error [s]	Scatter index	Reduction of variance
P1 floater	2061	1.99	0.34	yes	0.35	−0.04	0.20	10	0.66
				no	0.30	−0.19	0.28	11	0.32
P3 floater	2065	2.47	0.51	yes	0.56	−0.26	0.65	24	−0.59
				no	0.54	−0.24	0.65	24	−0.59
P3 waverider	757	2.81	0.52	yes	0.58	−0.48	0.86	25	−1.78
				no	0.55	−0.46	0.86	26	−1.78
P3 floater ($H_S > 0.2$ m)	1354	2.53	0.46	yes	0.45	−0.06	0.38	15	0.32
				no	0.44	−0.06	0.46	18	0.00
P3 waverider ($H_S > 0.2$ m)	478	2.82	0.42	yes	0.40	−0.18	0.37	11	0.25
				no	0.34	−0.15	0.44	15	−0.09

Table 4.2 shows statistics for the T_{m1} periods. Since current effects have been more obvious in the time series of this parameter, one can expect to see differences in the statistics for the two model versions. For location P1, a clear improvement of hindcast quality through consideration of current influences on waves is expressed by a decrease of magnitude of bias, decrease of root mean square error, and doubling of reduction of variance to a value of 0.66. The internal variability of the floater time series includes tidal modulation and is expressed by the standard deviation of measurements. Its value is reproduced by the wave model with current input, but is low for the model version without current input. The statistical results give quantitative evidence that tidal modulation of T_{m1} period is hindcasted better by a model which takes into account current effects.

The validation statistics for T_{m1} periods against floater and wave-rider measurements at P3 reflect the bad performance of period hindcast in cases of low wind waves with present residual low-frequency wave energy. The rms errors are large, they exceed the standard deviations of measurements and thus lead to negative hindcast skills. To show better performance in the presence of relevant wind waves, the table gives in addition statistics for data points with corresponding wave heights above 20 cm. Now, hindcast skill of the model with currents is positive and, as at P1, substantially better than for the model without currents.

4.3.3 Discussion

Selected time series of wave parameters as hindcasted by the wave-model versions with current input and without have revealed a similar quality of current effects as was found in the NW20 case study. In particular, changes of wave height by currents occured in equivalent tidal cycles, with equal signs and orders of magnitude. In the period chosen for the presented hindcast time series, wind directions were west to north. The directions thus match the wind situation prescribed for the NW20 case. This shows that qualitative effects in the basin depend on wind direction and are realistically reproduced by the case studies. The cases can be supplemented by further wind-direction and wind-velocity situations to obtain an atlas which can be used to estimate the sea state in the basin for any weather situation. This will complement the current and water-level atlas provided for the Sylt-Rømø tidal basin by Behrens et al. (1997).

The quantification of current impacts on wave parameters indicates a significance of current influences on the sea state in any coastal system characterized by similar tidal ranges and currents, and dominance of locally generated wind waves over incoming low-frequency waves.

The validation statistics of model results against field data allow an assessment of model quality. Statistical validation is standard in ocean wave modelling, see e.g. SWIM (1985). For small-scale coastal applications, however, validation studies are sparse in literature. For this reason, values for statistical parameters from this thesis cannot be compared with performance of other models. Ris (1997) reports statistics of SWAN results against measurements in two coastal applications. But since the stationary SWAN version was used in this study, the statistics have a different meaning: samples are comparisons of modelled and measured data obtained from various stations at the same point in time. Wolf et al. (1998) present validation statistics of an application of HYPAS to a small-scale coastal system adjacent to the Baltic Sea (the Odra lagoon). In this system tidal influences are negligible. This justifies the use of HYPAS in which

current effects cannot be considered. It is concluded that the validation study of a wave model in a small-scale system with tidal influence as presented in this thesis has not been reported before. Orders of magnitude of biases and root-mean-square errors are small in comparison to ocean-wave-model statistics, but this is obvious since the magnitudes of the parameters themselves are also much smaller. Scatter indices as reported in this study are large in comparison to ocean-wave-model statistics. But this results from very low mean values of measurements as obtained during the hindcast period. A parameter for assessment of hindcasting and forecasting skill is reduction of variance. Since the obtained values are positive except for wave periods at station P3, the model performance is valued here as satisfactory. This is a major step forward, since long hindcasts of waves in small-scale tidal environments have not been reported before. In this study, tidal-current-induced modulations of wave-period parameters have been reproduced for the first time in quantitative manner. This has led to a distinct improvement of hindcast skill.

The negative reduction-of-variance values for T_{m1} statistics at station P3 are unsatisfactory. The performed filtering of data points connected to low wave heights is questionable in a thorough statistical validation. But it shows that hindcast performance of wave periods is significantly decreased only in situations where wind waves are negligible and residual low-frequency energy from the open sea pushes up the period parameters. This effect is not captured well in the wave model.

Limitations of the Model System. In this paragraph, limitations of the model system and potential error sources will be indicated and discussed.

1. One reason for insufficient hindcast of incoming low-frequency wave energy at station P3 is the fact that output frequency-direction spectra from the K-model have been limited to a frequency axis ranging from 0.1 Hz to 1.0 Hz in the hindcast experiment. In the NW20 case, the frequency axis was extended downwards to 0.04 Hz. Spectra at P3 from this case study have been shown to exhibit parts with frequencies down to 0.04 Hz. If these are cut off at 0.1 Hz, T_{m1} periods will be low in cases where low-frequency wave energy is significant in comparison with the locally generated wind-sea part of the spectrum. But even if this is repaired, good hindcast of periods in these cases cannot be expected: for very low wave heights, period parameters defined by spectral moments are erroneous because division by total energy (zeroth moment) is involved. Regarding this aspect it is concluded that the K-model gives satisfactory hindcast performance in coastal systems which are wind-sea dominated. The Sylt-Rømø tidal basin is such a system because low-frequency wave effects only emerge in calm situations with absent local wind sea and do not influence wave heights in a significant manner.

2. The wave-model grid resolution was coarser than the current-model grid resolution in the simulations described in this chapter. This can lead to locally unrealistic current input into the wave model. Hindcast quality for wave parameters depending on local currents, e.g. T_{m1} periods, can be reduced by this. There is no general necessity to apply the wave model in equal resolution as the current model, but it must be ensured that the wave-model resolution is fine enough to capture the spatial structure of the current field. This was the case in the hindcast presented in this thesis: wave-model input currents agreed

well with measured currents. This enabled a feasible wave-model setup.

3. An extension of current modelling to an area outside the basin is expensive. It is not clear how, in this case, boundary values can be provided as conveniently and accurately as by measured tidal gauges at the basin entrance. Since in the present current-modelling approach water-level variations and current fields for wave-model input are cut off at the basin entrance, unrealistic effects on the waves in this area can be caused by artificial gradients. The gradients give rise to incorrect current refraction. Current shoaling and local current effects are not affected, however. It was shown that these two mechanisms have a leading impact on the waves in the basin entrance region. Therefore, the net current influence in this region is expected to be captured reasonably well. A validation of this statement is not possible because of the lack of field data from this area.

4. In the processing of input wind fields for the wave model from measured winds, effects of atmospheric stratification and of sea-state dependence of the roughness parameter were not considered. Further errors can be caused by orographic effects leading to a spatial structure of the wind field over the Sylt-Rømø tidal basin. Such effects have been pointed out e.g. by Rudolph (1993). They are not considered in the present modelling approach, since winds from one location have been homogeneously extended to the entire basin. Future studies should address this question by inclusion of mesoscale atmospheric modelling into the model system for the basin. However, measurements from further field stations would be required to prove the significance of this effect by validation against measurements.

5. Input current fields for the wave model were two-dimensional. In principal, the vertical structure of the current field can play a role in current influence on the waves. To take this into account, the two-dimensional current must be replaced by a weighted vertical mean depending on wave vector (Stewart et al. 1974, Young et al. 1985a). Two problems arise in this context. First, more expensive three-dimensional current modelling would be required. This would question the feasibility of the coupled modelling approach for the basin. Second, it is not clear in total how the vertical structure of the current field affects the wave spectrum. The relevance of this effect is also questionable. For these reasons, a close investigation was outside the scope of the present study.

6. A semi-tidal modulation of wave heights was measured at location P3. Wave heights showed periodical maxima in the vicinity of current-velocity minima, independent of current direction and water depth. This feature can thus be attributed to an influence of current modulus on wave height. It was not observed at station P1. The effect is not resolved in the wave model and is therefore discussed within the error analysis. One explanation is an unrecognized influence of current modulus in the source functions. For instance, the wind input can be altered by a decrease of surface roughness in the presence of currents, thus leading to a decrease of momentum flux. Bottom friction dissipation is influenced by the current modulus according to theories described in Hasselmann et al. (1968) and Hasselmann et al. (1973). Finally, wave turbulence interaction can be enhanced by higher turbulence levels in the presence of currents. This effect can easily be

parametrized in the K-model by a current-modulus dependence of the eddy-viscosity entering the dissipation constant, cf. section 2.3. The analysis is outside the scope of the present study, but it is recommended for future work.

4.3.4 Conclusions

Based on the presented wave-modelling results and discussion the following conclusions can be drawn from the April 1997 hindcast of sea state in the Sylt-Rømø tidal basin.

1. Wave modelling in coastal systems is a coupled problem. Current modelling is essential for providing time-varying water-level fields and spatial patterns of dry points. Time variability of measured surface winds on a ten-minute scale prohibit the utilization of large-scale wind fields as driving fields for the sea-state modelling. The large effort needed for external fields stresses the importance of efficient wave modelling which focuses on essential processes.

2. The spectral wave model with nonlinear dissipation under investigation in this thesis has been successfully validated in a hindcast experiment of waves in the Sylt-Rømø tidal basin. A comparable performance can be expected in applications of the model to similar coastal systems dominated by tidal currents and locally generated wind waves.

3. A substantial improvement of wave period hindcast in the Sylt-Rømø tidal basin by inclusion of tidal-current effects was demonstrated and proved in quantitative and objective manner by validation against field data. An enhancement of hindcast skill (reduction of variance) from 0.32 to 0.66 was achieved at station P1 Lister Ley. A similar improvement in skill was present at P3 Rømø Dyb, but at this station uncaptured effects of incoming low-frequency wave energy from the open sea reduced the general level of hindcast performance.

4. Current effects on significant wave height at the two field stations are insignificant in most cases. Therefore, an improvement of hindcast quality for this parameter could not be proved by validation statistics against measurements. But current impacts on wave height can be substantial in special cases at other locations. Extreme wave height variations during the hindcast were 30 per cent, extreme T_{m1} period variations up to 50 per cent. For this reason, inclusion of current effects into wave hindcasting and forecasting in the Sylt-Rømø tidal basin and similar coastal environments can be inevitable. However, depending on individual objectives of particular sea-state investigations it may be possible to neglect current effects in special cases. A decision in this question can be supported by pre-investigational case studies similar to the ones presented in the preceding subsection.

5 Concluding Remarks

In this study the conceptual idea of spectral wave modelling with nonlinear dissipation was investigated. To this end a wave model based on this idea was developed, analysed, and applied to a coastal system. The wave model has been alternatively termed K-model. Analytical treatment and numerical experiments of academic cases revealed general features and indicated the capabilities of the modelling approach. Utilization of the model in investigations of wind waves in a small-scale coastal environment with tidal influence demonstrated the applicability of the wave model and led to general conclusions on the dynamical behaviour of such systems. The concluding chapter of this thesis contains an overall summary of results from the individual parts of the investigation. In a general discussion it will be assessed to which degree these results can contribute towards realizing the general aim of the study which was proposed in the introduction, chapter 1. Future work to extend and apply the outcome of the study will be recommended in the course of this discussion.

Summary of Conclusions. The investigations on spectral wave modelling with nonlinear dissipation which were described in chapters 2, 3, and 4 of this thesis led to the following general conclusions:

1. New aspects in the conceptual idea of wave modelling with nonlinear dissipation have been discussed. A nonlinear dissipation source function is formally consistent with a general nonlinear form for dissipation source functions in spectral models. Furthermore, the nature of the considered process, i.e. wave dissipation by interaction with oceanic turbulence, gives a physical justification of the source function. For applications of spectral wave modelling in small-scale inhomogeneous systems, it can be justified to neglect a state-of-the-art source function accounting for nonlinear energy transfer due to quadruplet interactions of ocean waves. The use of action-density spectra in wave-number-direction space as prognostic fields is well suited for wave modelling of inhomogeneous, instationary systems.

2. Principal features and capabilities of a spectral wave model with nonlinear dissipation have been made apparent by an analysis of the model dynamical equation and computations of academic test cases. In contrast to many existing spectral wave models, the K-model reproduces prognostically a spectral tail which is consistent with most recent theory. Well-known qualitative features of wave growth are reproduced by the K-model. Fetch-limited growth curves for total energy and peak frequency can be calibrated to empirical laws according to Kahma et al. (1992) or alternatively according to Hasselmann et al. (1976). In the latter case, peak frequency is reproduced by the K-model for any nondimensional fetch, whereas total energy is correct only for limited nondimensional fetch as present in relevant situations of systems with dimensions of a few ten kilometers. K-model results are consistent with observations of directional spread in growing wind seas, observations of swell attenuation, and observations of response to turning winds. Some qualitative deficiencies of the modelling approach, which can be explained by the neglect of nonlinear energy transfer, were pointed out. However, these deficiencies do not apply to small-scale systems characterized by limited nondimensional fetches as specified above. This

means that the modelling approach is suitable for application to coastal wave modelling.

3. In numerical experiments on wind waves in the Sylt-Rømø tidal basin, the applicability of the wave model to small-scale tidal systems was demonstrated. In the experiments, the model served as tool for qualitative investigation and hindcast. Formulation and technical frame of the K-model enable instationary wave modelling of coastal systems with tidal influence. The model can readily be used for numerical investigations of such systems. Results of an April 1997 hindcast of wind waves in the Sylt-Rømø tidal basin were used for a successful model validation against field data at two stations within the basin.

4. The numerical experiments resulted in general conclusions on the nature of the investigated system. These conclusions apply to any coastal system belonging to a class characterized by a similar wave climate and similar tidal features. Wind wave parameters in these systems are distinctly modulated by tides. This is caused by tidal water-level variations and tidal currents in equally significant manner. The wave-hindcast skill is considerably improved by inclusion of current effects into the wave modelling.

General Discussion and Future Work. The general aim of this study was to obtain a wave model for small-scale coastal environments which can be installed into a coupled model system for these environments. The results of the study have shown that a spectral wave model with nonlinear dissipation is readily applicable in coupled modelling of complex systems and leads to a satisfying hindcast skill. Both aspects support the usefulness of the analysed modelling approach for the proposed general aim. This was achieved by a strategy of limiting model complexity, which has enabled coupling of wave dynamics to hydrography of coastal systems in an overall feasible manner. The specific choice of source functions has been used for the first time in a spectral wave model.

In regard to hindcast performance the question arises whether more complex representations of shallow-water wave dynamics as used in alternative modelling approaches, e.g. Ris (1997), would significantly improve the skill of wave hindcasts in coastal environments. Although it is clear that many processes, and in particular internal nonlinear coupling of waves, are present in coastal wave dynamics, it is questionable whether consideration of collected parametrizations for these processes in a wave model will give the desired improvement of skill. This point is supported by the argument that the uncertainty connected to each individual parametrization will add to a general level of noise in the hindcast and thus can diminish skill rather than improving it. To come to a decision in this question it is recommended to perform an intercomparison study of the two modelling approaches. Since the quality of a model is reflected by validation statistics against field data, such a study should consist of a wave hindcast in a coastal system. Statistical significance for the validation must be ensured by choice of a sufficiently long hindcast period in which enough field data are available and in which a significant variety of meteorological situations occurs. A hindcast of this quality was performed within this study for the purpose of validation of the K-model.

The limitations of the approach of spectral wave modelling with nonlinear dissipation have been pointed out in the course of the analysis. Applicability of the K-model to systems charac-

terized by transition to larger scale, spatially and temporarily less variable systems is diminished, because nonlinear transfer of energy gains in relative importance in these and is sufficiently well understood for these applications. Another limitation is the detailed resolution of the spectral fine structure caused by nonlinear transfer of energy. It may be observable but cannot be resolved in the K-model since nonlinear transfer is neglected. An example is bimodal directionality of wave spectra. However, this fine structure will probably be obscured by more dominant advective effects in most coastal applications. For instance, bimodal directionality was not apparent in the small-scale shallow-water results of Young et al. (1996c).

The influence of currents on the source functions has not been considered in the wave modelling approach because of insufficient knowledge on this subject. But influences of this kind became apparent in an observed modulation of measured wave heights with semi-tidal period. One possible reason is enhanced dissipation caused by a current-induced increase of turbulence in the water body. The isotropy of this effect is consistent with the semi-tidal period of the observed modulation. The effect can be parametrized in a straightforward manner within the K-model formulation. A corresponding analysis is thus feasible and also desirable, since a quantitative explanation of the effect would reduce considerable scatter in the hindcast of wave heights. Related work is thus recommended for the future.

It was shown that the spatial and temporal variability of the hindcasted wave fields considerably depends on the structure of water level and current fields. The quality of current modelling thus affects the wave modelling performance. In the presented hindcast results it is remarkable that in spite of a one-to-five reduction of spatial resolution of the wave model compared to the current model, inclusion of currents still led to an improvement of skill. It thus seems worthwhile to make an effort in current modelling to systematically reduce scatter in hindcasted wave parameters rather than regarding current effects as noise in the hindcast of wave parameters. This result is contradictory to the viewpoint in Cardone et al. (1998), where current effects are a priori excluded from the discussions.

According to results of Rudolph (1993), an improvement of a coupled-modelling approach for coastal systems can also be expected by inclusion of mesoscale atmospheric modelling. As was done for tidal influences, the significance of this effect can be assessed by hindcast simulations and analysis of skills of the present and extended model systems. This work is recommended as next step to improve the developed model system.

References

Allender, J. H., J. Albrecht, and G. Hamilton, 1983: Observations of directional relaxation of wind sea spectra, *J. Phys. Oceanogr.*, **13**, 1519–1525.

Banner, M. L., and I. R. Young, 1994: Modeling spectral dissipation in the evolution of wind waves. Part I: Assessment of existing model performance, *J. Phys. Oceanogr.*, **24**, 1550–1571.

Battjes, J. A., and J. P. F. M. Janssen, 1978: Energy loss and set-up due to breaking of random waves, in *Proc. 16th Int. Conf. Coastal Engineering*, 569–587, Hamburg, Germany.

Behrens, A., G. Gayer, H. Günther, and W. Rosenthal, 1997: Atlas der Strömungen und Wasserstände in der Sylt-Rømø-Bucht, GKSS external report 97/E/21, in German.

Bender, L. C., 1996: Modification of the physics and numerics in a third-generation ocean wave model, *J. Atmos. Oceanic Technol.*, **13**, 726–750.

Booij, N., R. C. Ris, and L. H. Holthuijsen, 1998: A third-generation wave model for coastal regions. Part I: Model description and validation (stationary mode), in preparation.

Bouws, E., and G. J. Komen, 1983: On the balance between growth and dissipation in an extreme depth-limited wind sea in the southern North Sea, *J. Phys. Oceanogr.*, **13**, 1653–1658.

Bouws, E., H. Günther, and W. Rosenthal, 1985: Similarity of the wind wave spectrum in finite depth water. 1. Spectral form, *J. Geophys. Res.*, **90**, 975–986.

Bretherton, F. P., and C. J. R. Garrett, 1969: Waves in inhomogeneous moving media, *Proc. Roy. Soc. A.*, **302**, 529–554.

Burgers, G., and V. K. Makin, 1993: Boundary-layer model results for wind-sea growth, *J. Phys. Oceanogr.*, **23**, 372–385.

Cardone, V. J., and D. T. Resio, 1998: An assessment of wave modeling technology, in *Proc. 5th Int. Workshop Wave Hindcasting and Forecasting*, 468–495, Melbourne, Florida.

Casulli, V., and E. Cattani, 1994: Stability, accuracy and efficiency of a semi-implicit method for three-dimensional shallow water flow, *Computers Math. Applic.*, **27**, 99–112.

Casulli, V., and R. T. Cheng, 1992: Semi-implicit finite difference methods for three-dimensional shallow water flow, *Int. J. Num. Methods in Fluids*, **15**, 629–648.

Cavaleri, L., and P. M. Rizzoli, 1981: Wind wave prediction in shallow water – theory and application, *J. Geophys. Res.*, **86**, 10961–10973.

Chalikov, D. V., and M. Y. Belevich, 1993: One-dimensional theory of the wave boundary layer, *Bound.-Layer Meteor.*, **63**, 65–96.

Donelan, M. A., 1995: Air-water exchange processes, in *Proc. IUTAM Symposium on Physical Limnology*, Broome, Australia.

Donelan, M. A., and B. C. Kenney, 1998: Observations of wave dissipation in wind-generated waves, in preparation.

Donelan, M. A., and W. J. Pierson, Jr., 1987: Radar scattering and equilibrium ranges in wind-generated waves with application to scatterometry, *J. Geophys. Res.*, **92**, 4971–5029.

Donelan, M. A., and Y. Yuan, 1994: Wave dissipation by surface processes, in *Dynamics and Modelling of Ocean Waves*, G. J. Komen et al., Eds., Cambridge University Press, 143–155.

Donelan, M. A., J. Hamilton, and W. H. Hui, 1985: Directional spectra of wind-generated waves, *Phil. Trans. R. Soc. Lond.*, **A 315**, 509–562.

Donelan, M. A., M. Skafel, H. Graber, P. Liu, D. Schwab, and S. Venkatesh, 1992: On the growth rate of wind-generated waves, *Atmos.-Ocean*, **30**, 457–478.

Eldeberky, Y., and J. A. Battjes, 1995: Parameterisation of triad interactions in wave energy models, in *Proc. Int. Conf. Coastal Dynamics*, 569–587, Gdansk, Poland.

Eldeberky, Y., and J. A. Battjes, 1996: Spectral modeling of wave breaking: Application to boussinesq equations, *J. Geophys. Res.*, **101**, 1253–1264.

Gelci, R., H. Cazalé, and J. Vassal, 1956: Utilization des diagrammes de propagation a la prevision energetique de la houle, *Bull. Inform. Comité Central Océanogr. Etudes Côtes*, **9**, 170–187, in French.

Goda, Y., 1985: *Random Seas and Design of Maritime Structures*, University of Tokyo Press.

Günther, H., and W. Rosenthal, 1983: A shallow water surface wave model based on the TEXEL-MARSEN-ARSLOE (TMA) wave spectrum, in *Proc. 20th Congress IAHR*, Moscow, Russia.

Günther, H., and W. Rosenthal, 1995: A wave model with a non-linear dissipation source function, in *Proc. 4th Int. Workshop Wave Hindcasting and Forecasting*, Banff, Canada.

Günther, H., W. Rosenthal, T. J. Weare, B. A. Worthington, K. Hasselmann, and J. A. Ewing, 1979: A hybrid parametrical wave prediction model, *J. Geophys. Res.*, **84**, 5727–5738.

Günther, H., W. Rosenthal, and M. Dunckel, 1981: The response of surface gravity waves to changing wind directions, *J. Phys. Oceanogr.*, **11**, 718–728.

Günther, H., S. Hasselmann, and P. A. E. M. Janssen, 1992: *The WAM Model cycle 4.0. User manual.*, Deutsches Klimarechenzentrum Hamburg, technical report no. 4.

Hasselmann, D. E., M. Dunckel, and J. A. Ewing, 1980: Directional wave spectra observed during JONSWAP 1973, *J. Phys. Oceanogr.*, **10**, 1264–1280.

Hasselmann, K., 1962: On the non-linear energy transfer in a gravity wave spectrum, part 1: General theory, *J. Fluid Mech.*, **12**, 481–500.

Hasselmann, K., 1963a: On the non-linear energy transfer in a gravity wave spectrum, part 2: Conservation theorems; wave-particle analogy and irreversibility, *J. Fluid Mech.*, **15**, 273–281.

Hasselmann, K., 1963b: On the non-linear energy transfer in a gravity wave spectrum, part 3: Evaluation of energy flux and swell-sea interation for a Neumann spectrum, *J. Fluid Mech.*, **15**, 385–398.

Hasselmann, K., 1974: On the spectral dissipation of ocean waves due to white capping, *Boundary-Layer Meteorol.*, **6**, 107–127.

Hasselmann, K., and J. I. Collins, 1968: Spectral dissipation of finite-depth gravity waves due to turbulent bottom friction, *J. Mar. Res.*, **26**, 1–12.

Hasselmann, K., D. B. Ross, P. Müller, and W. Sell, 1976: A parametrical wave prediction model, *J. Phys. Oceanogr.*, **6**, 201–228.

Hasselmann, K., T. P. Barnett, E. Bouws, H. Carlson, D. E. Cartwright, K. Enke, J. A. Ewing, H. Gienapp, D. E. Hasselmann, P. Krusemann, A. Meerburg, P. Müller, D. J. Olbers, K. Richter, W. Sell, and H. Walden, 1973: Measurements of wind-wave growth and swell decay during the Joint North Sea Wave Project (JONSWAP), *Dt. Hydrogr. Z. Suppl.*, **A 8 (12)**, 95p.

Hasselmann, S., and K. Hasselmann, 1981: A symmetrical method of computing the non-linear transfer in a gravity-wave spectrum, *Hamb. Geophys. Einzelschr.*, **Serie A, 52**, 138p.

Hasselmann, S., and K. Hasselmann, 1985a: Computations and parametrizations of the non-linear energy transfer in a gravity wave spectrum, part 1: A new method for efficient computations of the exact nonlinear transfer integral, *J. Phys. Oceanogr.*, **15**, 1369–1377.

Hasselmann, S., K. Hasselmann, J. H. Allender, and T. P. Barnett, 1985b: Computations and parametrizations of the nonlinear energy transfer in a gravity wave spectrum, part 2: Parameterizations of the nonlinear energy transfer for application in wave models, *J. Phys. Oceanogr.*, **15**, 1378–1391.

Hasselmann, S., K. Hasselmann, C. Brüning, R. B. Long, H. C. Graber, E. Bauer, and B. Hansen, 1994: Measurements of waves and wind, in *Dynamics and Modelling of Ocean Waves*, G. J. Komen et al., Eds., Cambridge University Press, 60–68.

Herterich, K., and K. Hasselmann, 1980: A similarity relation for the nonlinear energy transfer in a finite-depth gravity-wave spectrum, *J. Fluid Mech.*, **97**, 215–224.

Holthuijsen, L. H., 1983: Observations of the directional distribution of ocean-wave energy in fetch-limited conditions, *J. Phys. Oceanogr.*, **13**, 191–207.

Holthuijsen, L. H., 1994: Observation of the directional response to turning winds, in *Dynamics and Modelling of Ocean Waves*, G. J. Komen et al., Eds., Cambridge University Press, 188–194.

Holthuijsen, L. H., A. J. Kuik, and E. Mosselman, 1987: The response of wave directions to changing wind directions, *J. Phys. Oceanogr.*, **17**, 845–853.

Holthuijsen, L. H., N. Booij, and R. C. Ris, 1993: A spectral model for the tidal zone, in *Proc. Int. Conf. WAVES*.

Janssen, P. A. E. M., 1989: Wave induced stress and the drag of air flow over sea waves, *J. Phys. Oceanogr.*, **19**, 745–754.

Janssen, P. A. E. M., 1991: Quasi-linear theory of wind wave generation applied to wave forecasting, *J. Phys. Oceanogr.*, **21**, 1631–1642.

Janssen, P. A. E. M., G. J. Komen, and W. J. P. de Voogt, 1987: Friction velocity scaling in wind-wave generation, *Bound.-Layer Meteor.*, **38**, 29–35.

Kahma, K. K., 1981: A study of the growth of the wave spectrum with fetch, *J. Phys. Oceanogr.*, **11**, 1503–1515.

Kahma, K. K., and C. J. Calkoen, 1992: Reconciling discrepancies in the observed growth of wind-generated waves, *J. Phys. Oceanogr.*, **22**, 1389–1405.

Kitaigorodskii, S. A., 1962: Application of the theory of similarity to the analysis of wind-generated water waves as a stochastic process, *Bull. Acad. Sci. USSR Geophys.*, **1**, 105–117.

Kitaigorodskii, S. A., 1983a: On the theory of the equilibrium range in the spectrum of wind-generated gravity waves, *J. Phys. Oceanogr.*, **13**, 816–827.

Kitaigorodskii, S. A., and J. L. Lumley, 1983b: Wave-turbulence interaction in the upper ocean. Part 1: The energy balance of the interacting fields of surface wind waves and wind-induced three-dimensional turbulence, *J. Phys. Oceanogr.*, **13**, 1977–1987.

Kitaigorodskii, S. A., and Y. Z. Miropolskii, 1968: Turbulent energy dissipation in the ocean surface layer, *Izv., Atmos. and Ocean. Phys.*, **4**, 647–659.

Kitaigorodskii, S. A., V. P. Krasitskii, and M. M. Zaslavskii, 1975: On Phillips' theory of equilibrium range in the spectra of wind-generated gravity waves, *J. Phys. Oceanogr.*, **5**, 410–420.

Komen, G. J., S. Hasselmann, and K. Hasselmann, 1984: On the existence of a fully developed wind-sea spectrum, *J. Phys. Oceanogr.*, **14**, 1271–1285.

Komen, G. J., L. Cavaleri, M. Donelan, K. Hasselmann, S. Hasselmann, and P. A. E. M. Janssen, 1994: *Dynamics and Modelling of Ocean Waves*, Cambridge University Press.

Lin, R. Q., and N. E. Huang, 1996a: The Goddard Coastal Wave Model. Part I: Numerical method, *J. Phys. Oceanogr.*, **26**, 833–847.

Lin, R. Q., and N. E. Huang, 1996b: The Goddard Coastal Wave Model. Part II: Kinematics, *J. Phys. Oceanogr.*, **26**, 848–862.

Lin, R. Q., and W. Perrie, 1997a: A new coastal wave model. Part III: Nonlinear wave-wave interaction, *J. Phys. Oceanogr.*, **27**, 1813–1826.

Lionello, P., P. Malguzzi, and A. Buzzi, 1998: Coupling between the atmospheric circulation and the ocean wave field: An idealized case, *J. Phys. Oceanogr.*, **28**, 161–177.

Longuet-Higgins, M. S., D. E. Cartwright, and N. D. Smith, 1963: Observation of the directional spectrum of sea waves using the motions of a floating buoy, in *Ocean Wave Spectra*, Prentice Hall, p. 111.

Luo, W., R. Flather, and J. Monbaliu, 1998: An efficient computational scheme for the use of the third generation WAM model in coastal regions, in preparation.

Makin, V. K., 1998: Air-sea exchange of heat in the presence of wind waves and spray, *J. Geophys. R.*, **103**, 1137–1152.

Makin, V. K., V. N. Kudryavtsev, and C. Mastenbroek, 1995: Drag of the sea surface, *Bound.-Layer Meteor.*, **73**, 159–182.

Masson, D., 1990: Observations of the response of sea waves to veering winds, *J. Phys. Oceanogr.*, **20**, 1876–1885.

Miles, J. W., 1957: On the generation of surface waves by shear flows, *J. Geophys. Res.*, **99**, 18501–18511.

Mitsuyasu, H., 1975: Observations of the directional spectrum of ocean waves using a cloverleaf buoy, *J. Phys. Oceanogr.*, **5**, 750–759.

Müller, P., 1976: *Parametrization Of One-dimensional Wind Wave Spectra And Their Dependence On The State Of Development*, vol. 31 of *Hamburger Geophysikalische Einzelschriften*, G. M. L. Wittenborn Söhne, Hamburg, Germany.

NESS Project Consortium, 1992: NESS (North European Storm Study) summary report, Task Report 6010, United Kingdom Meteorological Office.

Phillips, O. M., 1957: On the generation of waves by turbulent wind, *J. Fluid Mech.*, **2**, 417–445.

Phillips, O. M., 1958: The equilibrium range in the spectrum of wind-generated waves, *J. Fluid Mech.*, **4**, 426–434.

Phillips, O. M., 1977: *The Dynamics Of The Upper Ocean*, Cambridge University Press.

Phillips, O. M., 1981: Wave interactions - the evolution of an idea, *J. Fluid Mech.*, **106**, 215–227.

Phillips, O. M., 1985: Spectral and statistical properties of the equilibrium range in wind-generated gravity waves, *J. Fluid Mech.*, **156**, 505–531.

Pierson, W. J., G. Neumann, and R. W. James, 1955: Practical methods for observing and forecasting ocean waves by means of wave spectra and statistics, H.O. Pub 603, US Navy Hydrographic Office.

Pierson, Jr., W. J., and L. Moskowitz, 1964: A proposed spectral form for fully developed wind seas based on the similarity theory of S. A. Kitaigorodskii, *J. Geophys. Res.*, **69**, 5181–5190.

Plant, W. J., 1982: A relationship between wind stress and wave slope, *J. Geophys. Res.*, **87**, 1961–1967.

Plant, W. J., 1986: A two-scale model of short wind-generated waves and scatterometry, *J. Geophys. Res.*, **91**, 10735–10749.

Polnikov, V. G., 1997: Nonlinear energy transfer through the spectrum of gravity waves for the finite depth case, *J. Phys. Oceanogr.*, **27**, 1481–1491.

Resio, D., and W. Perrie, 1991: A numerical study of nonlinear energy fluxes due to wave-wave interactions. part 1: Methodology and basic results, *J. Fluid Mech.*, **223**, 609–629.

Ris, R. C., 1997: Spectral modelling of wind waves in coastal areas, Ph.D. thesis, Delft University of Technology.

Rosenthal, W., 1989: Derivation of Phillips α-parameter from turbulent diffusion as a damping mechanism, in *Radar Scattering from Modulated Wind Waves*, G. J. Komen and W. A. Oost, Eds., Kluwer Academic Publishers, 81–88.

Rudolph, E., 1993: Impulsaustausch zwischen Atmosphäre und Ozean im Küstenbereich, Ph.D. thesis, GKSS external report 93/E/57, in German.

Schneggenburger, C., H. Günther, and W. Rosenthal, 1997: Shallow water wave modelling with nonlinear dissipation, *Dt. Hydrogr. Z.*, **49**, 431–444.

Schneggenburger, C., H. Günther, and W. Rosenthal, 1997b: Shallow water wave modeling with nonlinear dissipation: application to small scale systems, oral presentation at WISE San Francisco.

Schneggenburger, C., H. Günther, and W. Rosenthal, 1998: Shallow water wave modeling with nonlinear dissipation: Application to small scale tidal systems, in *Proc. 5th Int. Workshop Wave Hindcasting and Forecasting*, 242–255, Melbourne, Florida.

Shore Protection Manual, 1984: *Shore Protection Manual*, Department of the Army, Waterways Experiment Station, Vicksburg, Mississippi, 4th ed.

Snodgrass, F. E., G. W. Groves, K. F. Hasselmann, G. R. Miller, W. H. Munk, and W. H. Powers, 1966: Propagation of ocean swell across the Pacific, *Philos. Trans. Roy. Soc. London*, **A249**, 431–497.

Snyder, R. L., F. W. Dobson, J. A. Elliott, and R. B. Long, 1981: Array measurements of atmospheric pressure fluctuations above surface gravity waves, *J. Fluid Mech.*, **102**, 1–59.

Snyder, R. L., L. M. Lawson, and R. B. Long, 1992: Inverse modeling of the action-balance equation. Part I: Source expansion and adjoint model equations, *J. Phys. Oceanogr.*, **22**, 1540–1555.

Stewart, R. H., and J. W. Joy, 1974: HF radio measurements of surface currents, *Deep-Sea Res.*, **21**, 1039–1049.

SWAMP group: J. H. Allender, T. P. Barnett, L. Bertotti, J. Bruinsma, V. J. Cardone, L. Cavaleri, J. Ephraums, B. Golding, A. Greenwood, J. Guddal, H. Günther, K. Hasselmann, S. Hasselmann, P. Joseph, S. Kawai, G. J. Komen, L. Lawson, H. Linné, R. B. Long, M. Lybanon, E. Maeland, W. Rosenthal, Y. Toba, T. Uji, and W. J. P. de Voogt, 1985: *Ocean Wave Modeling*, Plenum Press.

SWIM group: E. Bouws, J. J. Ephraums, J. A. Ewing, P. E. Francis, H. Günther, P. A. E. M. Janssen, G. J. Komen, W. Rosenthal, and W. J. P. de Voogt, 1985: A shallow water intercomparison of three numerical wave prediction models (SWIM), *Quart. J. R. Met. Soc.*, **111**, 1087–1112.

Thornton, E. B., 1977: Rederivation of the saturation range in the frequency spectrum of wind-generated gravity waves, *J. Phys. Oceanogr.*, **7**, 137–140.

Toba, Y., 1973: Local balance in the air-sea boundary process, 3. On the spectrum of wind waves, *Oceanogr. Soc.*, **29**, 209–220.

Tolman, H. L., 1990: The influence of unsteady depths and currents of tides on wind-wave propagation in shelf seas, *J. Phys. Oceanogr.*, **20**, 1166–1174.

Tolman, H. L., 1991a: Effects of tides and storm surges on North Sea wind waves, *J. Phys. Oceanogr.*, **21**, 766–781.

Tolman, H. L., 1991b: A third-Generation model for wind waves on slowly varying, unsteady, and inhomogeneous depths and currents, *J. Phys. Oceanogr.*, **21**, 782–797.

Tolman, H. L., 1992: Effects of numerics on the physics in a third-generation wind-wave model, *J. Phys. Oceanogr.*, **22**, 1095–1111.

Tolman, H. L., and D. V. Chalikov, 1996: Source terms in a third-generation wind wave model, *J. Phys. Oceanogr.*, **26**, 2497–2518.

van Vledder, G. P., and L. H. Holthuijsen, 1993: The directional response of ocean waves to turning winds, *J. Phys. Oceanogr.*, **23**, 177–192.

WAMDI group: S. Hasselmann, K. Hasselmann, E. Bauer, P. A. E. M. Janssen, G. J. Komen, L. Bertotti, P. Lionello, A. Guillaume, V. C. Cardone, J. A. Greenwood, M. Reistad, L. Zambresky, and J. A. Ewing, 1988: The WAM model – a third generation ocean wave prediction model, *J. Phys. Oceanogr.*, **18**, 1775–1810.

Weber, S. L., 1988: The energy balance of finite depth gravity waves, *J. Geophys. Res.*, **93 (C4)**, 3601–3607.

Weber, S. L., 1991: Eddy-viscosity and drag-law models for random ocean wave dissipation, *J. Fluid Mech.*, **232**, 73–98.

Weber, S. L., 1994: Bottom friction and percolation, in *Dynamics and Modelling of Ocean Waves*, G. J. Komen et al., Eds., Cambridge University Press, 156–166.

Willebrand, J., 1975: Energy transport in a nonlinear and inhomogeneous random gravity wave field, *J. Fluid Mech.*, **70**, 113–126.

Wolf, T., and W. Rosenthal, 1998: Mesoscale wind and wave field modelling in the area of the Odra lagoon, in preparation.

Wu, J., 1982: Wind-stress coefficients over sea surface from breeze to hurricane, *J. Geophys. Res.*, **87**, 9704–9706.

Young, I. R., 1994: On the measurement of directional wave spectra, *Appl. Ocean Res.*, **16**, 283–294.

Young, I. R., 1998: Observations of the spectra of hurricane generated waves, *Ocean Engng*, **25**, 261–276.

Young, I. R., and L. A. Verhagen, 1996a: The growth of fetch limited waves in water of finite depth. Part 1. Total energy and peak frequency, *Coastal Engineering*, **29**, 47–78.

Young, I. R., and L. A. Verhagen, 1996b: The growth of fetch limited waves in water of finite depth. Part 2. Spectral evolution, *Coastal Engineering*, **29**, 79–99.

Young, I. R., and G. P. V. Vledder, 1993: A review of the central role of nonlinear interactions in wind-wave evolution, *Phil. Trans. R. Soc. Lond.*, **A 342**, 505–524.

Young, I. R., W. Rosenthal, and F. Ziemer, 1985a: A three-dimensional analysis of marine radar images for the determination of ocean wave directionality and surface currents, *J. Geophys. Res.*, **90**, 1049–1059.

Young, I. R., S. Hasselmann, and K. Hasselmann, 1987: Computations of the response of a wave spectrum to a sudden change in wind direction, *J. Phys. Oceanogr.*, **17**, 1317–1338.

Young, I. R., L. A. Verhagen, and S. K. Khatri, 1996c: The growth of fetch limited waves in water of finite depth. Part 3. Directional spectra, *Coastal Engineering*, **29**, 101–121.

A Technical Details

A.1 Wave Spectra

In this section, important explicit representations of the wave spectrum resulting from transformation to alternative independent variables are introduced. In some cases, original and transformed spectra are denoted by the same symbol. But since the spectra are usually quoted with arguments, this does not lead to confusion. In the second part of the section, parametric spectral forms for one-dimensional energy spectrum and directional distribution will be given.

Wave-number-direction Spectrum. For $k > 0$ the wave vector can be represented in polar coordinates yielding the wave-number-direction spectrum

$$F(k, \theta) = k\, F(\boldsymbol{k})\,. \tag{A.1}$$

Here and subsequently, the quantity θ gives the direction of the wave vector measured clockwise from north. The wave-number-direction spectrum is more suitable in a discrete representation of the spectrum for the purpose of numerical treatment, since in this case the directional resolution does not change with wave number k, i.e. wave energy in different wave length bins is treated with the same directional resolution.

The spectrum of wave vector moduli $F(k)$ is not obtained from directional integration of (A.1). It is defined by integration of $F(\boldsymbol{k})$ over wavevectors $\boldsymbol{k}$ with $\|\boldsymbol{k}\| = k$ (Kitaigorodskii 1983a).

Frequency-direction Spectrum. A common representation of the wave spectrum is the frequency-direction spectrum

$$E(f, \theta) = \frac{2\pi k}{v_{\mathrm{g}}} F(\boldsymbol{k})\,. \tag{A.2}$$

Many spectral wave models use this representation of the wave spectrum as prognostic field, because in this representation the dynamics will simplify in the case of stationary external fields. Note that the group velocity can be zero in the case of strong opposing currents (wave blocking). Therefore, care is needed in the use of this transformation.

One-dimensional Frequency Spectrum. The one-dimensional frequency spectrum $E(f)$ is obtained by integration of $E(f, \theta)$ over the directions:

$$E(f) \equiv \int_0^{2\pi} \mathrm{d}\theta E(f, \theta). \tag{A.3}$$

The directional distribution $D(f, \theta)$ is connected to it via the definition

$$D(f, \theta) \equiv E(f, \theta)/E(f). \tag{A.4}$$

One-dimensional spectrum and directional distribution allow direct comparison with measurements from buoy and directional-buoy measurements (Hasselmann et al. 1994).

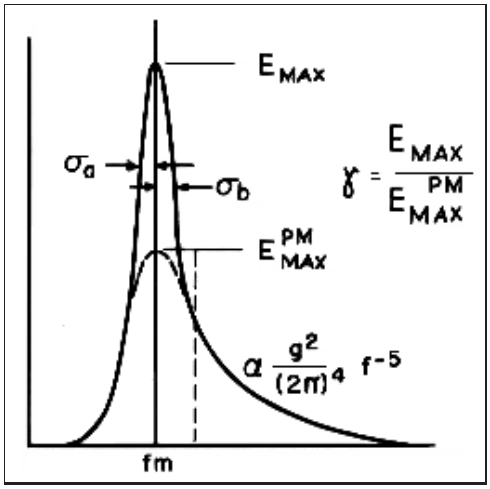

Figure A.1: JONSWAP spectrum. The figure is taken from Hasselmann et al. (1973), figure 2.5 on p. 33. Spectral energy density $E(f)$ is displayed as function of frequency f. The JONSWAP parameters f_m, α, γ, σ_a, and σ_b are illustrated.

Typical measured one-dimensional frequency spectra are characterized by a peak at a thus defined peak frequency f_m, a forward face with a sharp decline of energy for frequencies smaller than the peak frequency, and a more gently sloped rear face at frequencies greater than the peak frequency (Donelan et al. 1985). A subrange of the rear face characterized by frequencies considerably larger than the peak frequency is called equilibrium range of the spectrum.

JONSWAP Spectrum. The parametric spectral form which resulted from the JONSWAP experiment is given in this paragraph. It depends on the JONSWAP parameters peak frequency f_m, Phillips constant α, overshoot parameter γ, and peak width parameter σ. Two values are commonly specified for the latter: the width of the forward face σ_a and the width of the rear face σ_b. The JONSWAP spectrum reads

$$E(f) = \alpha g^2 (2\pi)^{-4} f^{-5} \exp\left(-\tfrac{5}{4}\left(\tfrac{f}{f_\mathrm{m}}\right)^{-4}\right) \gamma^{\exp \frac{-(f-f_\mathrm{m})^2}{2\sigma^2 f_\mathrm{m}^2}}, \tag{A.5}$$

$$\sigma = \begin{cases} \sigma_\mathrm{a} & \text{for } f \leq f_\mathrm{m} \\ \sigma_\mathrm{b} & \text{for } f > f_\mathrm{m} \end{cases}.$$

The spectrum is a generalization of the Pierson-Moskowitz spectral form, which is characterized by two parameters f_m and α (Pierson et al. 1964). It is generalized by a peak-enhancement factor containing the given power of γ. Parameter γ describes the ratio of spectral peak energy to Pierson-Moskowitz peak energy. The JONSWAP spectrum is illustrated in figure A.1. The figure also displays the corresponding Pierson-Moskowitz spectrum.

Directional Spread Parameter. A common parametrization of the directional distribution was given by Mitsuyasu et al. (1975). It reads

$$D(f,\theta) = J \cos^{2s(f)}\left(\frac{\theta - \langle\theta\rangle}{2}\right), \tag{A.6}$$

with $\langle\theta\rangle$ denoting the mean wave direction and J a normalization constant. The directional-spread parameter $s(f)$ is frequency dependent. The spread parameter is commonly used to describe directional spread of measured and model spectra. For a given directional distribution, it can be obtained from the Fourier coefficients

$$\begin{aligned} a_1 &\equiv \int \mathrm{d}\theta D(f,\theta)\cos(\theta) \\ b_1 &\equiv \int \mathrm{d}\theta D(f,\theta)\sin(\theta) \qquad \text{(A.7)} \\ r_1 &\equiv \sqrt{a_1^2+b_1^2} \qquad \text{(A.8)} \end{aligned}$$

of the directional distribution according to the formula

$$s = \frac{r_1}{1-r_1} \qquad \text{(A.9)}$$

(Hasselmann et al. 1980). The directional-spread parameter can be determined alternatively from a least-square fit of the directional distribution to the parametrization (A.6).

A.2 Derivation of Specific Nonlinear Dissipation Terms

The statements of subsection 2.2.1 on the consistency of specific nonlinear dissipation terms with a general power-series-expansion formulation (2.34) will be treated in this section.

Outline of Proof for Second-order Nonlinear Dissipation. To show the consistency, specific features of the expansion coefficients in (2.34) are assumed. The first few integrals of the expansion are discussed separately. The results are then interpreted to yield an evaluation of the complete expansion integral which equals the proposed second-order nonlinear term.

1. Regard the first integral in (2.34). Assume the specific form

$$\zeta(\boldsymbol{k},\boldsymbol{k}_1) = f(\boldsymbol{k})\delta(\boldsymbol{k}_1-\boldsymbol{k}) \qquad \text{(A.10)}$$

for the expansion coefficient. The integral can then be evaluated as

$$\int \mathrm{d}\boldsymbol{k}_1\zeta(\boldsymbol{k},\boldsymbol{k}_1)N(\boldsymbol{k}_1) = \int \mathrm{d}\boldsymbol{k}_1 f(\boldsymbol{k})\delta(\boldsymbol{k}_1-\boldsymbol{k})N(\boldsymbol{k}_1) = f(\boldsymbol{k})N(\boldsymbol{k})\,. \qquad \text{(A.11)}$$

2. Regard the second integral in (2.34). Let the expansion coefficient take the specific form

$$\eta(\boldsymbol{k},\boldsymbol{k}_1,\boldsymbol{k}_2) = f(\boldsymbol{k})\eta_1(\boldsymbol{k}_1)\delta(\boldsymbol{k}_2-\boldsymbol{k})\,, \qquad \text{(A.12)}$$

where $\eta_1(\boldsymbol{k}_1)$ is isotropic and Taylor-expandible to arbitrary order. Consider this coefficient in its (isotropic) expansion expression

$$\eta_1(\boldsymbol{k}_1) = \eta_1(k_1) = \sum_i \alpha_i k_1^i\,. \qquad \text{(A.13)}$$

Upon insertion of these expressions, the integral is evaluated as

$$\begin{aligned}&\int\int \mathrm{d}\boldsymbol{k}_1\mathrm{d}\boldsymbol{k}_2\eta(\boldsymbol{k},\boldsymbol{k}_1,\boldsymbol{k}_2)N(\boldsymbol{k}_1)N(\boldsymbol{k}_2) = \\ &\int\int \mathrm{d}\boldsymbol{k}_1\mathrm{d}\boldsymbol{k}_2 f(\boldsymbol{k})\sum_i \alpha_i k_1^i\,\delta(\boldsymbol{k}_2-\boldsymbol{k})N(\boldsymbol{k}_1)N(\boldsymbol{k}_2) = \\ &f(\boldsymbol{k})N(\boldsymbol{k})\sum_i \alpha_i\int \mathrm{d}\boldsymbol{k}_1 k_1^i N(\boldsymbol{k}_1) = f(\boldsymbol{k})N(\boldsymbol{k})L(m_0,m_1,\ldots)\,,\end{aligned} \tag{A.14}$$

where $L(\ldots)$ is a linear function of arbitrary scalar moments of N.

3. Regard the third integral in (2.34). The expansion coefficient is, similar to 2., considered as

$$\xi(\boldsymbol{k},\boldsymbol{k}_1,\boldsymbol{k}_2,\boldsymbol{k}_3) = f(\boldsymbol{k})\sum_i \alpha_i k_1^i \sum_j \beta_j k_2^j\,\delta(\boldsymbol{k}_3-\boldsymbol{k})\,. \tag{A.15}$$

The integral is accordingly

$$\begin{aligned}&\int\int\int \mathrm{d}\boldsymbol{k}_1\mathrm{d}\boldsymbol{k}_2\mathrm{d}\boldsymbol{k}_3\xi(\boldsymbol{k},\boldsymbol{k}_1,\boldsymbol{k}_2,\boldsymbol{k}_3)N(\boldsymbol{k}_1)N(\boldsymbol{k}_2)N(\boldsymbol{k}_3) = \\ &f(\boldsymbol{k})N(\boldsymbol{k})L_1(m_0,m_1,\ldots)L_2(m_0,m_1,\ldots) = f(\boldsymbol{k})N(\boldsymbol{k})Q(m_0,m_1,\ldots)\,,\end{aligned} \tag{A.16}$$

where $L_{1,2}(\ldots)$ are linear functions and $Q(\ldots)$ is a quadratic function of the moments.

4. Regard the nth integral. Upon similar assumptions for the expansion coefficient, it can be evaluated as

$$\int\int\ldots\int \mathrm{d}\boldsymbol{k}_1\mathrm{d}\boldsymbol{k}_2\ldots\mathrm{d}\boldsymbol{k}_n\chi(\boldsymbol{k},\boldsymbol{k}_1,\ldots,\boldsymbol{k}_n)N(\boldsymbol{k}_1)N(\boldsymbol{k}_2)\ldots N(\boldsymbol{k}_n) = f(\boldsymbol{k})N(\boldsymbol{k})P_{n-1}(m_0,m_1,\ldots)\,, \tag{A.17}$$

where $P_{n-1}(\ldots)$ is a polynomial of order $n-1$ of the moments.

5. Insertion of the obtained results gives an expression of the integral expansion (2.34) up to order n:

$$S_{\mathrm{dis}} = f(\boldsymbol{k})N^2(\boldsymbol{k})\left\{L(m_0,m_1,\ldots)+Q(m_0,m_1,\ldots)+\ldots+P_{n-1}(m_0,m_1,\ldots)\right\}+O(n+1)\,. \tag{A.18}$$

Now, all appearing polynomial expressions are grouped to one polynomial $\tilde{P}_{n-1}$. It is assumed to be the Taylor polynomial expression for a function g. If the limit $n\to\infty$ is taken, the dissipation term becomes

$$S_{\mathrm{dis}} = f(\boldsymbol{k})g(m_0,m_1,\ldots)N^2(\boldsymbol{k})\,, \tag{A.19}$$

which is the desired result. Concluding, it has been shown that specific expressions for the expansion coefficients in (2.34) exist, which allow the general dissipation function (2.34) to be simplified to an expression (2.35).

Other expressions. Other expressions as given in subsection 2.2.1 can be obtained similarly. The WAM dissipation function is obtained by replacing the delta functions in the above derivation by regular isotropic and expandible functions. Dissipation functions with higher-order powers in the wave spectrum can be obtained by introducing further delta functions.

A.3 Refraction Velocities

It was mentioned in 2.3.3 that the refraction velocities, also termed "dot terms", can be written in the K-model as sums

$$\dot{k} = \dot{k}_{\mathrm{D}} + \dot{k}_{\mathrm{C}}, \quad \dot{\theta} = \dot{\theta}_{\mathrm{D}} + \dot{\theta}_{\mathrm{C}}, \tag{A.20}$$

where the subscripts D and C denote depth and current refraction. The individual terms are:

$$\begin{aligned}
\dot{k}_{\mathrm{D}} &= \frac{\sigma k}{\sinh 2kh}\left(-\sin\theta\,\partial_{x_1}h - \cos\theta\,\partial_{x_2}h\right), \\
\dot{k}_{\mathrm{C}} &= -k\sin\theta\left(\sin\theta\,\partial_{x_1}u + \cos\theta\,\partial_{x_1}v\right) - k\cos\theta\left(\sin\theta\,\partial_{x_2}u + \cos\theta\,\partial_{x_2}v\right), \\
\dot{\theta}_{\mathrm{D}} &= \frac{\sigma}{\sinh 2kh}\left(-\cos\theta\partial_{x_1}h + \sin\theta\,\partial_{x_2}h\right), \\
\dot{\theta}_{\mathrm{C}} &= -\cos\theta\left(\sin\theta\,\partial_{x_1}u + \cos\theta\,\partial_{x_1}v\right) + \sin\theta\left(\sin\theta\,\partial_{x_2}u + \cos\theta\,\partial_{x_2}v\right).
\end{aligned} \tag{A.21}$$

The components of the current field $\boldsymbol{u}_{\mathrm{c}}$ are given here as u and v.

A.4 Validation Statistics Parameters

In this section, statistical parameters which have been used for validation of model results against field data will be defined. Consider time series of field data and model results at a given station. Let x_i be numbered measurement data and y_i corresponding model results, both data sets consisting of n elements.

The mean of measurements is given by

$$\overline{x} = \frac{1}{n}\sum_{i=1}^{n} x_i\,, \tag{A.22}$$

the mean of model results $\overline{y}$ is defined analogously.

The standard deviation of measured data reads

$$\sigma_x = \sqrt{\frac{1}{n-1}\sum_{i=1}^{n}(\overline{x} - x_i)^2}\,, \tag{A.23}$$

the standard deviation of model results σ_y being defined analogously.

The bias is given by

$$\mathrm{b} = \overline{x} - \overline{y}\,. \tag{A.24}$$

Root-mean-square error (rms error) is defined as

$$\mathrm{rms} = \sqrt{\frac{1}{n}\sum_{i=1}^{n}(x_i - y_i)^2}\,. \tag{A.25}$$

The standard deviation of model data to measured data is given by

$$\sigma = \sqrt{\frac{1}{n-1}\sum_{i=1}^{n}((x_i - \overline{x}) - (y_i - \overline{y}))^2}\,. \tag{A.26}$$

A definition of scatter index as used in this thesis is

$$\mathrm{si} = \frac{\sigma}{\overline{x}}\,. \tag{A.27}$$

An alternative, less common definition involves the rms error instead of standard deviation.

The reduction of variance reads

$$\mathrm{rv} = 1 - \frac{\sum_{i=1}^{n}(y_i - x_i)^2}{\sum_{i=1}^{n}(y_i - \overline{x})^2}\,. \tag{A.28}$$

It is a measure of forecasting or hindcasting skill. A value of one indicates perfect skill. A value below zero indicates that use of the measured mean as prediction instead of model results leads to a better forecasting or hindcasting performance. In meteorological applications, the mean of measurements appearing in the denominator of (A.28) is usually replaced by a climatological mean. Since a climatological mean cannot be given for wave hindcasts as presented in this thesis, the alternative definition using the mean of measurements has been used.

B List of Symbols and Acronyms

A list of used symbols and acronyms is given in this appendix.

Roman Letters.

a	wave amplitude
c	wave phase velocity
c.c.	complex conjugate
$D(f,\theta)$	directional distribution
$E(f)$	one-dimensional frequency spectrum
$\tilde{E}(f)$	dimensionless one-dimensional spectrum
$E(f,\theta)$	frequency direction spectrum
$\overline{E}$	spatially mean energy density
f	frequency
$\tilde{f}$	dimensionless frequency
f_{m}	peak frequency of one-dimensional spectrum
f_{PM}	Pierson Moskovitz frequency
$f(\boldsymbol{k})$	function of wave vector
$F(\boldsymbol{k})$, $F(\boldsymbol{k},\boldsymbol{x},t)$	wave (energy density) spectrum
$\hat{F}(\boldsymbol{\xi},\tau)$	two-point covariance function
$\tilde{F}(\boldsymbol{\kappa})$	wave spectrum with respect to generalized coordinates
g	gravitational acceleration
$g(m_0,m_1,\ldots)$	function of spectral moments
G	gustiness parameter
h	water depth
H_{S}	significant wave height
i	imaginary unit
k	wave number
$\boldsymbol{k}$	two-dimensional (horizontal) wave vector
m_0, m_1, ...	spectral moments
$N(\boldsymbol{k})$, $N(\boldsymbol{k},\boldsymbol{x},t)$	wave action density spectrum
p_1, p_2	coupling parameters of nonlinear dissipation
P	joint probability density of surface elevations
q	coupling parameter of nonlinear dissipation
$s(f)$	Mitsuyasu directional spread parameter
$S(N)$	total source function
S_{bot}	bottom interaction dissipation source function
S_{dis}	dissipation source function
S_{in}	wind-input source function
S_{nl}	quadruplet nonlinear interaction source function
S_{phil}	Phillips wind input source function
t	time
T	wave period

T_{m1}, T_{m2}	integrated wave periods
u_*	friction velocity
u_{10}	wind velocity in ten meters height
$\boldsymbol{u}_{\mathrm{c}}$	near-surface two-dimensional current field
v_{g}	modulus of wave group velocity
$\boldsymbol{v}_{\mathrm{g}}$	wave group velocity
$\boldsymbol{x}$	two-dimensional (horizontal) location vector
z	vertical location coordinate

Greek Letters.

α	Phillips parameter, linear-growth wind input parameter
β	exponential-growth wind input parameter
β_0	scaling constant of exponential-growth wind input
γ	dissipation parameter, JONSWAP overshoot parameter
γ_0	scaling parameter of nonlinear dissipation
Γ	scaling constant of bottom dissipation interaction
δ	dimensionless water depth
$\Delta \ldots$	finite difference
ϵ, ϵ_*	dimensionless total energies
$\zeta(\boldsymbol{k}, \boldsymbol{k}_1)$	expansion coefficient
$\zeta(\boldsymbol{x}, t)$	function of local properties of the medium
η	surface elevation field
$\eta(\boldsymbol{k}, \boldsymbol{k}_1, \boldsymbol{k}_2)$	expansion coefficient
θ	wave vector direction, relative angle of wind and wave vector
θ_{w}	wind vector direction
$\theta(\boldsymbol{x}, t)$	phase function
$\boldsymbol{\kappa}$	generalized wave vector coordinates
λ	wave length
ν, ν_*	dimensionless peak frequencies
$\boldsymbol{\xi}$	difference of space locations
ρ_{a}	density of air
ρ_{w}	density of water
σ	standard deviation
σ, $\sigma_\pm$	intrinsic circular frequencies
σ_{a}, σ_{b}	JONSWAP peak-width parameters
τ	difference of times, dimensionless time
τ_*	dimensionless turning-wind relaxation time
Φ	probability function
Φ_{K}	Kitaigorodskii factor
χ, χ_*	dimensionless fetches
ω, $\omega_\pm$	absolute circular frequencies
Ω	dispersion function

Further Symbols.

∂_t	partial time derivative
$\partial_{\boldsymbol{k}}$	$\boldsymbol{k}$ space gradient
$\partial_{\boldsymbol{x}}$	physical space gradient
$\langle \ldots \rangle$	ensemble expectation value

Acronyms.

BMO	British Meteorological Office wave model
DWD	Deutscher Wetterdienst (German Meteorological Office)
E20	wind at ten meters height of east 20 m/s
GKSS	GKSS-Forschungszentrum Geesthacht GmbH
HRMS	Hasselmann et al. (1976)
HYPA	HYbrid PArametrical wave model (Günther et al. 1979)
HYPAS	shallow-water version of HYPA (Günther et al. 1984)
JONSWAP	JOint North Sea WAve Project
NW20	wind at ten meters height of northwest 20 m/s
PROMISE	European Union MAST III Programme MAS3 CT 9500025 "PRe Operational Modelling in the Seas of Europe"
rms (error)	root-mean-square (error)
SWAN	Simulation of WAves in the Near-shore (Holthuijsen et al. 1996)
VENICE	model for wind wave prediction (Cavaleri et al. 1981)
WAM	third-generation WAve Model (WAMDI 1988)

Acknowledgements

The research for this thesis was carried out at the Institut für Gewässerphysik of GKSS-Forschungszentrum Geesthacht GmbH. I would like to thank Prof. Dr. Hans von Storch and Dr. Wolfgang Rosenthal from GKSS-Forschungszentrum for enabling this work, review of the thesis, and for guiding discussions.

I am especially indebted to Dr. Wolfgang Rosenthal and to Dr. Heinz Günther for their stimulating ideas, for many clarifying discussions and constant support. In addition, I would like to thank all members of the department GMS at GKSS for support in many aspects, especially Dr. Arno Behrens and Gerhard Gayer for carrying out the current modelling in the Sylt-Rømø tidal basin, Dr. Behrens for supplying DWD wind fields, and Gerhard Gayer for support in preparing figures.

I wish to thank Dagmar Herbers and Peter Rybaczok of the GKSS Institut für Gewässerphysik for giving access to the field data from the Sylt-Rømø tidal basin.

The supply of tide-gauge data at Westerland, Sylt, by the Amt für Land- und Wasserwirtschaft Husum is gratefully acknowledged.

The computations of the North-Sea hindcast and the Sylt-Rømø-tidal-basin applications have been performed on a CRAY C90 at the Deutsche Klimarechenzentrum, Hamburg. Technical support is gratefully acknowledged.

Finally, I would like to thank Mrs. Renate Schneggenburger for editorial advice and proof reading of the English manuscript.